Chapter II.8

Vacuum systems

Vincent Baglin, Roberto Kersevan
CERN, Geneva, Switzerland

Vacuum for accelerators is a transverse field across several engineering and scientific disciplines. This lecture introduces the fundamentals of vacuum science and technology and presents the main aspects with a special focus on particle accelerators.

II.8.1 Introduction

Vacuum cannot be "perfect" by essence, neither on earth nor in space! For instance, in the interstellar medium of a galaxy such as the Milky Way, the space is composed of molecules, ionized atoms, cosmic rays and dust (size 0.1 µm). In cold molecular clouds ($>$ 10 K) the gas density reaches 10^4 molecules/cm^3. Atomic densities are about 50 H/cm^3 at 100 K ($\sim 10^{-13}$ Pa) or 1 H/cm^3 at $10\,000$ K ($\sim 10^{-13}$ Pa). On earth, the vacuum science and technology is used in many areas of the domestic life and industry. The light bulb operating under 0.7 atm of Ar or cathodic tubes are well known examples. In semiconductor industry or for electron beam welding machines and vacuum brazing, vacuum is also of great importance as well as for the accelerator technology. Hence, the objective of vacuum science and technology is to reduce the collision rate of molecules with the surrounding environment to preserve the quality of a process.

Vacuum in an accelerator is required to reduce the collision of the beam with the residual gas. This basic requirement helps to preserve the beam emittance, to reach long beam lifetime (fundamental in high luminosity colliders), to lower the probability of generating secondary particles (e.g., electrons, ions, photons, etc.), to reduce radioactive activation of tunnel and accelerator components (improving maintainability while reducing the dose to the personnel during maintenance periods) and finally helps to preserve the properties of specially prepared surface (e.g., a photocathode).

Vacuum science and technology has a long standing history that may be illustrated with the level of vacuum obtained during the years [1]. These achievements were dictated by the developments of vacuum pumps and vacuum gauges, from 10^{-4} Pa in the 1900's until 10^{-12} Pa measured by the end of the XXth century. Today, the lowest measured pressure can be derived from the Baryon-Antibaryon Symmetry Experiment (BASE) at CERN. By measuring the annihilation of anti-protons due to beam-gas scattering, the estimated pressure in the cryogenic Penning trap equals 10^{-17} Pa, i.e. $2\,400$ molecules/m^3 at 4.5 K (see Eq. II.8.6) [2].

This chapter should be cited as: Vacuum systems, V. Baglin and R. Kersevan, DOI: 10.23730/CYRSP-2024-003.1259, in: Proceedings of the Joint Universities Accelerator School (JUAS): Courses and exercises, E. Métral (ed.), CERN Yellow Reports: School Proceedings, CERN-2024-003, DOI: 10.23730/CYRSP-2024-003, p. 1259.

For comparison, in the Large Hadron Collider (LHC), the measure of the beam-gas scattering using the beam loss monitors yields a modest 2.5×10^{12} molecules/m^3 at 15 K. However, the corresponding beam-gas lifetime (see Section II.8.7) equals 4.5 years i.e., 400 times longer than the LHC design value!

II.8.2 Basic concepts

There is a plethora of books and a few CERN Yellow Reports that discuss in detail the fundamentals of vacuum science and technology, see e.g. Refs. [3–12]. Hence, in this section, we will concentrate on the most important concepts.

II.8.2.1 Gas kinetic theory

Large numbers of molecules in a vessel move always in a disordered manner but with a rectilinear and uniform movement between successive elastic collisions. As demonstrated by Maxwell and Boltzmann, a pure gas in thermal equilibrium enclosed in an isothermal volume has the following properties:

1. the molecular density is constant in the volume and do not vary with time,
2. the direction of the molecules' speed is isotropic,
3. the speed distribution is stationary.

As a result, the speed of the molecules follows a Maxwell-Boltzmann distribution. The most probable speed, v_p, is obtained at the maximum of the distribution. It can be noted that less than $1/1\,000$ of the molecules have a speed lower than $0.1\ v_p$ or larger than $3\ v_p$. It shall be underlined that the most probable speed is different from the average thermal speed and the average quadratic speed derived from the Maxwell-Boltzmann distribution. It is noted that all molecular speeds scale like $\sqrt{\frac{T}{m}}$.

This is the average thermal speed, v, that is useful in vacuum science and technology. It is given by Eq. II.8.1 (the larger the temperature, the larger the thermal velocity of the molecule; the larger the molecule mass, the lower the thermal velocity)

$$v = \sqrt{\frac{8\,kT}{\pi\,m}} \quad , \tag{II.8.1}$$

with $k = 1.38 \times 10^{-23}$ J/K the Boltzmann constant (or 86.17 meV/K), *T* the gas temperature in K and *m* the mass of the molecule in kg. The average thermal speed ranges from 50–100 m/s to several 1 000 m/s. Therefore, the travelled distance of a molecule in a second is much larger than the vacuum chamber dimensions. The engineering formula is given by Eq. II.8.2 where *M* is the molar mass in g,

$$v\ [\text{m/s}] \ = \ 145.5 \sqrt{\frac{T[\text{K}]}{M[\text{g}]}} \quad . \tag{II.8.2}$$

Exercise 1: what are the average velocities of helium, air and argon at room temperature? Conclusion?

The molecular collision rate on the wall, ν, can be also derived from the Maxwell-Boltzmann distribution. This is the number of molecules that impinges on a wall per unit of time and unit of surface. It is directly proportional to the average thermal speed and the gas density as given by Eq. II.8.3,

$$\nu = \frac{1}{4} n v \quad , \tag{II.8.3}$$

with n the molecular gas density in molecules/m^3 and v the average molecular speed in m/s.

This parameter is useful to understand the importance of the level of vacuum in a vessel. Indeed, the properties of a vacuum chamber surface can be strongly modified by the adsorption of molecules onto it. The quantity of molecules in a single layer of gas (or monolayer, θ_m) is approximately given by $\sim 10^{15}$ molecules/cm^2, it is simply derived from the approximate surface area of a molecule (~ 10 Å^2). Equation II.8.4 below allows to compute the monolayer formation time t_m,

$$t_m = \frac{\theta_m}{v} \quad . \tag{II.8.4}$$

Exercise 2: what is the monolayer formation time of hydrogen at room temperature at 1 atm, 10^{-6} mbar and 10^{-11} mbar? Conclusion?

A unit to remember is the Langmuir, L, that corresponds to an exposure of 10^{-6} Torr during 1 second, 1 L = 10^{-6} Torr·s. Since 1 Torr equals 1.33 mbar, 1 Langmuir exposure corresponds to about 1 monolayer. In practical terms, 1 L $\sim$ 1 monolayer/s.

The pressure is defined by the force exerted on the vacuum wall by the molecules per unit of surface. The Pascal, Pa, is the Standard International (SI) unit, 1 Pa = 1 N/m^2. However, in vacuum science and technology other units are routinely used such as mbar in Europe and Torr in US (1 Torr = 1 mm of Hg in Torricelli's tube). Table II.8.1 gives some units and their conversions to others.

From the pressure definition, when a vacuum vessel is evacuated a force is exerted onto it by the atmospheric pressure. This force amounts to 1 kg/cm^2. This is not negligible and shall be considered during the mechanical design phase in order the vacuum system can withstand the "vacuum force". This effect was used by Otto von Guericke in 1654 during the famous demonstration of the Magdeburg hemisphere where several horses could not separate two 55 cm hemispheres held under vacuum.

Table II.8.1: Conversion table between usual pressure units.

Converts to	Pa	Kg/cm^2	Torr	mbar	bar	atm
1 Pa	1	10.2 10^{-6}	7.5 10^{-3}	10^{-2}	10^{-5}	9.81 10^{-6}
1 kg/cm^2	98.1 10^3	1	735.5	980	0.98	0.96
1 Torr	133	1.35 10^{-3}	1	1.33	1.33 10^{-3}	1.31 10^{-3}
1 mbar	100	1.02 10^{-3}	0.75	1	10^{-3}	9.869 10^{-4}
1 bar	10^5	1.02	750	10^3	1	9.869 10^{-1}
1 atm	101 325	1.03	760	1 013.25	1.01325	1

Examples:

1. 1 hPa, 1 hecto Pascal, 100 Pa, is converted to 100×10^{-2} = 1 mbar exactly,
2. 1 bar = 10^5 Pa exactly,
3. 10^{-6} Torr is converted to 1.33×10^{-6} = 1.3 10^{-6} mbar,
4. 10^{-6} Torr is converted to 133×10^{-6} = 1.3 10^{-4} Pa,

5. 4 10^{-6} Pa is converted to 4 10^{-6} × 7.5 10^{-3} = 3 10^{-8} Torr,
6. 4 10^{-6} Pa is converted to 4 10^{-6} / 100 = 4 10^{-8} mbar.

When the molecules circulate in the vacuum vessel, they collide on the wall generating a force, F, with momentum exchange with the wall of surface A. This creates a pressure, $P = F/A$. It can be shown that for any particle velocity distribution, the pressure is given by Eq. II.8.5,

$$P = \frac{1}{3}\,\rho\, v_q^2 \quad , \tag{II.8.5}$$

where ρ is the volumetric mass in kg/m^3 and v_q the quadratic (rms) speed of the molecules in m/s.

If the particle velocity distribution follows a Maxwell-Boltzmann distribution (e.g. at thermodynamic equilibrium), the pressure is given by the **ideal gas law**, Eq. II.8.6. This is a fundamental equation,

$$P = n\,k\,T \quad , \tag{II.8.6}$$

with n the gas density in molecules/m^3, $k = 1.38 \times 10^{-23}$ J/K the Boltzmann constant and T the gas temperature in K. The pressure increases linearly with the gas temperature, i.e. with the thermal speed of the molecules.

In a vacuum system, the gas is usually composed of several types of molecules. The so-called **Dalton's law** expresses the total pressure P_{tot} as the sum of all partial pressures P_i (see Eq. II.8.7). This is another fundamental equation,

$$P_{\text{tot}} = \sum P_i \;=\; k\,T \sum n_i \quad . \tag{II.8.7}$$

II.8.2.2 Gas flow

When the molecules circulate in a vacuum chamber, they may collide between themselves. The mean free path, λ, is defined as the average path length the molecules traverse between two successive collisions. The quantity is given by Eq. II.8.8 (the lower the pressure or gas density, the longer the mean free path)

$$\lambda \;=\; \frac{1}{\sqrt{2}\pi\, n\, \sigma^2} \;=\; \frac{1}{\sqrt{2}\pi}\,\frac{kT}{P}\,\frac{1}{\sigma^2} \quad , \tag{II.8.8}$$

where σ is the molecule diameter in m ($\sim$ 3 Å). For nitrogen gas, the mean free path at room temperature, λ_{N_2}, is given by Eq. II.8.9,

$$\lambda_{N_2}[\text{cm}] \;\approx\; \frac{7 \times 10^{-3}}{P[\text{mbar}]} \quad . \tag{II.8.9}$$

When evacuating a vacuum chamber of an accelerator from atmospheric pressure down to high or ultra-high vacuum (XHV), the mean free path varies from the size of a coronavirus (70 nm) to the perimeter of the Stade de France ($\sim$ 700 m) (HV) or the distance Geneva-Normandy ($\sim$ 700 km) (UHV) i.e., more than 10 orders of magnitude! Consequently, the vacuum level is classified according to Table II.8.2. In accelerator vacuum systems where usually, one operates well below 10^{-7} mbar, the mean free path is well above the km. Note that the XHV regime has been defined by the actual detection limit

of "standard" instrumentation but pressure below this value can be obtained.

Table II.8.2: Vacuum classification.

	Pa	mbar	λ_{N_2}
Low or rough vacuum	10^5 to 10^2	10^3 to 1	70 nm to 70 µm
Medium vacuum	10^2 to 10^{-1}	1 to 10^{-3}	70 µm to 7 cm
High vacuum (HV)	10^{-1} to 10^{-5}	10^{-3} to 10^{-7}	7 cm to 700 m
Ultra-high vacuum (UHV)	10^{-5} to 10^{-10}	10^{-7} to 10^{-12}	700 m to 70 000 km
Extreme-high vacuum (XHV)	$< 10^{-12}$	$< 10^{-14}$	$> 7\,000\,000$ km

Because of the strong variation of the mean free path with the vacuum level, several flows can be established during the pump down of a vacuum system. The turbulent flow is established around atmospheric pressure and immediately after pump down. In the low vacuum regime, the flow is viscous and laminar. In the HV and UHV regime, the flow is molecular. The mean free path is much larger than the vacuum chamber dimensions. In practice, the molecules interact only with the vacuum chamber walls. The **molecular flow** is the main flow regime used in vacuum technology for particle accelerators. In this regime, the molecules have been evacuated from the volume of the vacuum chamber and molecular collisions are very rare or totally absent. Then, the pressure inside the vessel is dominated by the nature of the surface which makes things a lot more interesting but difficult to describe!

In the molecular regime, the molecular flow is modified due to the interaction with the pipe. Following the collision to the wall and due to the roughness of the surface, the molecules are re-emitted according to the Beer-Lambert law. Hence, molecules can be re-emitted in backward or forward direction. Thus, pressure drops are observed along pipes due to their geometry.

The **conductance**, C, is defined as the ratio of the molecular flux Q, to the pressure drop, $P' - P$, along a vacuum vessel, see Eq. II.8.10. The conductance is a characteristic of a vacuum vessel and is a function of their shape, the nature of the gas and its temperature (velocity). This is a fundamental equation,

$$C = \frac{Q}{P' - P} \quad , \tag{II.8.10}$$

where Q is the flow of gas in mbar.l/s and P' (P) the pressure upstream (downstream) to the flow in mbar. The unit is usually expressed is l/s (but SI unit in m^3/s shall be used in the equations!)

When two vacuum vessels of conductance C_1 and C_2 are placed in parallel, the conductance of each pipe is added, whereas when vacuum vessel are placed in series, conductances are inversely added (see Eq. II.8.11),

$$\text{in parallel}: \quad C = C_1 + C_2 \qquad \text{and in series}: \quad \frac{1}{C} = \frac{1}{C_1} + \frac{1}{C_2} \quad . \tag{II.8.11}$$

In molecular regime, the conductance of a (thin) orifice is given by Eq. II.8.12,

$$C_{\text{hole}} = \sqrt{\frac{kT}{2\pi m}} A = \sqrt{\frac{RT}{2\pi M}} A \quad , \tag{II.8.12}$$

with the perfect gas constant $R = kN_A = 8.3145$ J/K/mole, $N_A = 6.0221 \times 10^{23}$ molecules/mole the Avogadro constant and A the surface of the hole in m^2. A practical engineering formula is given for air ($M = 29$ g/mole) at 20°C (~ 300 K), see Eq. II.8.13,

$$C_{\text{hole,air,RT}}[\text{l/s}] \; = \; 11.6 \, A[\text{cm}^2] \quad . \tag{II.8.13}$$

For air at room temperature, the conductance of a 10 cm diameter orifice equals ~ 900 l/s.

In molecular regime, the conductance for a tube of diameter D and length L is given by Eq. II.8.14,

$$C_{\text{tube}} = \frac{1}{6}\sqrt{\frac{2\pi kT}{m}}\frac{D^3}{L} = \frac{1}{6}\sqrt{\frac{2\pi RT}{M}}\frac{D^3}{L} \quad . \tag{II.8.14}$$

To increase the conductance of a vacuum system, it is better to have a vacuum chamber with large diameter and short length since the tube conductance scales like D^3/L.

For air at room temperature, the tube conductance is given by Eq. II.8.15,

$$C_{\text{tube,air,RT}}[\text{l/s}] = 12.1\frac{D[\text{cm}]^3}{L[\text{cm}]} \quad . \tag{II.8.15}$$

For a 10 m long tube of 10 cm diameter, the conductance equals ~ 12 l/s. The tube conductance is much lower than the hole conductance.

The specific conductance is defined as the conductance of a tube of unit length. For a 10 cm diameter tube, it equals 121 l/s.m.

It must be underlined that all conductances scale like $\sqrt{T/M}$, i.e. the conductance is proportional to the velocity. The higher the mass, the lower the conductance.

Exercise 3: what are the conductances at room temperature of a 10 cm diameter orifice and a 10 m long 10 cm diameter tube for H_2 and CO_2?

The **pumping speed** (or volumetric flow rate), S, of a pump is defined as the ratio of the flux of molecules pumped, Q, to the pressure at the pump inlet, P, see Eq. II.8.16,

$$S \; = \; \frac{Q}{P} \quad . \tag{II.8.16}$$

This is a fundamental equation where S is usually expressed in l/s with Q in mbar.l/s and P in mbar.

The **gas throughput** (or gas flow rate), Q, in a vacuum pump is defined by the volume of gas, dV, moving through the pumping inlet per unit of time, dt, multiplied by the pressure at the pump, see Eq. II.8.17,

$$Q \; = \; P\frac{dV}{dt} \; = \; P\,S \quad . \tag{II.8.17}$$

When increasing the pressure over a pump (assuming constant pumping speed), the gas throughput increases linearly. This is a fundamental equation. Hence, the pressure in a vacuum system is simply given by the ratio of the gas load to the pumping speed, see Eq. II.8.18,

$$P = \frac{Q}{S} \quad . \tag{II.8.18}$$

Decreasing the gas load (or outgassing) and/or increasing the pumping speed allows to reach lower pressure. This is a fundamental equation.

The pumping speed of usual pumps range over three orders of magnitude from 10 to 20 000 l/s. However, the specific outgassing rate q (in mbar.l/s/cm^2) of usual materials ranges over 10 orders of magnitude from 10^{-14} mbar./l/s/cm^2 for metallic surfaces to 10^{-5}-10^{-4} mbar.l/s/cm^2 for plastics. Consequently, outgassing must be minimised in vacuum systems to reach UHV.

Remark, the throughput or gas flow rate, i.e. the volume of gas moving through a plane per unit of time multiplied by the pressure, is proportional to the rate of quantity of molecules at constant temperature. Using Eq. II.8.6 and since the gas density $n = n_{\text{molecules}} / V$, Eq. II.8.17 can be written as

$$Q = P\frac{dV}{dt} = n\,k\,T\frac{dV}{dt} = \frac{(n_{\text{molecules}}kT)}{dt} \quad . \tag{II.8.19}$$

The gas flow rate in mbar.l/s is proportional to the number of molecules/s. It has the dimension of J/s, i.e. Watt. Table II.8.3 gives some usual gas flow rate units and their conversions to others.

Table II.8.3: Conversion table between usual gas throughput units.

Converts to	Pa m^3 s^{-1}	Torr l s^{-1}	mbar l s^{-1}	Molecules s^{-1}
1 Pa m^3 s^{-1}	1	7.5	10	2.46 10^{20}
1 Torr l s^{-1}	0.133	1	1.33	3.21 10^{19}
1 mbar l s^{-1}	0.1	0.75	1	2.41 10^{19}

In everyday' s work, the pump cannot always be positioned at immediate proximity of the vacuum vessel to be evacuated. When placing a vacuum pump of pumping speed S, at one extremity of a vacuum system (e.g. a tube) of conductance C, the pressure P' seen at the other extremity is a function of S and C. The gas flow, Q, entering at P' in the vacuum vessel, is conserved along the way and evacuated at the pump with pressure P.

Using Eq. II.8.10 and Eq. II.8.17, the **effective pumping speed**, S_{eff}, can be obtained by identification (see Eq. II.8.20)

$$\begin{cases} Q = P\,S \\ Q = C\,(P' - P) \end{cases} \quad \Longrightarrow \quad Q = \frac{S\,C}{S+C}P' = S_{\text{eff}}\,P' \quad , \tag{II.8.20}$$

where three cases are interesting:

1. when $C = S$ then $S_{eff} = S/2$,
2. when $C >> S$ then $S_{eff} = S$,
3. when $C << S$ then $S_{eff} = C$.

The effective pumping speed seen at the position P' is the result of adding in series the vacuum vessel conductance, C, with the pump pumping speed, S. This concept of effective pumping speed is useful to understand the variation of pressure along accelerator beam pipes, as an example, when dealing with a lumped pumping system. The pumping speed seen at any position along a pipe is reduced by the conductance of this same pipe.

In the last case, the system is said to be "conductance limited". If the conductance of a vacuum vessel is not large enough, the pressure upstream to the vessel will be limited by the conductance irrespective of the value of the pumping speed. Conversely, maximisation of the conductance improves the efficiency of the pumping system. Very large conductances are required to exploit all the benefit of a vacuum pump!

Exercise 4: assume a 10 m long 10 cm diameter vacuum pipe evacuated by a turbomolecular pump of 60 l/s. What is the effective pumping speed? Conclusion?

Conductance limitation is a common feature of all accelerators. For lumped pumping systems, it can be shown that it is useless to increase the pumping speed much beyond 10–20 times the specific conductance of a beam tube unless the distance between pumps is very short ($\sim$ 1 m or less)! A distributed pumping system is routinely used in accelerator vacuum systems to overcome this limitation.

II.8.3 Instrumentation

This section presents the main instruments used in vacuum technology for accelerators. Other specific instruments, mainly for specific or laboratory applications exist but are outside the scope of this lecture. The interested reader may refer to Refs. [3–12].

II.8.3.1 Vacuum gauges

From atmospheric pressure to UHV-XHV, the range of pressure covers 16 orders of magnitude. Obviously, a single vacuum gauge cannot cover such a large range. Around atmospheric pressure down to $\sim 10^{-6}$ mbar, some vacuum gauges respond under a vacuum force meaning that the read signal is a direct measure of the pressure. Bourdon, capacitance, piezo and spinning rotor gauges belong to this category. However, in the XHV, UHV and UV regimes, the signal measured by the gauge is an indirect measurement of the pressure usually via ionisation of the residual gas. Cold and hot cathodes gauges belong to this category.

Pirani gauges are widely used in the accelerator community because of their robustness, their ease of use and their cost. This gauge covering the range from 1 atm to 10^{-4} mbar is therefore suitable to monitor the rough vacuum during a pump down of a vacuum system. The gauge is gas-dependent and its accuracy ranges between 10 and 100%. The operating principle is based on the variation of the heat conductivity of gas as a function of pressure. A resistor under vacuum is heated at a constant temperature ($\sim$ 120°C). The heating current required to keep the temperature constant is an indirect measure of the pressure. In the viscous regime, the thermal conductivity is independent of pressure, hence, pressure reading above 1 mbar are not accurate, (i.e. wrong) [13].

Penning gauges are commonly used in the range 10^{-5} to 10^{-10} mbar. Commercially available

gauges have a magnetron or inverted magnetron design [14, 15]. This robust, gas-dependent gauge is used for interlocking purpose. Its accuracy is 25–50%. It is a cold cathode ionisation gauge. There are no hot filaments and the electrons are produced by field emission ($\sim$ 3 kV). The operating principle is based on the measure of a discharge current I^+ in a Penning cell, which is a function of the pressure, $I^+ = P^n$ with n close to 1. Typical sensitivities are in the range 0.02 A/Pa–0.05 A/Pa. Electrons produced by field emission perform oscillations in a magnetic field of 0.1–0.2 T (perpendicular to the electric field, cross field gauges), to enhance ionisation allowing low pressure measurement. At high pressure, the Penning discharge is unstable and may cause arcing. For this reason, Penning gauges are commonly used in conjunction with Pirani to interlock the Penning gauge at the appropriate pressure. At low pressure, the discharge extinguishes which translate into a zero pressure reading (usually symbolised as UR – under range). Leakage currents along the HV cables and the gauge insulators translate into a high pressure reading.

Bayard-Alpert gauges are hot cathode gauges used for vacuum measurement in the range 10^{-6} – 10^{-12} mbar. This is the common gauge for a laboratory. It is rather accurate with a relative error of 15 to 30 %. Electrons are emitted by a hot filament at + 50 V and perform a few oscillations in a grid held at $\sim$ +150 V. On their way, electrons ionize the residual gas and the ions are collected by a grounded electrode, see Fig. II.8.1.

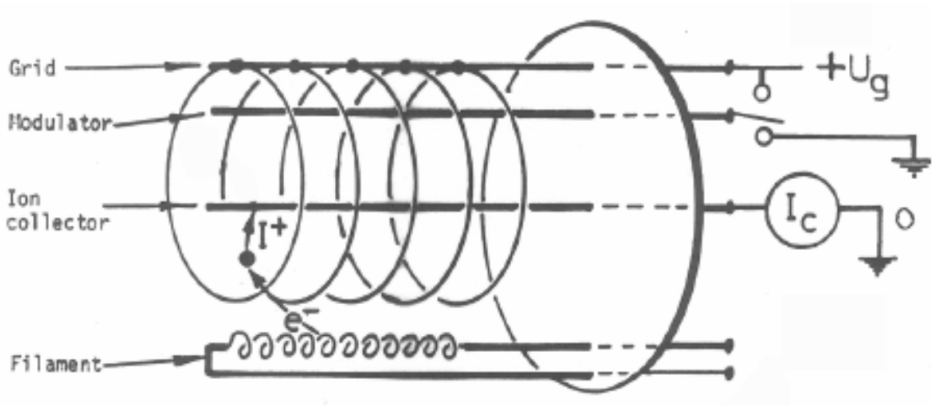

Fig. II.8.1: Schematic of a Bayard-Alpert gauge.

Electrons are produced by a tungsten filament heated above 2 000°C due to thermo-electronic emission according to the Richardson-Dushman equation. Typical electron emission range from 0.1 to 4 mA. To reduce the gas load into the vacuum system originating from thermal desorption, filaments can be coated by Iridium/Yttrium or Thorium to reduce the work function thereby reducing the operating temperature to 1 500°C. During the process, chemical reactions may occur at the hot filament cracking hydrogen, hydrocarbons, oxygen, and water to produce water, hydrocarbons, carbon monoxide, etc., see Ref. [16]. Therefore, the filament produces also a pumping speed of 0.1–1 l/s. It is important that the gauge operates in a clean environment and that the filament remains ON to avoid its contamination.

Hot cathode gauges are metal & glass based hence bake-able up to $\sim$ 400°C. During the bake-out, the electron emission is increased to $\sim$ 50 mA and the gauge is "degassed" under electron stimulated molecular desorption. As a result, the gauge outgassing rate is reduced as low as 5 10^{-10} to

1.5 10^{-9} mbar.l/s. This value can be further reduced to 5 10^{-11} mbar.l/s on a modified Helmer gauge when using thorium coated filament instead of a bare tungsten filament, see [17]. A lower value of 1.6 10^{-11} mbar.l/s was obtained with an extractor gauge (IE 514 Leybold) using a thorium oxide coated iridium wire filament (ThO_2/Ir), see [18].

The electrons oscillating around the grid have an energy of about 200 eV where the ionisation cross section is maximum. Typical cross sections are 4 10^{-17} cm^2 for He, 8 10^{-17} cm^2 for H_2 and 3 $10^{-16}cm^2$ for other gases. The ion collection current, I^+, is given by Eq. II.8.21,

$$I^+ = I_e \sigma\, n\, L = I_e\, S_{\text{gauge}}\, P \quad , \tag{II.8.21}$$

with I_e the electron emission current in A, σ the ionisation cross section in m^2, n the gas density in molecules/m^3 and L the electron path length in m. The gauge sensitivity S_{gauge}, expressed in $mbar^{-1}$, is defined by Eq. II.8.22,

$$S_{\text{gauge}} = \frac{\sigma L}{kT} \quad . \tag{II.8.22}$$

Due to the large variation in cross section, the measured pressure is a strong function of the gas species. Arbitrarily, the pressure reading is expressed in nitrogen equivalent as if the gas composition was only pure nitrogen. The nitrogen sensitivity can be as large as 40 $mbar^{-1}$ for the optimised gauges.

In the low UHV, the typical collected ion current is in the 0.2-20 pA range for 10^{-12} mbar–10^{-10} mbar. The connecting cable must be shielded against electromagnetic perturbation in accelerator environment where the cable length can be as long as a few hundred metres. Triaxial cables are preferred against coaxial cables.

With the emission current fixed, the gauge is calibrated by injecting pure gas at different known pressure levels over several orders of magnitude. The sensitivity is then derived using Eq. II.8.21. Typical sensitivities obtained at CERN following the calibration of more than 100 CERN Bayard-Alpert gauge of type SVT305 are given in Table II.8.4 that gives also the relative sensitivity, $S_{\text{rel},i}$ of a gas i to N_2. The sensitivity relative error is $\sim 10\%$.

Table II.8.4: Typical sensitivities and relative sensitivities of CERN hot cathode gauge.

	H_2	He	CH_4	Ne	N_2	CO	C_2H_6	Ar	CO_2	Xe
S_i [$mbar^{-1}$]	19.06	7.46	60.62	10.48	41.84	42.30	114.71	53.19	54.48	7.50
$S_{\text{rel},i}$	2.20	5.61	0.69	3.41	1.00	0.99	0.36	0.79	0.77	4.83

Exercise 5: assume a baked vacuum system, your Bayard-Alpert gauge reads 2 10^{-10} mbar nitrogen equivalent, what is the true pressure?

In the low UHV, the pressure reading is limited by X-rays, created at the grid by electron bremsstrahlung. A fraction of these photons hit the ion collector emitting a photoelectron that is interpreted as a positive charge by the electron system. This X-ray limit can be measured using a modulator electrode whose potential can be set to the grid voltage. A modulation factor is then measured (~ 0.9) and the X-ray limit evaluated. X-ray limit of CERN Bayard-Alpert gauge equals $\sim 2 \times 10^{-12}$ mbar.

Other hot cathode gauges have been developed over the years to overcome the X-ray and electron stimulated desorption limits. One may cite the Helmer gauge which uses an electrostatically deflected ion beam or the extractor gauge that uses a hidden collector located outside the ionisation region. Both gauges can reach pressures as low as 10^{-13} to 10^{-14} mbar [19].

II.8.3.2 Gas analysis

In general, the gas composition in a vacuum system is not mono-molecular and several species are present. The main gas species are H_2, CH_4, H_2O, CO and CO_2. The major gas is a function of the nature of the surface and its treatment. In practice, unbaked metallic vacuum systems are dominated by H_2O, whereas baked metallic vacuum systems are dominated by H_2. In an accelerator, the relative proportion of the gas species may evolve with beam time. Therefore, it is of paramount importance to evaluate qualitatively and sometime quantitatively the gas composition.

Residual gas analysers (RGA) are used to perform gas analyses. Most of the time, quadrupole mass spectrometers (QMS) are used. They operate in the range 10^{-4} to 10^{-13} mbar.

A filament produces electrons that ionize the residual gas inside a grid. The typical emission current is $\sim$ 1 mA. A mass filter is introduced between the grid and the ion collector. By applying a varying RF voltage on the quadrupole mass filter, a mass scan is obtained with *m/e* varying from 0 to 100 and even 500–5 000 amu (atomic mass unit) for specific QMS. The mass separation at FWHM usually equals 0.5 amu but can be as low as 0.02 amu to distinguish helium and deuterium peaks. Depending on the pressure level, the ion current can be measured directly, using a Faraday cup (for ion current > 10^{-11} A) or indirectly, using a secondary electron multiplier (several discrete Cu-Be dynodes) or a channeltron (a continuous dynode electron multiplier constructed of a semiconductive film deposited on glass) to enhance the ion current by a gain up to 10 000. In the latter case an electron current is measured, and the pressure shall be below 10^{-8}–10^{-7} mbar to avoid a fast degradation of the electron multiplication system accompanied by a loss in gain. Typical voltages applied at the electron multiplier range from 1 400 to 1 600 V. The outgassing rate of the ion source may vary from 2×10^{-9} mbar.l/s for well outgassed grid to 5×10^{-7} mbar.l/s for a non-well outgassed axial ion source.

Ions produced inside the grid can be fragmented into sub species by the collision with electrons producing a so-called "cracking pattern" characteristic of each gas species. Table II.8.5 give a typical cracking pattern in a QMS. For each gas, the table gives the relative percentage of each sub species with respect to the main species (set at 100%).

For instance, H_2, is traced by mass 1 and 2 corresponding to ions H^+ and $H_2{}^+$ with an ion current for H^+ representing 3% of the main peak (mass 2, $H_2{}^+$). Carbon dioxide is traced by masses 44 ($CO_2{}^+$), 28 (CO^+), 16 (O^+) and 12 (C^+) with respectively 13, 16 and 9.7% of the ion current, I_{44}, at mass 44. The presence of hydrocarbons (C_2H_6, C_3H_8), which is indication of a polluted vacuum, is traced by masses in the range 25–27, 29–30 and 39–43.

Although the main peak of CH_4 is 16, this mass can also be attributed to O^+. Like the filaments of hot cathode gauges, QMS filaments produce artefacts that are observed in the mass spectrum, usually 16 and 19 originating from O^+ and F^+. In practice this is identified by checking that the ratio of ion current at mass 15 over 16 is strongly different from 0.85. Hence, for methane it is recommended to follow mass

Table II.8.5: Typical cracking pattern in a QMS showing the relative percentage of each sub species with respect to the main species.

M (uma)	H_2	CH_4	H_2O	N_2	CO	C_2H_6	O_2	Ar	CO_2	C_3H_8
1	3	16.5	2.4			9.6				5.0
2	100									
12		3.0			6.3	0.7			9.7	0.6
13		7.8				1.2				0.9
14		16.0		14	0.8	3.3				2.3
15		85.0				4.7				
16		100	1.8		2.8		18		16.0	
17		1.2	26							
18			100							
20								22.6		
22									2.1	
25						3.8				0.8
26						23.2				9.8
27						33.4				43.5
28				100	100	100			13.0	61.0
29				0.7	1.2	20.0				100
30						22.2				21.7
31										
32							100			
34							0.4			
36								0.34		
37										4.6
38								0.06		6.7
39										20.2
40								100		2.6
41										15.0
42										4.8
43										22.8
44									100	24.0
45								1.2		0.8

15 instead of 16.

The spurious signals usually originate from electrons emitted from the filament stimulating neutrals and ions desorption. Spurious signal at masses 1, 16, 19, 35 and 37 are due to low energy ions (1 eV) of H^+, O^+, F^+ and Cl^+ following electron impact desorption (EID) of ions from pre-adsorbed surfaces [3]. An estimation of the EID background is done by decreasing from 12 to 1 V the voltage along the field axis in the ionisation chamber ("field axis").

For UHV and after bakeout to 300-400 ^{0}C, degassing a grid ion source is a good practice to reduce spurious signals. This is achieved by using an intense (20 mA) and energetic (500 eV) electron bombardment emitted from the filament,

Exercise 6: a mass spectrum shows a large peak at mass 28 but no signal at mass 14, how to disentangle between nitrogen and carbon monoxide?

In an unbaked vacuum system, the mass spectrum is dominated by H_2O^+, i.e. mass 18 originating from the outgassing of water vapour.

In a baked vacuum system, the mass spectrum is dominated by $H_2{}^+$, i.e. mass 2 originating from the hydrogen outgassing from the material. Other gas species such as CO (mass 28) or CO_2 (mass 44) are one order of magnitude lower. The partial pressure of hydrogen represents 96% of the total pressure.

The QMS needs to be calibrated against a total pressure gauge to provide a quantitative analysis of a mass spectrum, see e.g. Ref. [20]. In-situ calibration is recommended where possible. To do so, a pure gas, *i*, is admitted in the UHV system to measure the QMS sensitivity. Since the QMS signal strongly depends on the voltage applied at the secondary electron multiplier whose gain may vary with time, a relative sensitivity $S_{\mathrm{rel},i,\mathrm{RGA}}$ of the gas to N_2 is used, see Table II.8.6. Once adjusted and calibrated, the parameters of the QMS shall not be modified. Calibration checks shall be routinely performed.

According to the Dalton law, the reading of the total pressure gauge shall be equal to the sum of the partial pressures. This leads to Eq. II.8.23,

$$P_i \;=\; S_{\mathrm{rel},i}\frac{S_{\mathrm{rel},i,\mathrm{RGA}}}{\sum_{j=1}^{n} S_{\mathrm{rel},j,\mathrm{RGA}} \times I_j} P_{\mathrm{N_2}}\, I_i \quad . \tag{II.8.23}$$

The equation expresses the partial pressure of a gas, i, as a function of the relative sensitivity of the total pressure gauge and the one of the QMS, the measured total pressure expressed in nitrogen equivalent and the current, with P_i the partial pressure of gas i, $S_{\mathrm{rel},i}$ the relative sensitivity of the total pressure gauge for the gas i (see Table II.8.4), $S_{rel,i,RGA}$ the relative sensitivity of the QMS for the gas *i* (see Table II.8.6), $S_{\mathrm{rel},i,\mathrm{RGA}}$ the relative sensitivity of the QMS for all the gas j measured in the spectrum, I_j the current for all the gas j measured in the spectrum, $P_{\mathrm{N_2}}$ the total pressure measured by a total pressure gauge expressed in nitrogen equivalent and I_i the current of the gas i to be evaluated.

Table II.8.6: Typical relative sensitivities of a QMS.

	H_2	CH_4	N_2	CO	Ar	CO_2
$S_{\mathrm{rel},i,\mathrm{RGA}}$	2.20	0.69	1.00	0.99	0.79	0.77

Exercise 7: for a baked system with $P_{\mathrm{N_2}}$ = 10^{-10} mbar, the mass spectrum contains peaks at mass 2, 15, 28, 40 and 44. Which molecules are seen in this vacuum system? Why? The measured currents are $I_2 = 1 \times 10^{-9}$ A, $I_{15} = 2 \times 10^{-12}$ A, $I_{28} = 7 \times 10^{-11}$ A, $I_{40} = 5 \times 10^{-13}$ A and $I_{44} = 2 \times 10^{-11}$ A. Determine the partial pressures.

Applying Eq. II.8.23 and using the total and partial pressures gauges relative sensitivities in Tables II.8.4 and II.8.6, one computes the following $P_{\mathrm{H_2}}$ = 2 10^{-10} mbar, $P_{\mathrm{CH_4}}$ = 1 10^{-13} mbar, P_{CO} = 6 10^{-12} mbar, P_{Ar} = 4 10^{-14} mbar and $P_{\mathrm{CO_2}}$ = 3 10^{-12} mbar.

Finally, QMS can be used to identify and detect leaks in vacuum systems. Indeed, traces of N_2 and Ar are usually the signature of air leaks (air is composed by 78% N_2, 20% O_2 and 1% Ar). Oxygen being highly chemically reactive its mass is not always present in the mass spectrum to the expected level.

II.8.3.3 Vacuum pumps

Like vacuum gauges, the pumping devices shall cover 16 orders of magnitude to pump down from atmospheric pressure to UHV. Hence, a single type of pump cannot be used. Some pumps are used to evacuate the vessel and others to maintain a vacuum. One can distinguish pumps that remove the molecules from the vessel such oil sealed mechanical pumps or turbomolecular pumps and pumps that capture the molecules such as sputter ion pumps, cryopumps, getter pumps, etc. In the latter category, the molecules remain in the vacuum system and they may be re-desorbed inside the vessel under specific circumstances. In this section, we discuss only primary pumps, turbomolecular and sputter ion pumps that are routinely used in vacuum technology.

Oil sealed rotary vane pump is a primary pump that is used to pump down from atmosphere to 10^{-2} mbar. Depending on the vessel size, their pumping speed ranges from 3 to some 100 m^3/h. These pumps are used as backing pump of turbomolecular pumps, in accelerators technology 12 m^3/h is usually sufficient. While a rotating vane pump extracts gas from the inlet, traps it, compresses it and releases it at the exhaust. The wet pump operates with oil which acts as a sealing, a lubricant, a heat exchanger and protects the mechanical parts from rust and corrosion.

Turbomolecular pumps operate in the molecular regime. They are routinely used during the commissioning phase of a vacuum sector in an accelerator. A 60 l/s turbomolecular pump is usually installed on a trolley together with a primary pump in such a way the assembly can be removed after the vacuum sector commissioning and used to commission the next sector.

The ultimate pressure of such pump can be as low as 10^{-11} mbar with a pumping speed ranging from 10 to 30 000 l/s. The pumping speed is about constant over the full range of operation. The pumping mechanism is based on the transfer of momentum. When a molecule collides with a blade, it is adsorbed for some duration. After re-emission, the blade speed is added vectorially to the thermal speed of the molecules (see Eqs. II.8.1 and II.8.2). So, to be significant, the blade speed must be comparable to the thermal speed hence it requires fast moving surfaces (i.e. $\sim$ 40 000 turns/min). During this process, the molecules are evacuated from the pump inlets to the outlet where a primary pump is taking care of them. The compression ratio ($P_{\text{inlet}}/P_{\text{outlet}}$) of these pumps increase exponentially with $\sqrt{M}$. Thus, such pumps produce a clean vacuum without leaving heavy masses such as hydrocarbons.

Sputter ion pumps operate in the range 10^{-5} to 10^{-11} mbar. This capture pump is used to maintain the pressure in the vacuum chamber of an accelerator after the commissioning of the vacuum sector (in the LHC room temperature sections, NEG (Non-Evaporable-Getters) complement the pumping). The pump has no exhaust and traps the gas species. Typical pumping speeds range from 1 to 500 l/s (but 1 000–2 000 l/s custom models exist). The pump is made of several Penning cell (anode) assembled and placed in a magnetic field (0.1–0.2 T). During operation electrons (that are always present in a system) ionize the residual gas along their trajectory curved by the magnetic field. The ions are accelerated at $\sim$ 5 kV towards the cathode plates made of titanium. Ti is then sputtered (i.e. deposited onto the surface) and being a getter material, forms chemical bonds with the molecules of the residual gas. At high pressure, many ions are created which sputter large quantities of Ti enabling large pumping speed, whereas at low pressure, lower quantity of Ti is sputtered. Consequently, the lower the pressure the lower the pumping speed enabling a longer pump lifetime owing to the reduction of the cathode erosion. Noble

gases and hydrocarbons that cannot be pumped by the getter mechanism are buried or implanted onto the cathode. Beside their robustness while operating in UHV, the ion current measured in this pump is proportional to the pressure, providing additional pressure reading along the accelerator. In addition, this signal can be used in the beam interlock chain in place of vacuum gauges.

II.8.4 Outgassing

We have seen in Section II.8.2 that the pressure in a vacuum system is given by the ratio of the gas load to the pumping speed (see Eq. II.8.18). In absence of leaks, the gas load is usually originating from the outgassing of the surface materials into the vacuum vessel, the so-called thermal desorption or thermal outgassing usually shortened to "outgassing".

Equation II.8.19 showed that the gas throughput is proportional to a rate of quantity of molecules. What are the involved quantities? What do they represent? Using Eq. II.8.6 and since the gas density $n = n_{\text{molecules}}/V$, one obtains Eq. II.8.24,

$$P\,V \;=\; n_{\text{molecules}} k\,T \qquad . \tag{II.8.24}$$

Hence, at room temperature (300 K), 1 mbar.l is equivalent to 2.4 10^{19} molecules (or 1 Torr· l is equivalent to 3.2 10^{19} molecules). Then, for any temperature,

$$1\,\text{mbar}\cdot\text{l} \Leftrightarrow \frac{7.25\times10^{21}}{T} \quad \text{and} \quad 1\,\text{Torr}\cdot\text{l} \Leftrightarrow \frac{9.64\times10^{21}}{T} \qquad . \tag{II.8.25}$$

The quantity 1 mbar·l represents a huge quantity of molecules!

Exercise 8: imagine a 10 m long beam pipe of 10 cm diameter with 1 mbar·l of molecules adsorbed on its surface. What would be the pressure if all this amount of molecules are desorbed?

Several types of materials are used for the construction of vacuum systems. Metals for vacuum vessels such stainless steels (304L, 316LN grade, etc.), Cu alloys (OFE, OFS, etc.), Al alloys or Be (for the experimental beam pipes) are widely used for the fabrication and construction. The choice of the material is a function of the required properties of the system, machinability, weldability, thermal / electric conductivity, particle transparency, corrosion robustness, mechanical stability, cost, etc. [12]. Insulating materials are also used for instrumentation, metrology or assembly purposes. These might be minerals such as ceramics, glass, Macor® ... or polymers (plastics) such as glues, Kapton®, PEEK (polyether-ether-ketone), Teflon (PTFE, polytetrafluoroethylene), elastomers (Viton®, Neoprene, EPDM, etc.).

During the manufacturing process of all these materials, atoms and molecules are absorbed on the material surface (adsorption) or in the bulk (absorption). All these particles are readily available for outgassing into the vacuum vessel. In addition, the surface of a material can be very rough and the porosity of the materials increases further the outgassing rate.

Quantities of adsorbed gases in the material can be extremely large. Indeed, 1 cm^3 of stainless steel can contain 0.05–0.5 mbar · l of hydrogen and nylon (a polyamide plastic) can lose 4% of its weight under vacuum, i.e. 5 mbar.l per cm^3.

Understanding and accessing the outgassing properties of materials used in vacuum science and

technology is therefore of paramount importance.

II.8.4.1 Elements of adsorption / desorption

During the pump down, one distinguishes several phases: 1) volume pumping, 2) surface desorption, 3) bulk diffusion and 4) permeation through the wall. Figure II.8.2 shows the *P* - *t* plots for the pumping down of a 1 m long, 10 cm diameter stainless steel pipe with a pumping speed of 30 l/s.

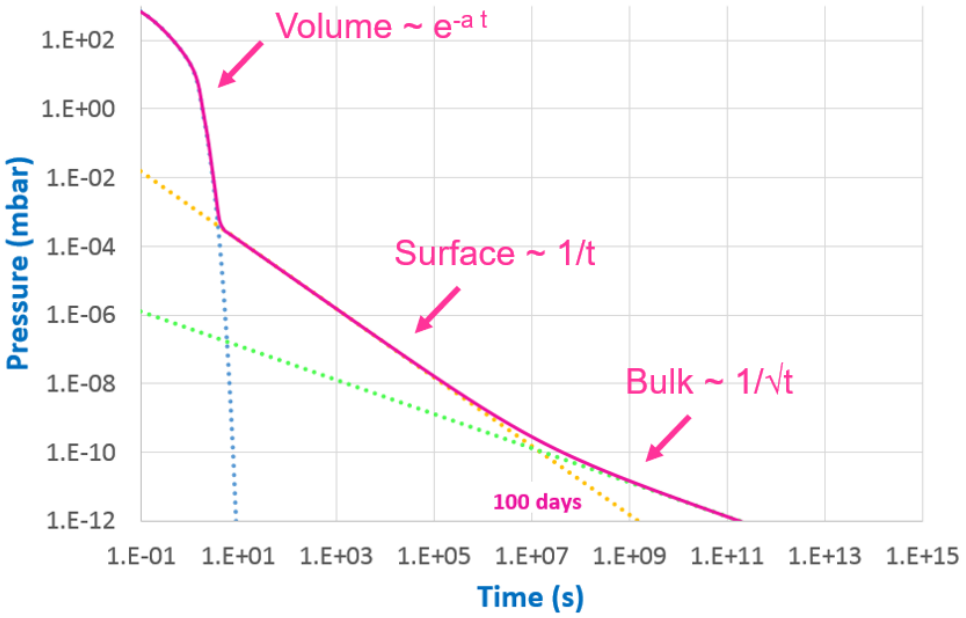

Fig. II.8.2: Long-term pump down of a stainless steel tube.

Volume pumping follows an exponential law that scales like e^{-at} with $a = \frac{S}{V}$. This is a rather fast process and after 10 s all the molecules from the vacuum tube volume have been fully evacuated.

Surface desorption scales like the inverse of time. It originates from the water vapour that outgasses from the material surface. As shown, the process is very long and slows down the entire pumping process. After one day (10^5 s), the pressure reaches 10^{-8} mbar and 10^{-9} mbar one month later. Around 6 months (10^7 s) are required to remove the water from the surface to reach 10^{-10} mbar.

After this long period, hydrogen diffusion from the bulk is taking over. The diffusion process scales like the inverse of the square root of time. Hence, accessing the low UHV requires several decades and is clearly not accessible without specific precautions and material treatments.

Permeation trough the wall is (in principle) negligible for metallic surface (unless presence of cracks in the material). Helium is a concern for vacuum system built with materials like glass and quartz, used often in the past and in laboratories. He permeation concerns only polymers materials and is present for instance at rubber gaskets used for insulation of vacuum systems.

The material shall then be seen as a (infinite) source of molecules. Depending on the origin of those molecules, adsorption, absorption, diffusion or permeation, the outgassing rate changes.

The adsorption-desorption process is driven by the interaction energy between a molecule (or

atom) with the surface. Weakly bound molecules are physisorbed on the surface (binding energy $\sim$ 0.1 eV) and strongly bounded molecules are chemisorbed at the surface (binding energy $\sim$ 1 eV). Physical adsorption involves van der Waals intermolecular forces. Several monolayers of gas can be physisorbed on a surface. Chemical adsorption involves transfer of the electrons between atoms. Chemisorption can be dissociative (e.g. H_2) and non-dissociative (e.g. C=O). A single monolayer can then be adsorbed at the surface.

Thermal desorption follows the Polanyi-Wigner equation, that expresses the desorption rate, r (or change of surface coverage), as a function of the adsorption energy and the order of desorption,

$$r = -\frac{d\theta}{dt} = \nu_{\mathrm{n}}\,\theta^n e^{-\frac{E_D}{kT}} \quad , \tag{II.8.26}$$

with θ the surface coverage, ν_{n} the pre-exponential factor, frequency of vibration of an adsorbed molecule ($\sim 10^{13}$ Hz) for desorption order n, E_D the activation energy for desorption.

The order of desorption (or kinetic order) and the desorption energy can be evaluated from temperature programmed desorption (TPD) or thermal desorption spectroscopy (TDS): 0^{th} order occurs for thick layers of ice; 1^{st} order desorption is applicable for physisorbed molecules and non-dissociated chemisorbed molecules; 2^{nd} order desorption is applicable for dissociatively chemisorbed molecules (H_2, N_2, O_2) on metals [21]. For a first order desorption, $n = 1$, the solution of the equation is

$$\theta(t) = A\, e^{-\frac{t}{\tau}} \quad , \tag{II.8.27}$$

with the time constant τ usually called sojourn time or residence time. The sojourn time of a molecule on a surface is a function of the desorption energy and the temperature of the surface,

$$\tau = \tau_0\, e^{\frac{E_D}{kT}} \quad , \tag{II.8.28}$$

where τ_0 is the oscillation period of the molecule on the surface (10^{-13} s). The inverse of the sojourn time is the desorption probability of a molecule.

For some binding energies, the sojourn time of a molecule is in the order of a week. But increasing the surface temperature decreases the residence time: this is called a bakeout. Decreasing the surface temperature, increases the residence time: this is called cryopumping. Conversely, strongly bound molecules have long residence time and may stay on the material surface for very long period before desorbing.

The activation energy can be evaluated by TDS. In this case, a temperature ramp is applied to the surface with several heating rate β: $T = T_0 + \beta t$. The maximum temperature, T_P, of the desorption rate is recorded for the different heatings. A plot in $\ln(\beta/T_P^2)$, $1/T_P$ coordinates gives a straight line with slope proportional to the activation energy [22, 23].

II.8.4.2 Unbaked systems

The (intrinsic) specific outgassing rate is the quantity of gas leaving the surface per unit of time and per unit of exposed geometrical surface. The SI unit is Pa·m^3·s^{-1}·m^{-2} (or Pa·m/s or W/m^2). Several units can

be used and found in textbooks. Table II.8.7 shows the conversion factor for usual specific outgassing rate units [24].

Table II.8.7: Conversion table between usual specific outgassing rate units.

Converts to	Pa m s^{-1}	Torr l s^{-1} cm^{-2}	mbar l s^{-1} cm^{-2}	Molecules s^{-1} cm^{-2}
1 Pa m s^{-1}	1	$7.5\ 10^{-4}$	10^{-3}	$2.46\ 10^{16}$
1 Torr l s^{-1} cm^{-2}	$1.33\ 10^{3}$	1	1.33	$3.27\ 10^{19}$
1 mbar l s^{-1} cm^{-2}	10^{3}	0.75	1	$2.46\ 10^{19}$

Examples:

1. $3\ 10^{-10}$ Torr l / (s cm^2) is converted to $1.33\ 10^{3} \times 3\ 10^{-10} = 4\ 10^{-7}$ Pa m s^{-1},
2. $5\ 10^{-13}$ Torr l s^{-1} cm^{-2} is converted to $1.33 \times 5\ 10^{-13} = 6.7\ 10^{-13}$ mbar l s^{-1} cm^{-2},
3. $5\ 10^{-15}$ mbar l s^{-1} cm^{-2} is converted to $2.46\ 10^{19} \times 5\ 10^{-15} = 123\,000$ molecules s^{-1} cm^{-2}.

Water is always present in vacuum systems. It originates from previously adsorbed molecules and from reactions with oxides ($Fe_xO_y + 2H \rightarrow Fe + H_2O$).

Figure II.8.3 shows the sojourn time of molecules on metallic surface as function of temperature. At room temperature (20°C), the sojourn time of hydrogen on stainless steel is a few minutes hence hydrogen is promptly evacuated during pump down. Conversely, the sojourn time of carbon monoxide is very large ($\sim$ 1 year) because the molecule is strongly bound to the surface and cannot be thermally desorbed at ambient temperature.

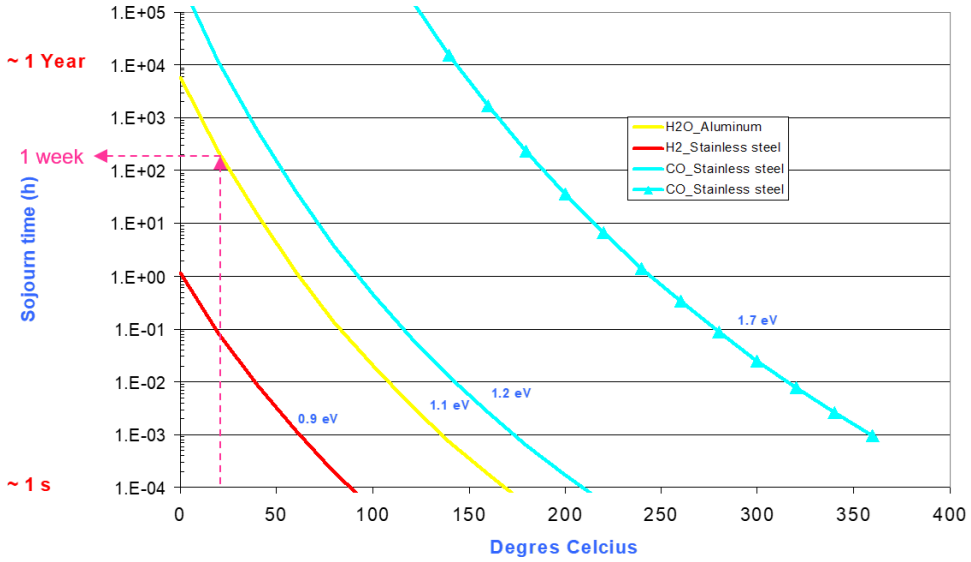

Fig. II.8.3: Sojourn time of molecules on metallic surfaces as a function of temperature.

At room temperature and for unbaked vacuum systems, the sojourn time of water on the surface is very large ($\sim$ 1 week). Thus, the surface coverage of water is reduced by $1/e$ in a week, see Eq. II.8.27. Water desorption is therefore the dominating factor of the pumping process, several months of pumping

are required to evacuate the adsorbed water from the surface. However, a mild bakeout to 120°C for a couple of hours is enough to remove most water from the surface and the vacuum system.

It is observed that the desorption of water follows a universal inverse power law with $a \sim 1$ for metals and metal oxides,

$$q(t) = q_0\, t^{-a} \quad , \tag{II.8.29}$$

with q_0 the initial outgassing rate of water. In practical units, the specific outgassing rate is given by Eq. II.8.30,

$$q(t) = \frac{3\,10^{-9}}{t[\mathrm{h}]}\,[\mathrm{mbar.\,l\,s^{-1}\,cm^{-2}}] \quad . \tag{II.8.30}$$

Exercise 9: consider a 10 m long unbaked beam tube of 10 cm diameter evacuated by a pump of 30 l/s. What is the pressure after one day, one week and one month of pumping?

Although there is not a detailed understanding of the outgassing phenomena, some models have been derived to describe phenomenologically the observed pressure. A recent one assumes that the desorption/adsorption of water is reversible. Using Temkin-like isotherms with several possible adsorption energies sites, in the range 0.6–1 eV, the $1/t$ behaviour observed during the pump down could be rather well reproduced [25].

One observes that the coefficient in Eqs. II.8.29 and II.8.30 is a function of the roughness of the surface. Indeed for rough surfaces the factor is increased. For instance, the coefficient is multiplied by $\sim$ 30 when comparing a stainless steel surface to a thick carbon coated tube ($\sim$ 500 nm). Conversely, mechanical polishing or electropolishing are techniques applied to reduce the outgassing rate of materials.

Sometimes it may be required to vent a vacuum system, that has been evacuated from its water for a long pumping period, back to atmosphere (for example for maintenance purpose). A thorough study was conducted to measure the effectiveness of different venting methods in terms of speed of vacuum recovery after a venting [26]. The study showed that venting with highly dry nitrogen gas was the best method: almost no water was absorbed on the surface following this technique. In this way, the base pressure could be recovered rather quickly in less than two hours. This venting method is indeed a long-standing good practice in vacuum technology.

Table II.8.8 gives typical values of outgassing (in Torr·l/s/cm^2) of some unbaked technical surfaces used for the construction of vacuum systems. Values are similar for Al, Cu and stainless-steel. As shown in Fig. II.8.4, the gas composition in an unbaked vacuum system is dominated by water, but other molecules are also present, with hydrogen as the second important species and hydrocarbons at lower content with traces of oil contamination (alkanes C_nH_{2n+2}).

II.8.4.3 Baked systems

As said above, a way to reduce the sojourn time of water is to increase the temperature of the surface for some time. Of course, the heating of a material is possible if its mechanical property is kept. Hence, Cu and Al alloys are usually baked up to $150 - 200$°C whereas stainless steel materials can be baked to

Table II.8.8: Outgassing value in Torr.l/s/cm^2 of some unbaked technical surfaces after 10 h pumping [27].

Gas	Al	Cu	Stainless steel	Be
H_2	$7\ 10^{-12}$	$1\ 10^{-11}$	$7\ 10^{-12}$	$1\ 10^{-11}$
CH_4	$5\ 10^{-13}$	$5\ 10^{-13}$	$5\ 10^{-13}$	$1\ 10^{-12}$
H_2O	$3\ 10^{-10}$	$3\ 10^{-10}$	$3\ 10^{-10}$	$6\ 10^{-10}$
CO	$5\ 10^{-12}$	$1\ 10^{-12}$	$5\ 10^{-12}$	$1\ 10^{-11}$
CO_2	$5\ 10^{-13}$	$3\ 10^{-13}$	$5\ 10^{-13}$	$1\ 10^{-12}$

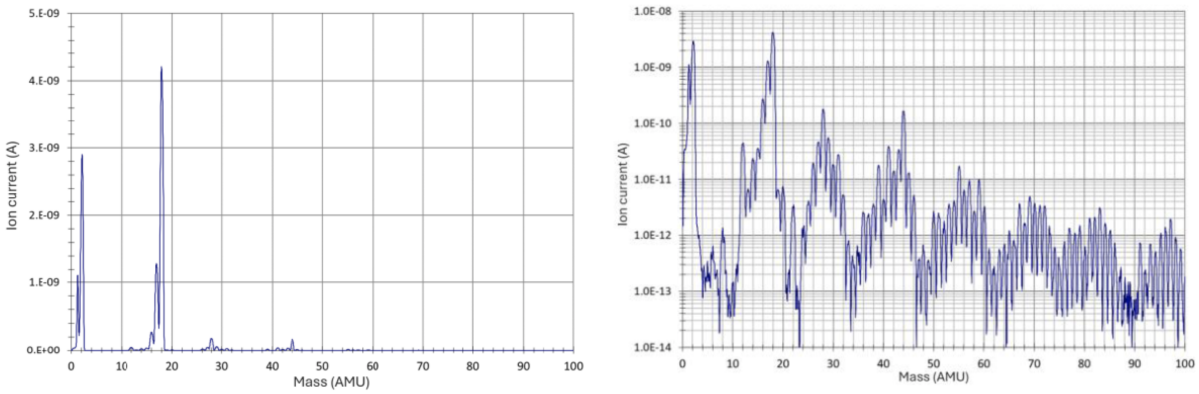

Fig. II.8.4: Gas analysis of an unbaked system at 4 10^{-9} mbar, left linear scale, right log-linear scale (data courtesy B. Jenninger, TE-VSC-VSM).

300–400°C. A bakeout of Cu and Al allows to remove all molecules with binding energies below 1.7 eV and up to 2 eV for stainless steel materials. Molecules with larger binding energy will not be depleted by a bakeout but will remain available for subsequent desorption under ion bombardment for instance.

In daily work, a bakeout above 130–150°C is used to remove water from a vacuum vessel in such a way that hydrogen becomes the dominant gas, see for instance the example of Al [28]. Collars, heating tape, insulating material, bakeout jackets, thermocouples are equipment used to perform a bakeout in accelerators. Heating ramps of 50°C/h are applied and controlled by a dedicated control system that can manage several channels. All parts of the accelerator exposed to vacuum shall be baked, including in-vacuum assemblies. Cold spots are forbidden because they will become a source of outgassing after the bakeout. A typical bakeout sequence consist of $\frac{1}{2}$ half day for temperature ramping, 24 h (or a night) at plateau and $\frac{1}{2}$ day temperature decrease with the degassing of the vacuum instruments on the way. A leak test shall be performed at the end of the bakeout and the ultimate pressure recorded two days after baking when the entire vacuum system is back to room temperature.

Table II.8.9 gives typical values of outgassing (in Torr·l/s/cm^2) of baked technical surfaces used for the construction of vacuum systems [27]. Values are given after 50 h of pumping for Al, Cu baked at 150°C and stainless-steel at 300°C.

As shown, hydrogen dominates the residual gas composition after baking. The bakeout reduces water outgassing by four orders of magnitude. Other species are reduced by one to three orders of magnitude.

During the bakeout, several monolayers of gas are removed from the surface material and evacu-

Table II.8.9: Outgassing value in Torr·l/s/cm^2 of some baked technical surfaces after 50 h pumping [27].

Gas	Al	Cu	Stainless steel	Be
H_2	5 10^{-13}	1 10^{-12}	5 10^{-13}	1 10^{-12}
CH_4	5 10^{-15}	5 10^{-15}	5 10^{-15}	1 10^{-14}
H_2O	1 10^{-14}	< 1 10^{-15}	1 10^{-14}	2 10^{-14}
CO	1 10^{-14}	1 10^{-14}	1 10^{-14}	2 10^{-14}
CO_2	1 10^{-14}	5 10^{-15}	1 10^{-14}	2 10^{-14}

ated by the turbomolecular pump. A total of 28.8 monolayers was measured after a laboratory bakeout of a stainless steel chamber at 200°C for 20 h, 11 monolayers for H_2, 0.7 for CH_4, 7 for H_2O, 4.4 for CO and 5.7 for CO_2 [29].

A model of diffusion based on the 1st and 2nd Fick laws (see Eq. II.8.32) can be used to explain the hydrogen outgassing in materials. It makes use of the diffusion coefficient, see Eq. II.8.31, that is a strong function of the diffusion energy and temperature,

$$D(T) = D_0\, e^{-\frac{E_{\text{diff}}}{kT}} \quad , \tag{II.8.31}$$

with D_0 a diffusion constant depending on the material, E_{diff} the activation energy for the diffusion process and T the temperature. For 304L and 316 L stainless steel, $D_0 = 5.8 \times 10^{-3}$ cm^2/s and $E_{\text{diff}} = 0.558$ eV [30].

For a one dimensional object along x: 1) the 1st Fick law says that the gaseous flux, q, is equal to the product of the diffusion coefficient, D, by the gradient of hydrogen concentration, c; 2) the 2nd Fick law says that the time variation of the hydrogen concentration along the solid is equal to the product of the diffusion coefficient by the second derivative of the hydrogen concentration in the solid,

$$\begin{aligned} q(x,t) &= -D\,\tfrac{\partial c(x,t)}{\partial x} \quad , \\ \tfrac{\partial c(x,t)}{\partial t} &= D\,\tfrac{\partial^2 c(x,t)}{\partial x^2} \quad . \end{aligned} \tag{II.8.32}$$

During a pump down, the hydrogen concentration on the surface ($x = 0$) and in the material is reduced with time. The time variation of the hydrogen concentration can be computed using the second law which allows to compute the hydrogen outgassing rate from the first law. It can be demonstrated that the hydrogen outgassing rate, q, after a pumping time t is given by Eq. II.8.33 (see also Ref. [31]),

$$q(t) = -D\left(\frac{\partial c(x,t)}{\partial x}\right)_{x=0} = c_0\sqrt{\frac{D}{\pi}}\,\frac{1}{\sqrt{t}} \approx \sqrt{D}\,t^{-\frac{1}{2}} \quad , \tag{II.8.33}$$

with c_0 the initial hydrogen concentration assumed to be uniform within the solid. Consequently, a very important observation is made: the hydrogen outgassing rate varies inversely with the square root of pumping time. During the pump down, the hydrogen naturally embedded into the material is depleted from it. Hence, re-exposure to air does not recharge the bulk.

During an (in-situ) bakeout, the temperature of the material is increased to several hundred degrees (T_{BO}) for several hours (t_{BO}) in such a way that the hydrogen diffusion inside the material is increased to stimulate its depletion from it. It can be demonstrated that after a bakeout, the hydrogen outgassing

Table II.8.10: Equivalence between bakeout temperature and duration for stainless steel.

200°C	250°C	300°C
1 day	7 h	2 h
4 days	1 day	8 h
10 days	2 days	1 day

rate in a material of thickness, L, is almost constant and given by Eq. II.8.34 (see also Refs. [31, 32]),

$$q_{\mathrm{RT}}(t) \approx \frac{4\, c_0\, D(T_{\mathrm{RT}})}{L}\, e^{-\left(\frac{\pi}{L}\right)^2 D(T_{\mathrm{BO}})\, t_{\mathrm{BO}}} \quad . \tag{II.8.34}$$

The equation above shows that it is more efficient to increase the temperature of the bakeout, due to the diffusion term, than to increase the bakeout duration time.

Table II.8.10 gives for stainless steel, the equivalence for different bakeout temperatures and durations. A bakeout at 300°C during a night is equivalent to four days of bakeout at 200°C. It is important to properly design a vacuum system to withstand high bakeout temperatures to gain time and minimise the risk of a power cut during the bakeout process.

Figure II.8.5 shows a typical gas analysis obtained after baking. The reached pressure equals 4×10^{-11} mbar. The mass spectrum is a clean one dominated by H_2 with traces of H_2O, CO and CO_2. No contamination above mass 50 is seen. Spurious peaks at mass 16 (O^+) and 19 (F^+) due to the grid bombardment by the electrons emitted by the filament are seen.

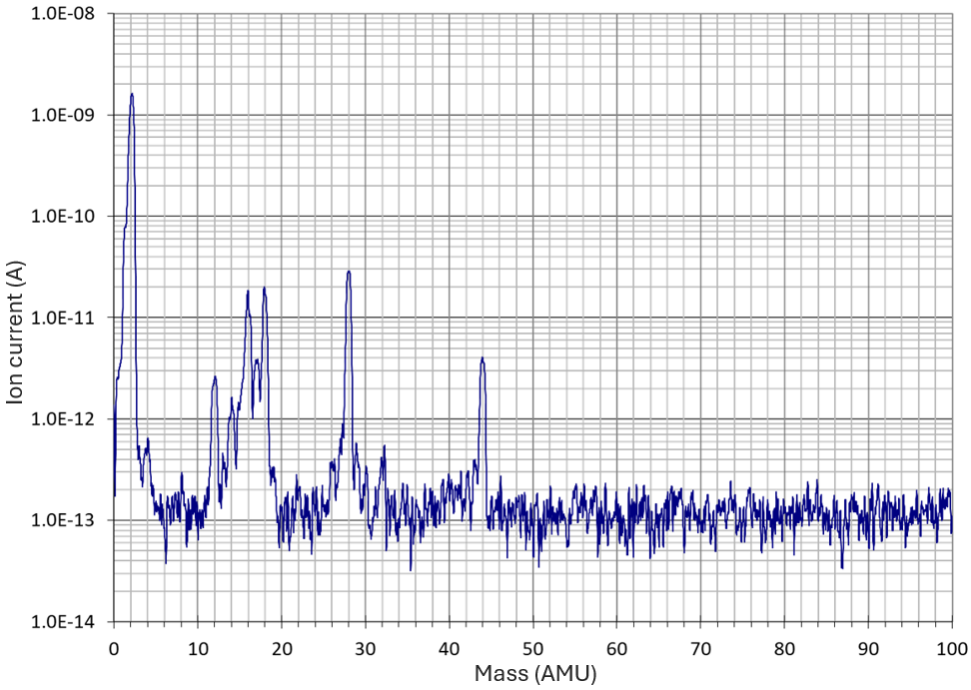

Fig. II.8.5: Gas analysis after baking (data courtesy B. Jenninger, TE-VSC-VSM).

Successive bakeouts of a vacuum system reduce further the outgassing rate. The outgassing rate at

the bakeout cycle n is given by Eq. II.8.35. A plot of $\ln(q)$ versus the number of bakeout cycles is linear with a slope proportional to the diffusion coefficient [32],

$$q_n(t) \;=\; \frac{4\,c_0\,D(T_{\mathrm{RT}})}{L}\;e^{-n\left(\frac{\pi}{L}\right)^2 D(T_{\mathrm{BO}})\,t_{\mathrm{BO}}} \quad . \tag{II.8.35}$$

Hence, the ratio between two successive bakeout cycles given by Eq. II.8.36 is constant. Each bakeout cycle reduces the outgassing rate at room temperature by a constant value experimentally evaluated to 1.3–1.5 for stainless steel or a complex object like a collimator [32, 33],

$$\frac{q_{n+1}(t)}{q_n(t)} \;=\; e^{-\left(\frac{\pi}{L}\right)^2 D(T_{\mathrm{BO}})\,t_{\mathrm{BO}}} \quad . \tag{II.8.36}$$

Finally, is worth remembering that due to the diffusion term, the outgassing rate of a baked material follows an Arrhenius law,

$$q(T) \;=\; q_0\,e^{-\frac{E}{k}\frac{\alpha}{T}} \quad . \tag{II.8.37}$$

The higher the operating temperature, the higher the outgassing rate. A plot of $\ln(q)$ versus $1/T$ gives a straight line whose slope is proportional to the activation energy.

The activation energy of baked stainless and vacuum fired stainless steel measured in the laboratory equals 0.5 and 0.4 eV respectively. Table II.8.11 gives the outgassing rate increase with respect to 20°C for different operating temperatures. As experienced by many users of vacuum technology, the pressure level measured in a non-climatised laboratory is sensitive to day and night temperatures! In accelerators, irradiation of components by stray particles, e.g. collimators, also provokes an increase of the base pressure. For this reason, the temperature of such devices may be interlocked to moderate the beam-induced pressure increase.

Table II.8.11: Outgassing rate increase with respect to room temperature set at 20°C.

	10°C	30°C	50°C	100°C	150°C
Baked stainless steel	0.5	2	5	70	450
Vacuum fired stainless steel	0.5	2	5	30	150

Exercise 10: consider a 10 m long stainless steel beam tube of 10 cm diameter evacuated by a pump of 30 l/s. What is the pressure after a bakeout at 300°C? Conclusion?

II.8.4.4 Hydrogen reduction

A method to reduce the hydrogen content in stainless steel (316 series) is to degas the material in an oven at 950°C under vacuum (<10^{-5} mbar) for two hours, a so-called "vacuum firing" treatment. The high temperature strongly promotes the hydrogen diffusion within the solid. Hydrogen then reaches the surface of the solid before degassing and being evacuated by the pumping system. CERN is equipped with a large furnace of 1 m diameter and 6 m length [12]. It can be loaded up to 1 Ton to vacuum fire a large quantity of material per cycle. After vacuum firing, the hydrogen concentration is reduced from 2×10^{19} to 10^{18} H/cm^3 [34]. Because of the heating, low carbon and low carbon nitrogen alloys stainless

steel shall be used such as 316 LN (304 series are recrystallised due to carbide precipitation at the grain boundaries and may cause leaks at the flange level after a vacuum firing cycle). The surface is enriched in Fe due to the Cr evaporation during the heat treatment. When the material is brought back to atmospheric pressure, it keeps the memory of the treatment since the hydrogen diffusion at room temperature is small: a single treatment is needed for the full life of the material.

As previously, the hydrogen outgassing rate after n successive bakeouts and vacuum firings can be computed using the 1st Fick Law, see Eq. II.8.38 [32]. The equation below gives the hydrogen outgassing rate of a vacuum fired stainless steel that is in situ baked n times,

$$q_{n,F}(t) \;=\; \left[c_F \;+\; (c_0 - c_F)\, e^{-\left(\frac{\pi}{L}\right)^2 D(T_F)\, t_F}\right] \frac{4D(T_{\mathrm{RT}})}{L}\, e^{-n\left(\frac{\pi}{L}\right)^2 D(T_{\mathrm{BO}})\, t_{\mathrm{BO}}} \quad , \tag{II.8.38}$$

with c_0 the initial hydrogen concentration (assumed to be uniform), c_F the hydrogen concentration in the material defined by the oven pressure at high temperature, T_F the furnace temperature, t_F the duration of the vacuum firing, T_{BO} the bakeout temperature and t_{BO} the duration of the bakeout.

It can be shown that for thin sheets (e.g., tubes), the initial content of the hydrogen in the material is fully removed. The final outgassing is defined by the H_2 pressure in the furnace. It equals 5×10^{-15} mbar·l/s/cm^2. For thick slab (e.g. flanges), the pressure in the furnace has limited influence and the outgassing rate is defined by the firing temperature. In this last case, the computed outgassing rate equals 10^{-13} mbar·l/s/cm^2 [12, 35].

Laboratory studies confirmed the model: the measured hydrogen outgassing rate of a 1.5 mm thick sheet after bakeout at 300°C was 5×10^{-13} mbar·l/s/cm^2 and dropped to 5×10^{-15} mbar·l/s/cm^2 following the vacuum firing process. In both cases, a reduction of 1.8 was observed between each bakeout cycle, see Table II.8.12 and Ref. [36]. The vacuum firing reduces by two orders of magnitude the hydrogen outgassing rate. Vacuum firing is routinely applied at CERN when low UHV is required.

Table II.8.12: Outgassing rate (in mbar·l /s/cm^2) of 300°C baked unfired and vacuum fired stainless steel as a function of bakeout cycles [36].

bakeout cycle	1	2	3	4	5
Baked stainless steel	5 10^{-13}	5 10^{-14}	3 10^{-14}	1.5 10^{-14}	-
Vacuum fired stainless steel	5 10^{-15}	3 10^{-15}	1.5 10^{-15}	9 10^{-16}	5 10^{-16}

Another way to decrease the hydrogen outgassing rate of baked materials is to perform an air baking to create a diffusion barrier [37]. This low cost solution was employed for the 2×3 km arms of the VIRGO gravitational wave detector at Pisa, Italy. The method consists in performing an air firing at 400°C for 38 h following by a bakeout under vacuum at 150°C for 7 days. The process increases the oxide thickness by a factor of ten in such a way that the diffusion energy increases from 0.5 to 0.6 eV. As a result, the measured outgassing rate on a 7.5 m long, 1.2 m diameter and 2 mm thick 304 L stainless steel prototype reached an outgassing rate of 10^{-15} mbar·l/s/cm^2.

Coating can be also produced on the vacuum chamber to reduce hydrogen outgassing. A 1 µm thick film of TiN deposited on the vacuum chamber can reduce the hydrogen permeation hence the

outgassing [38]. Extrapolation from coupons measurements predicts 10^{-17} mbar·l/s/cm^2. However, it is difficult to realise a uniform coating without pinholes which would compromise the observed performance on a tube or vacuum chamber. In spite of this, a reduction of two orders of magnitude on the hydrogen outgassing rate when comparing a short uncoated chamber (10^{-12} mbar.l/s/cm^2) to a TiN coated chamber (7×10^{-15} mbar.l/s/cm^2) is observed. Today, there are yet no applications of this technology for accelerators although an attempt to implement this technology was made [39].

A last, and widely used way to reduce outgassing is to dissolve hydrogen using getter materials. The technology developed at CERN, uses magnetron sputtering to produce a 1 µm thick film of TiZrV in stoichiometric proportion [40,41]. Ti, Zr and V are getter materials and have remarkable properties once activated to 180–200°C. Once activated, owing to the high solubility and diffusivity of hydrogen, the coating provides at room temperature an extremely low outgassing rate (<10^{-17} Torr·l/cm^2 that means < 300 CH_4/cm^2) and large pumping speed (0.3-2.2 l/s/cm^2 for H_2 and 5-9 l/s/cm^2 for CO). This corresponds to $\approx$ 2 000 & 15 000 l/s per metre of LHC vacuum chamber for H_2 and CO respectively! Such technique developed on the km scale allowed to reach a pressure below 10^{-11} mbar from day 1 in all the room temperature parts of the LHC vacuum system [42].

II.8.4.5 Non-metallic materials

Ceramics are used as insulators for feedthrough, as RF windows for their transparency to EM fields or to minimise Foucault's currents induced in the vacuum chambers of fast ramping magnets (kickers) or fast cycling accelerators. These types of materials are usually sintered during their production, for instance alumina (Al_2O_3) is sintered at 1 600°C. Their outgassing rate is a function of their porosity. Before their use in vacuum systems, ceramics are heated to high temperature (so called ceramic "burning") under atmosphere for outgassing. After such treatment, their specific outgassing rate can be very low, for instance the TiN coated alumina vacuum chambers produced for the J-PARC rapid-cycling synchrotron reach 1 10^{-11} mbar·l/s/cm^2 after 50 h of pumping [43]. Recent studies suggest that the ceramic burning is not required, and carbides, silica, alumina, and Titanium dioxide may be used without any specific heat treatment. Only Macor® and nitrides ceramics would require an in-situ bakeout to 200°C to reach UHV. Achieved specific outgassing rates of different ceramics lies in the range 1 10^{-12}–1 10^{-10} mbar.l/s/cm^2 after bakeout [44].

Ferrites are sometimes used in accelerator components to modify the EM properties of an RF resonator (e.g. TT2-11R, CMD5005, CMD10). After bakeout, their specific outgassing rate is low, 1 10^{-11} mbar.l/s/cm^2 is reached after a heat treatment at $400 - 1\,000$°C. Beware that those material may heat up during their operation due to EM waves damping, so called "beam-induced heating" which provokes a thermal outgassing, that scales like Eq. II.8.37, a strong function of the activation energy, E, and the temperature, T. Table II.8.13 gives the outgassing rate increase at various temperatures for typical ferrites. A too large temperature may hamper the operation of an accelerator (e.g. in the LHC, the circulating beams increase the temperature of some boron-nitride jaw by impedance effects [45]).

Additive manufacturing is a recent technique, that allows the construction of new and complex shapes. The specific outgassing rate of additive manufactured stainless steel is as low as conventional ones [46]. A first beam position monitor produced by additive manufacturing was recently installed in

Table II.8.13: Outgassing rate increase for typical ferrites with respect to room temperature set at 20°C.

50°C	100°C	150°C	200°C
5	40	150	600

THOM-X.

Polymers and elastomers are an important category of materials for vacuum technology. These materials are highly porous and contain much more water than stainless steel. Usually those materials cannot be baked although some can be to 150–200°C. Their outgassing rate, see Eq. II.8.29, is limited by a diffusion process with $a = 1/2$. Moreover, the outgassing rate of these materials is 10^2–10^5 larger than metals. Consequently, much longer time is required to evacuate the water from a vacuum vessel that is using plastics. A good vacuum design uses only metallic surfaces and reduces to (about) zero the quantity of plastics.

Exercise 11: consider a 10 m long stainless steel beam tube of 10 cm diameter sealed by two Viton® gaskets. What is the outgassing rate after 1 h and 1 week of pumping? Conclusion? (the specific rate of unbaked Viton® after 1 h equals 10^{-6} mbar.l/s/cm^2. The exposed surface to vacuum of the two seals equals 12.5 cm^2).

The thicker the plastic material, the more moisture is embedded. During pump down, first diffusion dominates ($a = 1/2$) then a dependency with $a = 3$ is observed after an extended period of pumping time ($t >$ 100 h). The specific outgassing rates, q, measured on samples of different thicknesses (0.2–1.2 mm) range from 1 10^{-10}–1 10^{-7} mbar.l/s/cm^2 after 100 h of pumping. Compared to Vespel® & Kapton®, PEEK has larger diffusion coefficient hence faster q reduction and lower moisture content hence lower q. Polymers thicker than $\sim$ 1 mm require more than two weeks of pumping to reduce q significantly. A bake-out to 200°C strongly reduce outgassing in the 10^{-11} – 10^{-10} mbar.l/s/cm2 range [47, 48]. It must be stressed that a venting with pure nitrogen or dry air is required to preserve the benefit of the material outgassing.

Finally, it must be remembered that vacuum instruments using hot filaments degas. Hence, the measurement of the pressure may be affected by the vacuum instrument cleanliness. For this reason, it is of paramount importance that the instrument is degassed, and remains ON and clean during the process, see Sections II.8.3.1 and II.8.3.2.

There is a lot of outgassing rate data available in the literature. However, quite often, the circumstances under which the data were obtained, and the detailed material properties and preparation are not well defined. Moreover, some data are sometime contradictory or misreported. When possible, it is therefore customary to repeat the measurement in your own laboratory with your own material and your own surface preparation to get a dataset useful for your study.

II.8.4.6 Qualification of materials

Outgassing of small samples can be evaluated using the accumulation method. A sample is placed in a vacuum vessel and pumped down. The vessel where the sample is located can be isolated from the pumping system by a leak valve. During this period, the gas desorbs from the sample and accumulates into the sample's chamber. By regularly opening then closing the leak valve, the gas accumulated during

a period can be identified and quantified using a QMS and a Bayard-Alpert gauge. The leak valve opening/closing procedure is repeated every 1 to 72 h yielding the desorption rate as a function of time. This method is very sensitive and it is used for measurements of low outgassing rates.

The throughput method is a standard technique used to determine a quantity of gas. Two vacuum vessels are separated by a known conductance, usually $\sim$ 10 l/s. The device under test is connected to the upstream vessel and the pumping system to the downstream vessel. The outgassing rate of the device is given by the gas flow across the conductance, see Eq. II.8.10. By measuring the total pressure upstream and downstream to the conductance, the total outgassing rate can be evaluated. A QMS allows to derive the outgassing rate for each gas species. The conductance can be computed using standard formula but also calibrated by injecting a known gas flux into the upstream vacuum vessel.

Cleaning is an important step during the construction phase of a vacuum equipment. Chemical cleaning is used to remove gross contamination such as grease, oil, fingerprints. It can be needed to attack the surface with acids to etch the oxide layer. Passivation is essential to produce a "stable" oxide layer on the surface. Several cleaning techniques are developed as a function of the material used and their final application. As an example, the 16 m long CERN LHC beam screens were degreased with an alkaline detergent at 50°C in an ultrasonic bath, rinsed with running tap water, rinsed by immersion in cold demineralized water, rinsed with alcohol, and dried at ambient air. An important step is to analyze the surface to evaluate the cleanliness of a material, identify species, monitor a process, etc. Techniques such as Auger Electron Spectroscopy (AES), Secondary Ion Mass Spectroscopy (SIMS) or X-ray Photon Electron Spectroscopy (XPS) are used [28, 49, 50].

Once the vacuum equipment has been properly designed, cleaned, and assembled using appropriate techniques to maintain the cleanliness (e.g. gloves, laminar flow, etc.), the device shall be qualified before installation in the accelerator. For the operation of large machines, several test benches based on the throughput method, are used to measure the ultimate pressure, perform a gas analysis, and evaluate the outgassing rate. Outgassing rate obtained after bakeout of standard accelerators equipment lies in the range 10^{-9} to 5 10^{-8} mbar·l/s [51].

II.8.5 Cryo-vacuum

With the increasing use of cryogens in accelerator technology for RF (e.g. superconducting cavities) and magnetic devices (e.g. superconducting magnets), the knowledge of vacuum at cryogenic temperature (cryo-vacuum) is becoming a must. Therefore, elements of cryo-vacuum shall be part of a modern lecture on vacuum science and technology [10–12, 52].

II.8.5.1 Elements of cryopumping

We have seen above in Eqs.II.8.26 and II.8.28 that the probability of desorption and the sojourn time of a molecule on a surface is an exponential function of the binding energy and the surface temperature. For temperatures below 100 K, cryosorption occurs and molecules are weakly bound to a surface (physisorbed) and remain adsorbed for very long periods. Taking one year as a reference sojourn time for a cryopump, physisorption can occur for binding energy below 20 meV at liquid helium temperature (4.2 K) and below 300 meV at liquid nitrogen temperature (77 K). Of course, the energies of physisorp-

tion depend on the nature of the gas and the properties of the surface. For instance, a natural warm up from liquid helium temperature to room temperature of a stainless-steel evacuated vessel by a pump, exhibits desorption peaks. H_2 desorbs at $\sim$ 18 K, CO at 45 K, CH_4 and 60 K, CO_2 and 95 K and $H_2O >$ 250 K.

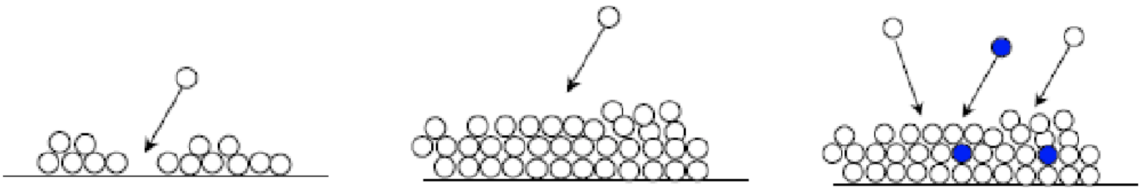

Fig. II.8.6: Schematic illustration of the different mechanisms of cryopumping: (left) physical adsorption, (middle) condensation, (right) cryotrapping.

As shown in Fig.II.8.6, three mechanisms for cryopumping are distinguished: 1) physical adsorption, 2) condensation and 3) cryotrapping. Physical adsorption concerns sub-monolayer coverage. It is due to attractive forces, of van der Waals type, between a molecule and a surface. Binding energies for H_2 physical adsorption range from 20 to 85 meV for smooth and porous material. Hence, smooth surface desorbs gas at lower temperature than porous surface e.g. 1 h sojourn time is at 5.2 K for a smooth surface and 26 K for a porous surface. Consequently, sub monolayers quantities of gas can be physisorbed at their boiling temperature. Condensation happens for thick gas coverage where only the force between molecules takes place. By condensation, the gas liquifies or solidifies. Typical energies of vaporisation are 9 meV for H_2 and 175 meV for CO_2. As said above, the desorption of thick layers of ice is governed by 0^{th} order desorption ($n = 0$), see Eq. II.8.26. The cryotrapping mechanism makes use of a condensable carrier (e.g. Ar) to trap molecules with high vapour pressure (e.g. He, H_2).

The pumping speed of a cryopump is characterised by the sticking probability, σ, the ratio of the cryosorbed molecules to the incident rate, see Eq. II.8.3. Values of sticking probability are very scarce in the literature; this is why it is quite often assumed a unitary sticking probability, i.e. all molecules incident on a cold surface are immediately pumped after the first interaction. But the sticking probability is a function of the gas species, the surface condition, the surface coverage, the surface and gas temperatures. For instance, sticking probabilities of hydrogen at 300 K incident on a surface held at 3.1 K increases from 0.3 at 10^{14} H_2/cm^2 to 0.9 at 10^{17} H_2/cm^2. At large coverage, the hydrogen condensation coefficient on a surface held in the 3.5–3.9 K, decreases from 1 to 0.7 while increasing the kinetic energy (temperature increases from 100 to 700 K) of the molecule [53, 54].

If the sticking probability of a molecule on a cold surface (or cryopumping surface) is known, the pumping speed S of the cryopump can be computed using Eq. II.8.39 (to provide pumping, a cryopump shall be used in the regime $P << P_{\text{sat}}$, where P_{sat} is the saturated vapour pressure),

$$S = \frac{1}{4}\sigma \left(1 - \frac{P}{P_{\text{sat}}}\right) A\, v \cong \frac{1}{4}\sigma\, A\, v \quad , \tag{II.8.39}$$

with the sticking probability σ, the geometrical area of the cold surface A, and v the average thermal

speed of the molecule, see Eq. II.8.1. The ideal pumping speed is the maximum pumping speed obtained when $\sigma = 1$.

Exercise 12: demonstrate that the ideal pumping speed is the one of the conductance of a hole.

The engineering formula per unit of surface is given by Eq. II.8.40, where M is the molar mass in g,

$$S[\mathrm{l\,s^{-1}cm^{-2}}] \;=\; 3.63\sigma\sqrt{\frac{T[K]}{M[g]}} \quad . \tag{II.8.40}$$

Exercise 13: a cryopump operating at 10 K has a surface of 10 cm^2. What is the ideal pumping speed for hydrogen and CO? A 5 cm diameter, 1 m long vacuum chamber operates at 15 K. What is the ideal pumping speed for hydrogen and CO?

For cryogenic reasons, the cold surface is protected from thermal radiations. This is the case of cryopumps that are protected by baffles and radiations. This is also the case in LHC for instance where the cold bore is protected from synchrotron radiation heat load by a so-called beam screen. The effective pumping is then reduced by the geometry of the system. The sticking probability of Eq II.8.40 is then substituted by the capture factor, C_f. Cryopumps have a capture factor of ~ 0.3 [55] and the perforation of the LHC beam screen a capture factor of ~ 0.5 [56].

In cryogenic vacuum systems, the gauges are usually placed at room temperature and connected to the vessel held at cryogenic temperature by a transition tube. Doing so, the heat load on the cryogenic system is minimised but the pressure is not directly measured (remember, the pressure depends on temperature, Eq. II.8.6). By equating the impingement rate at the cold to warm transition, we obtain Eq. II.8.41 that link the pressure, P, and gas density, n, between vacuum vessels 1 and 2 held at temperature T_1 and T_2,

$$\frac{P_1}{P_2} = \sqrt{\frac{T_1}{T_2}} \quad \text{and} \quad \frac{n_1}{n_2} = \sqrt{\frac{T_2}{T_1}} \quad . \tag{II.8.41}$$

In practice, when a pressure is measured at room temperature, the corresponding pressure at liquid nitrogen temperature (77 K) is obtained by dividing the room temperature pressure by 2 and by 8 at liquid helium temperature (4.2 K).

In accelerator physics, what matters is the beam interaction with the residual gas molecules. The relation of the gas density, n, in the beam pipe held at T K, to the pressure measured at room temperature, P_{300}, is given by Eq. II.8.42,

$$P_{300} = n\,k\,T\sqrt{\frac{300}{T}} \quad . \tag{II.8.42}$$

Exercise 14: the LHC design gas density is set at 10^{15} H_2/m^3. In 2018, gas density estimated by the beam loss monitors equals 2.5×10^{12} H_2/m^3. What is the corresponding pressure at room temperature? Assume the LHC beam screen tube operates at 15 K.

II.8.5.2 Adsorption isotherms

Adsorption isotherms are the equilibrium pressure of a gas for a given surface coverage, θ, at a defined temperature, T. Adsorption isotherms vary with many parameters such as the molecular species, the surface temperature (under 20 K, only H_2 and He are present), the nature of the surface, the gas composition in the vacuum chambers, etc. When required, characterisation of your material for your specific process is a must.

There a several models of adsorption isotherms. One may cite the Henry's law, valid for low surface coverage, as shown in Eq. II.8.43,

$$\theta = cP \quad , \tag{II.8.43}$$

where c is a constant.

The DRK model (Dubinin, Radushkevich and Kaganer) is used for metallic, glass and porous substrates. It is valid at low pressure and gives good predictions with temperature variation,

$$\ln(\theta) \; = \; \ln(\theta_m) \; - \; D \left[k\,T \ln\left(\frac{P_{\text{sat}}}{P}\right)\right]^2 \quad , \tag{II.8.44}$$

with θ_m the DRK surface coverage at one monolayer, D a constant in eV^{-2}.

The BET model (Brunauer, Emmet and Teller) is shown in Eq. II.8.45 with $\alpha = e^{\frac{\Delta E}{kT}} >> 1$. The model is a multi-monolayer description valid in the range $0.01 < \frac{P}{P_{\text{sat}}} < 0.3$. It can be used to derive the roughness factor of a technical surface by plotting an adsorption isotherm in the BET coordinates $P/P_{\text{sat}}, P/\left[\theta(P_{\text{sat}} - P)\right]$,

$$\frac{P}{\theta(P_{\text{sat}} - P)} \; = \; \frac{1}{\alpha\,\theta_m} + \frac{(\alpha - 1)}{\alpha\,\theta_m}\frac{P}{P_{\text{sat}}} \cong \frac{1}{\theta_m} + \frac{P}{P_{\text{sat}}} \quad . \tag{II.8.45}$$

The saturated vapour pressure of a gas is the pressure P_{sat} of this gas over its liquid or solid phase, i.e. when many monolayers of gas are condensed on a surface. The saturated vapour pressure follows the Clausius-Clapeyron law,

$$\log(P_{\text{sat}}) \; = A \; + \; \frac{B}{T} \quad , \tag{II.8.46}$$

where A and B are constant given in Table II.8.14.

Table II.8.14: A and B constants (see Eq. II.8.46) for P_{sat} expressed in mbar at 300 K.

	He	**H_2**	**CH_4**	**H_2O**	**Ne**	**N_2**	**CO**	**C_2H_6**	**O_2**	**Ar**	**CO_2**
A	4.09	3.97	7.36	10.23	6.95	8.14	8.67	9.69	8.57	7.84	9.995
B	4.96	40.9	486.8	2612.6	109.87	379.27	441.19	1039.34	463.448	420.58	1360.35

Figure II.8.7 shows the saturated vapour pressure curve as function of the surface temperature for common gas species [12]. Data were measured at high pressure on smooth surfaces (Cu, glass) and extrapolated in the XHV-UHV range. The indicated pressure is corrected from thermal transpiration.

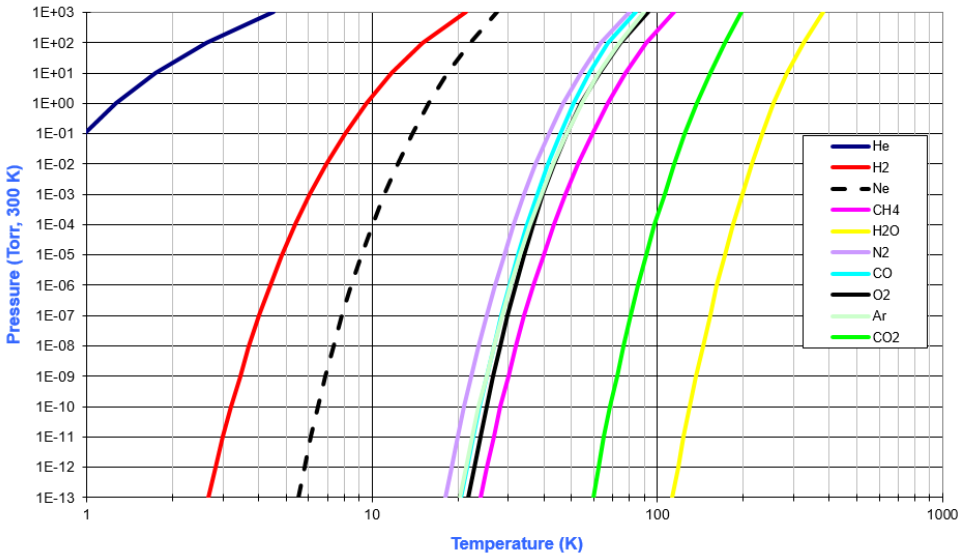

Fig. II.8.7: Saturated vapour pressure curve as a function of temperature [12].

At atmospheric pressure (760 Torr), liquid helium boils at 4.2 K, hydrogen at 20 K, nitrogen at 77 K and water at 373 K. When decreasing the temperature, the saturated vapour pressure is also decreased: several orders of magnitude over a few Kelvins.

Below 20 K, the saturated pressure of common gases in vacuum systems (excepting He, H_2) is below 10^{-13} Torr. Therefore, large quantities of such gases can be pumped below 20 K. At liquid helium temperature (4.2 K) only helium and hydrogen are not pumped (Ne is barely present in usual vacuum systems). Therefore, only He and hydrogen matter at cryogenic temperature. At 4.2 K, the saturated vapour pressure of hydrogen is $\sim 10^{-6}$ Torr. In the operating range of the LHC beam screens (5 to 20 K), the saturated vapour pressure of hydrogen spans over eight decades.

When reducing the quantity of adsorbed gas on the cold surface, the vapour pressure is also reduced because the cryopumping regime evolves from condensation to physisorption.

Figure II.8.8 shows the hydrogen adsorption isotherm onto stainless steel in the 2.3–4.17 K range [57]. As more gas is adsorbed on the cold surface, the vapour pressure increases reaching a plateau, the so-called saturated vapour pressure. The steep rise is obtained at about one monolayer 3 10^{15} H_2/cm^2. The vapour pressure saturates when several monolayers of gas are adsorbed. At 4.17 K, the saturated vapour pressure of hydrogen equals 7×10^{-7} Torr (9 10^{-7} mbar) which translates into 6×10^{-6} Torr (8×10^{-6} mbar) when thermal transpiration corrections at 300 K are applied. The pressure level of the saturation is a function of the temperature.

When reducing the operating temperature of the cold surface from 4.17 to 2.3 K (the operating temperature of a condensation cryopump [58]) the saturated vapour pressure vanishes to 3 10^{-11} mbar. However, an "anomalous" deviation from the Clausius Clapeyron law can be observed due to thermal radiation at 300 K on the cryo-surface. At 2.3 K, a linear dependence of the saturated vapour pressure (from 10^{-11} to 10^{-9} Torr) is observed with the absorbed power on the surface, function of its emissivity and the quantity of impinging radiation. Silver plating of the cold surface and an optimised screening of

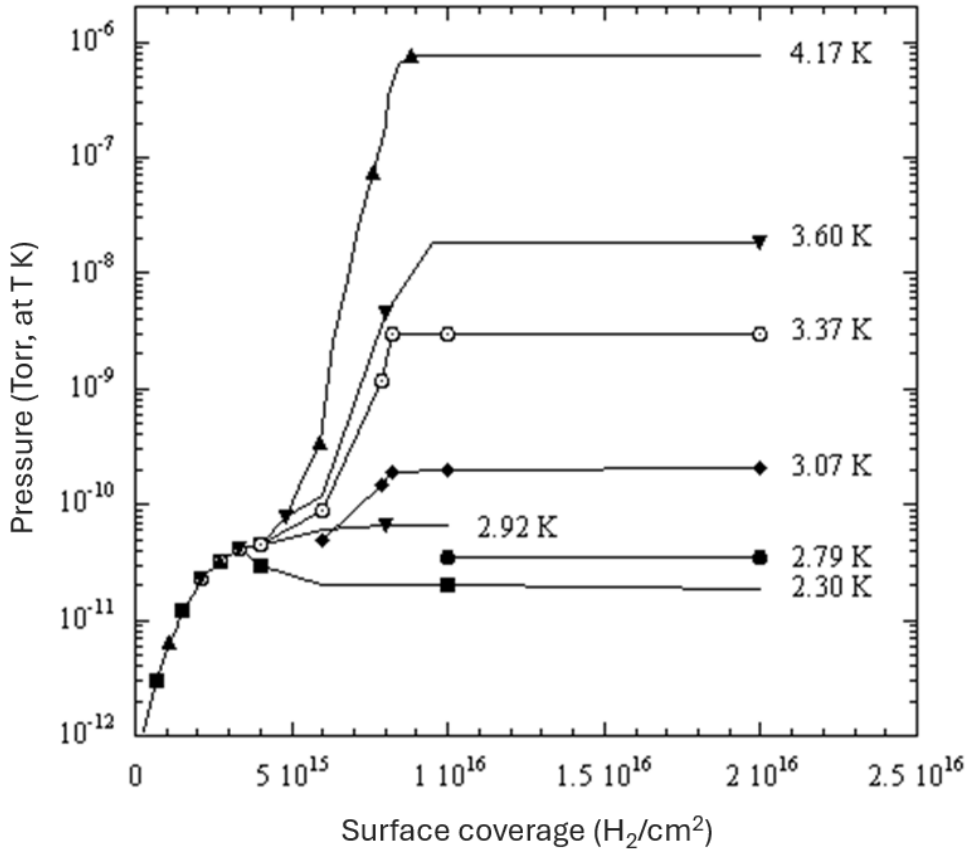

Fig. II.8.8: Hydrogen adsorption isotherm onto a stainless-steel surface as a function of the temperature [57].

the 300 K thermal radiation towards the cold surface can be used to overcome the problem.

Hydrogen adsorption isotherms on stainless steel were obtained in the 7—18 K range and fitted with the DRK model using the following parameters: $D = 3075$ eV^{-2} and $\theta_m = 6.4510^{14}\mathrm{H_2/cm^2}$ [59]. At constant surface coverage, when increasing the temperature, the hydrogen vapour pressure strongly increases by several orders of magnitude. At 10^{-9} mbar, the relative surface coverage (the ratio of the surface coverage to the monolayer coverage) decreases from 40% at 8 K to 0.2% at 18 K.

In accelerators, several species of molecules are present, therefore the study of gas mixtures in real machine environment is important. Indeed, the adsorption isotherm shown in Fig.II.8.8 can be strongly distorted by the presence of CH_4, CO and CO_2. Adsorption on gas condensates modifies the adsorption capacity and co-adsorption with gases other than hydrogen reduces the vapour pressure by cryotrapping. For instance, 2×10^{16} CO_2/cm^2 pre-condensed on the surface, the hydrogen steep rise is shifted to 6×10^{15} H_2/cm^2. Also, for a given gas composition in the LHC, the hydrogen vapour pressure of Fig.II.8.8 is modified by co-adsorption yielding a less steep hydrogen vapour pressure rise and reducing by two orders of magnitude the hydrogen vapour pressure at 4×10^{15} H_2/cm^2 [60].

Hydrogen isotherm of technical surfaces can be split into two categories: 1) smooth surfaces such as Cu, stainless steel, glass [61] with low adsorption energies and 2) porous surfaces of adsorbents such as anodised aluminium with high adsorption energies at pores and defects [52]. A particularly suitable

material used in cryopumps is activated charcoal. This cryosorbing material has a large pumping speed, a large capacity (10^{22} H_2/g) and a large temperature working range up to 30 K. For this reason, activated charcoal is placed on the 20 K cryopanels of the cryopumps to provide generous helium and hydrogen pumping [62].

The surface binding energy of the cryosorbed gas is evaluated by TPD, see Section II.8.4.1. For example, hydrogen adsorption at cryogenic temperature on 400 nm thick amorphous carbon coating (a technical surface with a unitary secondary electron yield) reveals the porous nature of the surface. Hydrogen is adsorbed until 40 K at the high energy sites in quantity of 3 10^{15} H_2/cm^2. When increasing the surface coverage, hydrogen desorbs at lower temperature with 1.3 10^{18} H_2/cm^2 desorbed at 8 K. The monolayer capacity of this material is estimated to be in the range 1–5 10^{17} H_2/cm^2 [52].

Another example, with hydrogen adsorption on amorphous water ice, reveals a wide range of adsorption sites that, here also, varies with the surface coverage where high energy sites are first occupied at low surface coverage then low energy sites are occupied at large surface coverage. The amorphous water ice is characterized by a distribution of adsorption sites that are filled according to a Fermi–Dirac statistical law [62].

II.8.6 Interactions with circulating beams

In modern and next generation accelerators, the machine parameters have a strong impact on the design and the performance of the vacuum system. The base pressure (or "static" pressure) obtained in the beam pipe after the commissioning is modified by the circulation of the beam. This pressure increase is named "dynamic" pressure because it stops when the beam is aborted. Synchrotron radiation emitted in the magnetic fields stimulates molecular desorption, ion bombardment of the vacuum chamber walls may cause pressure runaway and electron cloud also provokes pressure increases. In this section, we will discuss these main phenomena at the origin of the dynamic pressure [10–12, 52].

II.8.6.1 Fundamentals of synchrotron radiation

When a charged particle is accelerated it can generate EM radiation. The centripetal acceleration generates more power than the longitudinal acceleration by a factor γ^2 (with $\gamma = E/E_0$, the relativistic factor). For a relativistic particle, the EM radiation is highly peaked, with an opening $1/2$ angle of $1/\gamma$. Synchrotron radiation is emitted tangentially to the beam orbit of circular accelerators [52, 63–65] (see also Chapter I.10 on synchrotron radiation). Depending on the bending radius and the mass of the particle, the radiation energy ranges from infrared (meV) to gamma rays (MeV). The emitted radiation along the beam orbit forms a horizontal fan with high-energy photons in the centre and low-energy photons below and above the horizontal plane. In synchrotrons, the energy loss shall be compensated by the RF system to keep the particles on their orbit. Synchrotron radiation is especially strong for electrons and positrons moving in magnetic fields. Synchrotron radiation centres around the world operate with electrons, e.g. SOLEIL operates with electrons of 2.75 GeV.

The synchrotron radiation is characterised by the critical energy, ε_c, which splits into two equal parts the power spectrum, see Eq. II.8.47 (88% of the emitted photons have an energy lower than the critical energy),

$$\varepsilon_c = \frac{3}{2}\frac{hc}{2\pi}\frac{\gamma^3}{\rho} \quad , \tag{II.8.47}$$

with $h = 6.62 \times 10^{-34}$ J.s the Plank constant, $c = 3 \times 10^8$ m/s the speed of light, ρ the bending radius in m and γ the relativistic factor. The critical energy scales like E^3. Engineering formulae for electrons and protons are given by Eq. II.8.48,

$$\begin{aligned} \text{Electrons}: \quad \varepsilon_c &= 2.218 \times 10^3 \frac{E[\text{GeV}]^3}{\rho[\text{m}]} \\ \text{Protons}: \quad \varepsilon_c &= 3.5835 \times 10^{-7} \frac{E[\text{GeV}]^3}{\rho[\text{m}]} \end{aligned} \quad . \tag{II.8.48}$$

The bending radius can be derived from the magnetic rigidity,

$$B\,\rho = \frac{p}{q} \cong \frac{E}{ec} \quad , \tag{II.8.49}$$

with B the magnetic field, p the particle momentum, $e = 1.602 \times 10^{-19}$ C the elementary charge and E the particle energy ($E >> E_0$). The engineering formula is then

$$\frac{1}{\rho} \cong \frac{3}{10}\frac{B[\text{T}]}{E[\text{GeV}]} \quad . \tag{II.8.50}$$

Consequently, the critical energy scales like BE^2, as shown by Eq II.8.51,

$$\epsilon_c = \frac{3}{2}\frac{hc^2}{2\pi}\frac{e}{{E_0}^3}BE^2 \quad . \tag{II.8.51}$$

The average power, P_0 emitted by synchrotron radiation per unit of length is

$$P_0 = \frac{e\gamma^4}{6\pi\varepsilon_0\rho^2}I \quad , \tag{II.8.52}$$

with $\varepsilon_0 = 8.85 \times 10^{-12}$ F/m the vacuum permittivity and I the beam intensity in A. The average power emitted per unit of length scales like B^2E^2I as shown by Eq II.8.53,

$$P_0 = \frac{e^3c^2}{6\pi\varepsilon_0}\frac{1}{E_0^4}B^2E^2I \quad . \tag{II.8.53}$$

Engineering formulae for electrons and protons are given by Eq. II.8.54,

$$\begin{aligned} \text{Electrons}: \quad P_0[\text{W/m}] &= 88.57 \quad \frac{E[\text{GeV}]^4}{2\pi\,\rho[\text{m}]^2} I[\text{mA}] \\ \text{Protons}: \quad P_0[\text{W/m}] &= 7.79 \times 10^{-12} \quad \frac{E[\text{GeV}]^4}{2\pi\,\rho[\text{m}]^2} I[\text{mA}] \end{aligned} \quad . \tag{II.8.54}$$

For the total dipole radiation power dissipated around the ring, multiply Eq. II.8.52 (or Eq. II.8.54) by $2\pi\rho$.

Protons generate a lot less synchrotron radiation compared to electrons because there is a m^{-4} dependency in the formula for the radiated power, where m is the mass of the radiating particle. Protons

are 1 836 times heavier than electrons, so the reduction factor is $\sim 8.8 \times 10^{-14}$.

The synchrotron radiation power emitted by a particle is a function of the vertical angle (above/below the plane of the orbit) and the wavelength. It can be shown that by integrating over the vertical angle, one obtains the spectral power density per unit of length that is proportional to the average emitted power divided by the critical energy and a universal function. Remarking that this spectral power density is equal to the photon flux per unit length in a relative energy band, one can compute the total photon flux per unit of length, $\dot{\Gamma}$, given by Eq. II.8.55,

$$\dot{\Gamma} = \frac{15\sqrt{3}}{8}\frac{P_0}{\varepsilon_c} = \frac{5\sqrt{3}\,e}{12\,h\,\varepsilon_0\,c}\frac{\gamma}{\rho}\,I \quad . \tag{II.8.55}$$

The photon flux per unit of length scales like BI as shown by Eq. II.8.56,

$$\dot{\Gamma} = \frac{5\sqrt{3}\,e^2}{12\,h\,\varepsilon_0}\frac{1}{E_0}\,BI \quad . \tag{II.8.56}$$

Engineering formulae for electrons and protons are given by Eq. II.8.57,

$$\begin{aligned} \text{Electrons}: \quad \dot{\Gamma} &= 1.288 \times 10^{17}\,\frac{E[\text{GeV}]}{\rho[\text{m}]}\,I[\text{mA}] \\ \text{Protons}: \quad \dot{\Gamma} &= 7.017 \times 10^{13}\,\frac{E[\text{GeV}]}{\rho[\text{m}]}\,I[\text{mA}] \end{aligned} \quad . \tag{II.8.57}$$

The synchrotron radiation light is highly peaked, with a vertical opening $\frac{1}{2}$ angle of $\frac{1}{\gamma}$. Low-energy photons are emitted at large vertical angle and high-energy photons at low vertical angle. Equation II.8.58 gives the maximum vertical angles for photons with energies $\varepsilon \ll \varepsilon_c$ and vertical angles for photons with energies $\varepsilon \gg \varepsilon_c$,

$$\begin{aligned} \varepsilon \ll \varepsilon_c: \quad \theta_{\max} &= \frac{2}{\gamma}\left(\frac{\varepsilon_c}{\varepsilon}\right)^{1/3} = \frac{1.33\times10^{-2}}{(\varepsilon[\text{eV}]\,\rho[\text{m}])^{1/3}} \\ \varepsilon \gg \varepsilon_c: \quad \theta_{\max} &= \frac{2}{\gamma}\left(\frac{3\varepsilon_c}{\varepsilon}\right)^{1/2} = \frac{2.30\times10^{-2}}{(\varepsilon[\text{eV}]\,\rho[\text{m}])^{1/2}} \end{aligned} \quad . \tag{II.8.58}$$

Table II.8.15 compares two synchrotron radiation sources parameters with the CERN Large Electron Positron Collider (LEP). In synchrotron radiation sources, the emitted synchrotron radiation power and photon flux are extremely large. Note also the highly focused radiation that correspond for the ESRF case to a spot size of 0.82 mm ten metres aways from the beam. Note for LEP the extremely high critical energy.

Table II.8.15: Parameters of some synchrotron radiation sources.

	E [GeV]	**I [mA]**	**ρ [m]**	**ϵ_c [keV]**	**[ph/m/s]**	**P [kW/m]**	**1/γ [µrad]**
ESRF-1	6	200	23.37	20.5	6.6 10^{18}	6.7	82.5
ELETTRA	2	250	5.5	3.2	1.2 10^{19}	3.7	255.5
LEP	100	4	2963	748.6	1.7 10^{16}	0.6	5.1

Figure II.8.9 shows the synchrotron radiation spectrum of the LHC for different operating energies. At injection energy, the spectrum is dominated by photons in the infrared range. At collision energy, the synchrotron radiation spectrum is widened to ultra-violet photon energy. The LHC is the first proton

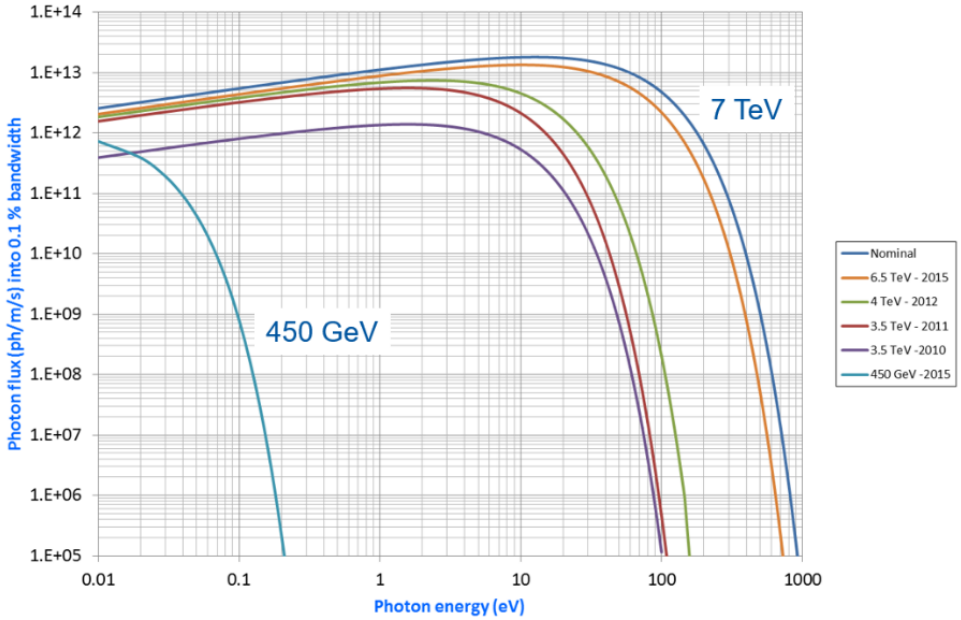

Fig. II.8.9: Synchrotron radiation spectrum of LHC for different beam energies.

synchrotron where significant synchrotron radiation is emitted. At 7 TeV, the critical energy equals only 44 eV but 10^{17} ph/m/s with 0.2 W/m are emitted inside the superconducting magnets held at 1.9 K along the 27 km ring. Note a moderate photon beam size of 1.3 mm at 10 m from the source.

Synchrotron radiation has huge impacts on the design and operation of accelerators. These are illustrated by the machine parameters of Table II.8.16. In LEP, and all synchrotron light sources, the evacuation of the power is an issue. The LHC operates at 7 TeV with $\sim$ 0.6 A. Power evacuation is an issue for the cryogenic system (1 kW/arc), due to the low Carnot efficiency at low temperature. The critical energy varies from a few tens eV to 660 keV. Strongly bound molecules can be desorbed. The photon flux is large, leading to large gas load. Adequate dimensioning of the effective pumping speed is required. The annual integrated photon dose is large which has implications on gas reduction and radiation.

Table II.8.16: Synchrotron radiation parameters of SOLEIL, KEK-B, LEP and LHC.

	SOLEIL	**KEK-B LER**	**KEK-B LER**	**LEP Inj.**	**LEP 1**	**LEP 2**	**LHC Inj.**	**LHC**
Particle	e^-	e^+	e^-	e^-			p	
I [mA]	500	2 600	1 100	3	3	7	584	584
E [GeV]	2.75	3.5	8	20	50	96	450	7 000
ρ [m]	5.36	16.31	104.46	2 962.96			2,784.302	
P [W/m]	14 030	20 675	5 820	0.8	30	955	0	0.2
ε_c [eV]	8 600	5 800	11 000	6 000	94 000	660 000	0	44
$\dot{\Gamma}$ [ph/m/s]	$3\ 10^{19}$	$7\ 10^{19}$	$1\ 10^{19}$	$3\ 10^{15}$	$7\ 10^{15}$	$3\ 10^{16}$	$7\ 10^{15}$	$1\ 10^{17}$
Dose at 3000h [ph/m]	$4\ 10^{26}$	$8\ 10^{26}$	$1\ 10^{26}$	$3\ 10^{22}$	$7\ 10^{22}$	$3\ 10^{23}$	$7\ 10^{22}$	$1\ 10^{24}$

Materials can melt, or air leak open due to the thermal load induced by synchrotron radiation. Hence, the vacuum system of leptons machines shall be specifically designed to cope with synchrotron

radiation. Complex vacuum chamber design exists with an antechamber that allows the light extraction, pumping, instrumentation ports and the insertion of power absorbers (so-called crotches). For instance, the SOLEIL crotch absorber is a water cooled copper (Glidcop alloy[1]) that allows to extract 256 W/mm^2. A sawtooth profile is machined along the absorber to distribute the synchrotron radiation power on a wider area. Subsequently the antechamber has integrated a distributed pumping system based on NEG strip, e.g. LEP and NSLS-2 designs. After activation by Joule effect, such NEG strip provides very large pumping speed with sticking coefficient of 0.05 for H_2 and 0.1 for CO, CO_2, N_2. An ultimate design is a NEG thin film coating in the beam tube, e.g. LHC 80 mm diameter long straight sections Cu chambers and MAX-IV 22 mm diameter Cu chambers. In superconducting hadron machines such as LHC, the extraction of the dissipated power at cryogenic temperature is the *raison d'être* of the beam screen operating at 5 to 20 K and designed to extract 4 kW per ring over the full circumference.

II.8.6.2 Photon induced molecular desorption

The interaction of photons with the vacuum chamber walls stimulates the desorption of neutral molecules inside the vacuum system. The mechanism of photon stimulated desorption (PSD) of physisorbed (meV) or chemisorbed (eV) molecules can be direct or indirect. The identified transmitters are photoelectrons, secondary electrons, and phonons. The desorption process has been attributed to a two-step process: 1) photons produces photoelectrons and secondary electrons, 2) then these electrons excite strongly bound molecules that desorbs spontaneously. Emitted photoelectrons contribute also to the gas load. The oxide and carbon layers of the near surface ($\sim$ 1-5 nm) are believed to be the source of gas. But the diffusion of atoms into the solid and their recombination at the surface play also a role.

The photon stimulated molecular desorption is a function of the nature of the material, its temperature, its surface state, a function of the photon energy and of the irradiation angle. However, no comprehensive model exists, and therefore an in-situ qualification of the materials is required for the design of a future machine.

Under photon irradiation, a dynamic pressure arises that decreases with photon dose under 'beam cleaning' or 'beam scrubbing' effects. A decrease of 3-4 orders of magnitude of the dynamic pressure (mbar/A) is routinely observed in all machines, see e.g. Refs. [66–68].

The molecular photo-desorption yield is characterised by η_{photon}, the number of molecules desorbed per incident photon. Note that this yield is given per incident photon, and not per interacting photon, and for all photon energies of the synchrotron radiation spectrum.

The pressure in a vacuum chamber subjected to synchrotron radiation irradiation is given by Eq. II.8.59 (most of the time, the dynamic pressure is larger than the static pressure),

$$P = P_{\mathrm{static}} + P_{\mathrm{dynamic}} = \frac{Q + \frac{\eta_{\mathrm{photon}}\dot{\Gamma}}{G}}{S} \cong \frac{\eta_{\mathrm{photon}}\dot{\Gamma}}{G\,S} \quad , \tag{II.8.59}$$

with the conversion factor $G = 2.4 \times 10^{19}$ molecules/(mbar.l) at room temperature.

Figure II.8.10 shows a schematic of an experimental system to measure the molecular photodes-

[1]Glidcop is a family of copper-based metal matrix composite alloys mixed primarily with small amounts of aluminum oxide ceramic particles. It is a trademark of North American Höganäs.

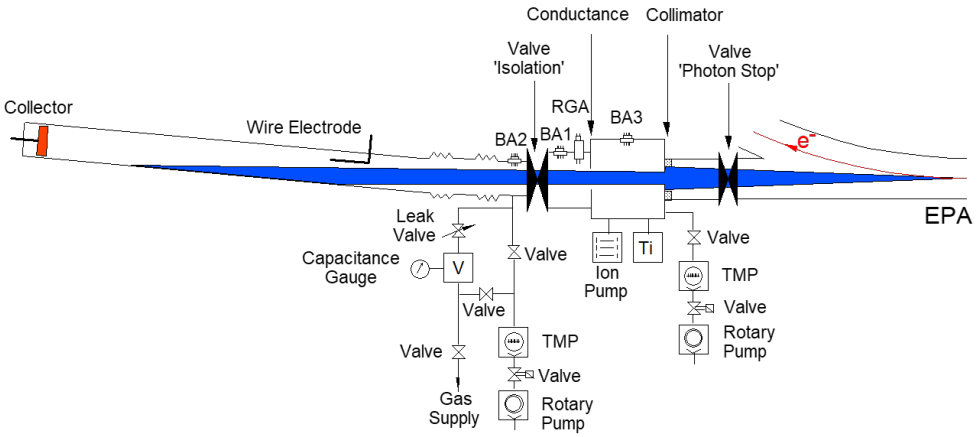

Fig. II.8.10: Experimental system to measure the molecular photodesorption yield, photon reflectivity and photoelectron yield [69, 70].

orption yield and photoelectron yield. The light emitted by a bending magnet is horizontally and vertically collimated (hence photons with energy < 4 eV are attenuated) and impinge a 4.2 m long test tube with a grazing angle of 11 mrad. The molecular photodesorption yield is measured by the gas throughput method using a conductance of 72.5 l/s for N_2 [69]. A wire and a collector are used to measure a current to estimate the photon reflectivity and the photoelectron yield [70].

Typical molecular photodesorption yields range from 10^{-3} to 10^{-6} molecules/photon when conditioned. The cleaning rate with the photon dose, D, is described by Eq. II.8.60,

$$\eta_{\text{photon}} = \eta_0 \left(\frac{D}{D_0} \right)^{-a} \quad , \tag{II.8.60}$$

with a varying from 0.5 to 1. The molecular photodesorption yield is constant at η_0 up to a photon dose D_0 and then decreases.

Figure II.8.11 shows the molecular photodesorption yield of a 3.6 m long, 129 mm inner diameter unbaked stainless steel subjected to synchrotron radiation irradiation with 3.75 keV critical energy at 11 mrad incidence angle. All gases are desorbed. The initial yield starts at 10^{-2} molecule/photon and decreases by 2–6 orders of magnitude with photon dose accumulation. The exponent a equals 1 for H_2, CO and 1.2 for CO_2, CH_4. After beam conditioning, the most dominant desorbed species are, in order of importance, H_2, CO and CO_2 [29].

By integration of the molecular desorption yield against the photon dose, the number of desorbed molecules per square centimetre of surface area can be computed. Table II.8.17 shows a total of 14.4×10^{15} molecules/cm^2 desorbed after a dose of 2×10^{23} photon/m. Hydrogen is the main species photodesorbed followed by CO and CO_2 in similar quantities.

Table II.8.17: Number of photodesorbed molecules per square centimetre [29].

	H2	**CH4**	**H2O**	**CO**	**CO2**	**Total**
Molecules/cm^2 $\times 10^{15}$	8.1	0.2	1.1	2.8	2.2	14.4

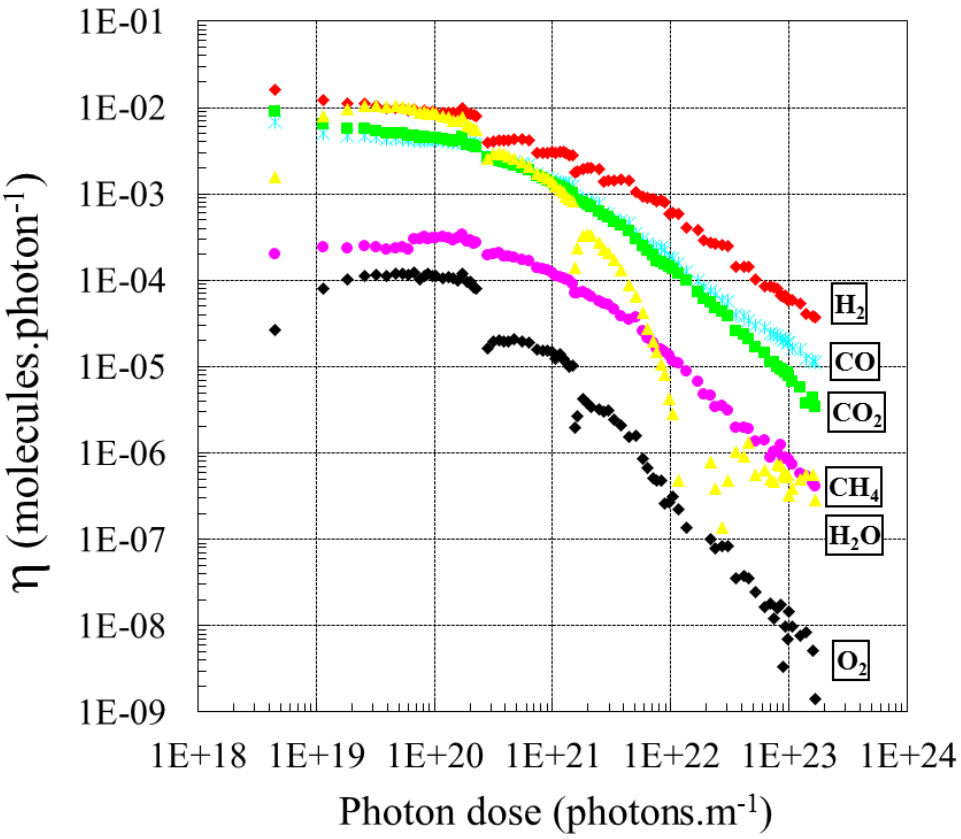

Fig. II.8.11: Molecular photodesorption yield of unbaked stainless steel when irradiated at 11 mrad with synchrotron radiation of 3.75 keV critical energy [29].

The molecular photodesorption yield is also a strong function of the critical energy. At low energy, the photoelectric effect dominates, hence a linear trend is seen until $\sim$ 5 keV. Above a few 100 keV, Compton diffusion dominates and produces a cascade of energetic recoil electrons with a diffusion of secondary photons, see Fig.II.8.12.

In the photoelectric effect region, the molecular photodesorption yield as a function of the critical energy is given by Eq. II.8.61,

$$\eta_{\text{photon}} = C\,\varepsilon_c^{\alpha} \quad , \tag{II.8.61}$$

where C and α are empirical fitting constants given in Table II.8.18 for some technical materials in the critical energy range 10–300 eV (except for H_2 stainless steel 60–300 eV), see Refs. [69, 71].

As shown from the above table, the molecular photodesorption yield is a function of the nature of the surface and its treatment. Yields of unbaked materials are larger than yields of in-situ baked materials. Other treatments such as pre-bakeout, vacuum firing or glow discharge affect also the molecular photodesorption yields, but to a lesser extent [71, 72].

When activated, a $\sim$ 1 µm thick TiZrV NEG thin film has a cleaned surface, free of carbon and oxides, to provide a large pumping speed, see Section II.8.4.4. Naturally, the intrisinsic molecular

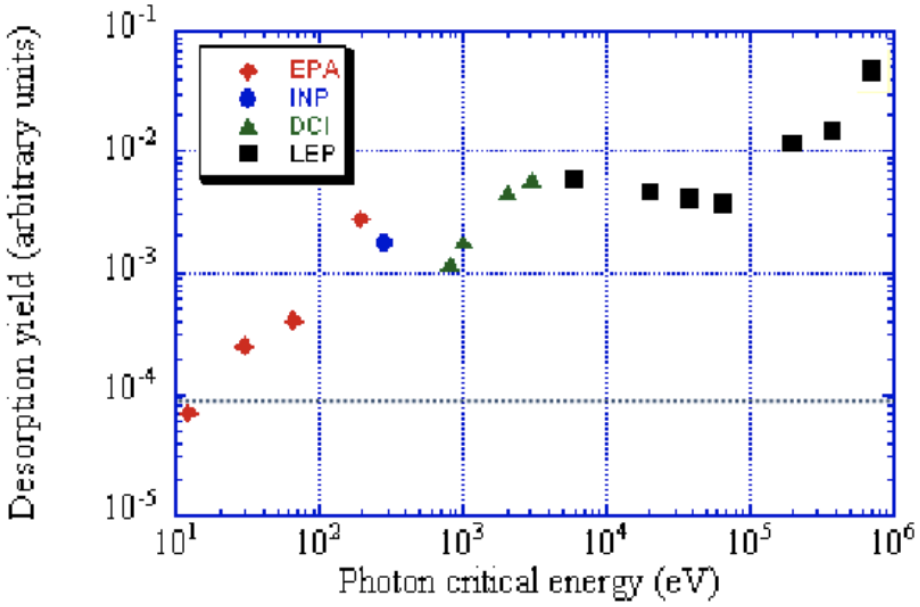

Fig. II.8.12: Relative desorption yield as a function of critical energy [10].

Table II.8.18: Empirical fitting constants for molecular photodesorption yield as a function of the critical energy, see Eq. II.8.61 (C and α are empirical fitting constants for Al, Cu and stainless steel [69, 71]).

	H_2		CH_4		CO		CO_2	
	C	α	C	α	C	α	C	α
Unbaked Al	$3.6\ 10^{-5}$	1.01	$9.4\ 10^{-7}$	1.18	$1.1\ 10^{-5}$	1.07	$4.1\ 10^{-5}$	1.16
Unbaked electrodepo. Cu	$1.4\ 10^{-5}$	1.12	$8.9\ 10^{-7}$	1.12	$2.8\ 10^{-6}$	1.18	$1.5\ 10^{-5}$	1.07
150°C baked Al	$5.9\ 10^{-6}$	1.10	$3.8\ 10^{-7}$	1.20	$2.3\ 10^{-6}$	1.07	$1.6\ 10^{-5}$	1.04
150°C baked OFHC Cu	$2.2\ 10^{-5}$	0.74	$3.7\ 10^{-7}$	0.94	$1.1\ 10^{-6}$	1.01	$1.7\ 10^{-6}$	1.12
150°C baked st. steel	$1.6\ 10^{-6*}$	1.34^{*}	$6.9\ 10^{-7}$	1.00	$1.5\ 10^{-7}$	0.92	$2.6\ 10^{-7}$	0.96

photodesorption yield is also greatly reduced. Table II.8.19 gives the sticking probability and the intrinsic molecular photodesorption yields of a $\sim$ 3 µm TiZrV film irradiated with 4.5 keV critical energy synchrotron radiation at 10 mrad [73].

Table II.8.19: Sticking probability, σ, and molecular photodesorption yield, η, of TiZrV film [73].

	σ_{H_2}	σ_{CH_4}	σ_{CO}	σ_{CO_2}	η_{H_2}	η_{CH_4}	η_{CO}	η_{CO_2}
Non activated TiZrV	0	0	0	0	$1.0\ 10^{-3}$	$2.5\ 10^{-4}$	$5.0\ 10^{-4}$	$3.0\ 10^{-4}$
190°C activated TiZrV	0.007	0	0.5	0.5	$1.5\ 10^{-5}$	$2.0\ 10^{-7}$	$< 1\ 10^{-5}$	$< 2\ 10^{-6}$

The molecular photodesorption yield is also affected by the cryogenic temperature. Primary photodesorption yields decrease while decreasing the temperature from 300 to 5 K. Hydrogen is reduced by a factor five, and CO, CO_2 by at least a factor ten [74].

When molecules are physisorbed on cold surfaces, the desorption yield increases due to the weakly bound molecules. As shown in Table II.8.20 for 250-300 eV critical energy synchrotron radiation and

perpendicular photon irradiation, the hydrogen recycling yield is linear with surface coverage and levels-off at 0.5 molecules/photon above 10^{15} H_2/cm^2. The recycling yield of the other gas is also linear with surface coverage. It equals 10^{-2} molecules/photon at 10^{17}-10^{18} molecules/cm^2 [75].

Table II.8.20: Recycling photodesorption yield, η', at a given surface coverage, θ, for 250-300 eV critical energy synchrotron radiation and perpendicular photon irradiation [75].

	H_2	CH_4	CO	CO_2
η' (molecules/photon)	0.5	0.01	0.01	0.03
θ (molecules/cm^2)	1 10^{15}	1 10^{17}	1 10^{18}	1 10^{18}

Exercise 15: a 3 GeV light source is being designed: the aim is to reach 400 mA current. The dipole field is 0.5 T.

1. What is the critical energy ε_c of such light source?
2. What is the specific photon flux [ph/s/m]?
3. What is the specific power P_0 [W/m]?
4. What is the half vertical opening of the synchrotron radiation fan, in milliradians?
5. Assuming that the photon-stimulated desorption yield is $\eta = 2 \times 10^{-5}$ [molecule/ph], what is the specific gas load Q [mbar·l/s/m]?
6. What is the required specific pumping speed S_{spec} [l/s/m] so that the average pressure P stays below 2×10^{-9} [mbar]?
7. Since the main gas desorbed by photon stimulated desorption is H_2, do you think that such a large pumping speed can be obtained in a chamber of 3 cm diameter with a lumped pumped system?
8. What is the ideal specific pumping speed of a 3 cm diameter beam pipe?
9. What is the required hydrogen sticking probability to fulfil the specification?

II.8.6.3 Vacuum instability and ions stimulated desorption

When the beam circulates in the vacuum chamber, it interacts with the residual gas. In particular, the gas can be ionized. If the ionisation rate and the beam intensity are large enough, the ions bombarding the vacuum chamber walls stimulate molecular desorption. These desorbed molecules may in turn be also ionized increasing further the gas load into the vacuum system. Ultimately, this pressure runaway may lead to an instability (so-called "vacuum instability") leading to a loss of beam intensity or a beam dump.

This effect was discovered at CERN with the Intersecting Storage Rings (ISR), the first hadron collider in the world operating from 1971 until 1984. The 2×943 m long storage rings were colliding protons against protons at 62 GeV in the centre of mass with a luminosity of 4×10^{30} to 1.4×10^{33} Hz/cm^2. Fills were lasting from 50 to 60 h with routinely 30–40 A (with a record at 57 A).

Figure II.8.13 shows the first documented pressure bump in the ISR. When trying to increase the beam current by accumulating more and more pulses, a pressure rise was observed at several places around the ISR. Increasing further the current, the pressure rise increased faster and faster in a non-linear manner. Within a minute, the pressure increased from 10^{-8} to 10^{-6} Torr, leading to beam neutralisation

and loss due to gas scattering. A kind of "critical" beam current was found above which the machine could not be operated.

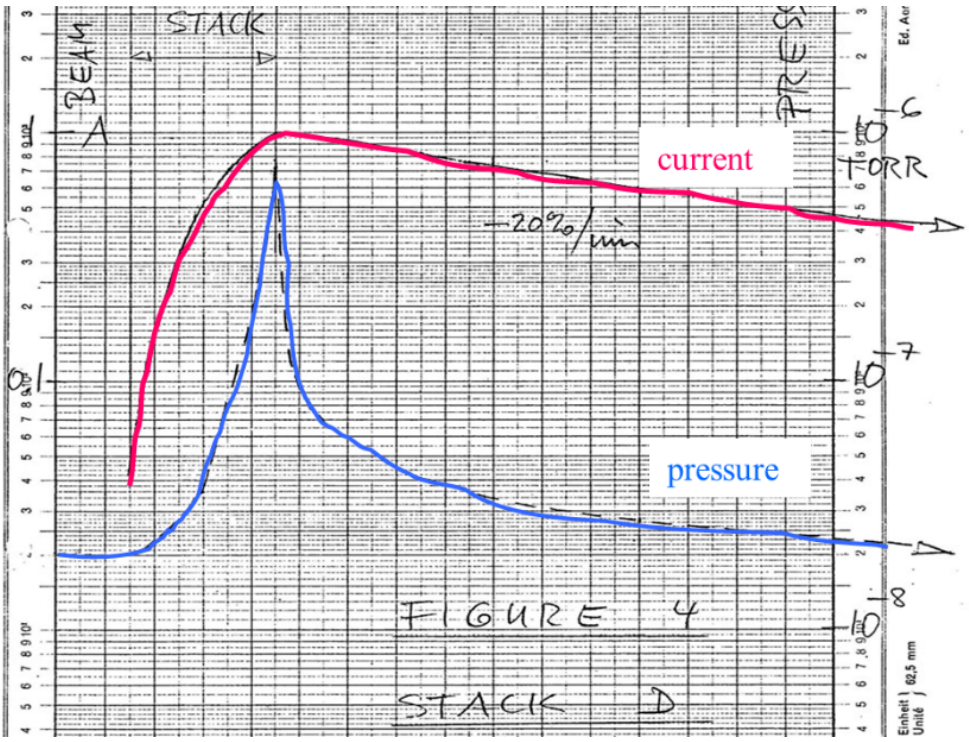

Fig. II.8.13: First documented pressure bump in the ISR. ISR running-in note by E. Fischer, O. Gröbner, E. Jones. Run8, 18 November 1970 [11].

This vacuum instability hampered the first operation years of the ISR despite a static pressure of 10^{-11} Torr was achieved at the machine start up (although it was designed for 10^{-9} Torr!!). This lesson from history is concluded by E. Fischer: "The first experiences have shown that our pessimism has almost compensated our ignorance. Perhaps we should have been still a little more pessimistic—or a little less "ignorant" [76].

The vacuum chamber wall bombardment by the ions and the feedback loop due to the beam gas ionisation phenomena can be modelled using the gas balance equation of Eq. II.8.61 (see Ref. [77]). The first term accounts for thermal desorption, the second term for molecular desorption induced by the ion bombardment and the third term for the gas flow in a conductance-limited system,

$$V\frac{dP}{dt} = Q_0 + 10^3\eta_{\text{ion}}\sigma_{\text{ion}}\frac{I}{e}P + C\frac{d^2P}{dx^2} \quad , \tag{II.8.62}$$

with V the specific volume in l/m, P the pressure in mbar, Q_0 the specific thermal outgassing in mbar.l/s/m, η_{ion} the ion desorption yield in molecules/ion, σ_{ion} the ionisation cross section in m^2, I the beam current, e the elementary charge, C the specific conductance in l/s.m. The factor 10^3 in the 2$^{\text{nd}}$ term accounts for the conversion of cubic metres to litres.

The ionisation cross section is a function of the speed, v, and the charge of the projectile and of the nature of the residual gas [78]. It is given by Eq. II.8.63,

$$\sigma_{\text{ion}} = 4\pi \left(\frac{h/2\pi}{m_e c}\right)^2 \frac{Z^2}{\beta^2}\left[M^2\left(\ln\left(\frac{\beta^2}{1-\beta^2}\right) - \beta^2\right) + C\right] \quad , \qquad \text{(II.8.63)}$$

with $h = 6.62 \times 10^{-34}$ J.s the Plank constant, $m_e = 9.1 \times 10^{-31}$ kg the electron mass, $c = 3 \times 10^6$ m/s the speed of light, Z the atomic number, $\beta = v/c$, M and C constants function of the molecules, see Table II.8.21.

Table II.8.21: M^2 and C constants (see Eq. II.8.63) for atoms and molecules.

	H_2	He	CH_4	H_2O	N_2	CO	O_2	Ar	CO_2
M^2	0.695	0.752	4.23	3.2	3.7	3.7	4.2	4.5	5.75
C	8.115	7.571	41.85	32.3	34.8	35.14	38.8	34.1	55.92

Figure II.8.14 shows the ionisation cross section for protons as a function of the beam energy. At low energy, the ionisation is large, ionisation matters in Linacs. While increasing the energy and the protons become relativistic, the cross section increases due to the logarithmic term, ionisation matters in high energy storage rings. The cross section is large for heavy gases, they must be minimised in accelerator vacuum systems.

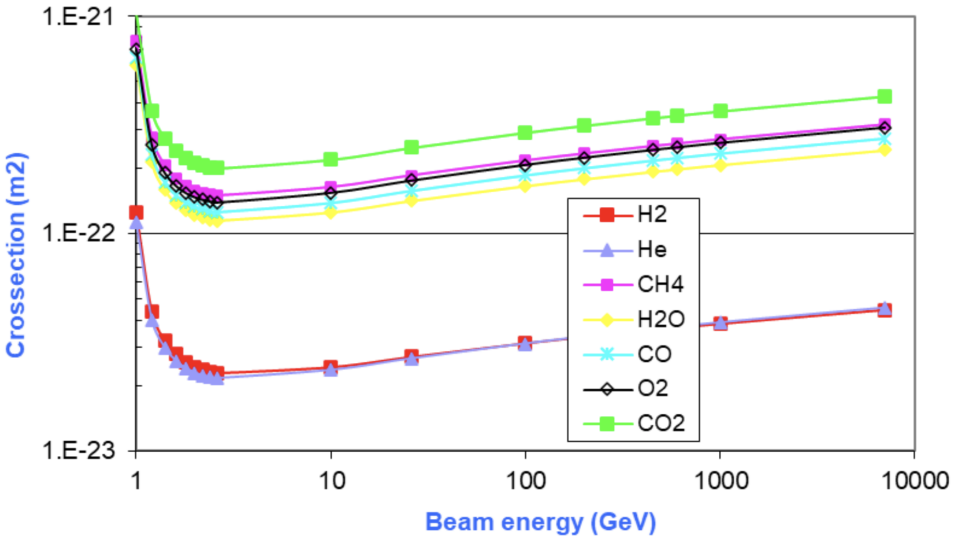

Fig. II.8.14: Ionisation cross section for protons as a function of the beam energy.

Table II.8.22 gives the ionisation cross sections for protons at 26, 450 and 7 000 GeV. As compared to the computed cross section, a correction factor of 1.2 for H_2 and He and 1.5 for the heavier masses was taken to be prudent for the estimations of vacuum stability. This correction factor accounts from deviations observed while comparing the computed data using Eq. II.8.63 and the measured data at the ISR at 26 GeV.

In quasi static conditions ($VdP/dt = 0$) and in a conductance-limited system the 3$^{\text{rd}}$ term on the right can be replaced by $S_{\text{eff}}P$ with S_{eff} the effective pumping speed per unit length, and we have Eq. II.8.64,

Table II.8.22: Ionisation cross sections for protons in 10^{-18} cm^2.

	H_2	He	CH_4	H_2O	N_2	CO	O_2	Ar	CO_2
26 GeV	0.27	0.27	1.9	1.4	1.6	1.6	1.8	1.7	2.5
450 GeV	0.36	0.36	2.5	1.9	2.2	2.2	2.4	2.4	3.4
7 TeV	0.45	0.45	3.2	2.4	2.7	2.7	3.1	3.1	4.3

$$P = \frac{Q_0}{\left(S_{\text{eff}} - 10^3\,\eta_{\text{ion}}\,\sigma_{\text{ion}}\,\frac{I}{e}\right)} \quad . \tag{II.8.64}$$

Clearly, the ion induced molecular desorption term acts in opposition to the effective pumping speed term. When both terms approach each other's, the pressure run away develops and increases towards infinity.

It is convenient to define the critical current at which the pressure tends to infinity,

$$(\eta_{\text{ion}}\,I)_{\text{critical}} = \frac{e\,S_{\text{eff}}}{10^3\,\sigma_{\text{ion}}} \quad . \tag{II.8.65}$$

Therefore, two parameters are important to mitigate the pressure run-away, the beam current and the ion stimulated molecular desorption yield. Of course, the only lever on which the vacuum scientist can play with is the ion desorption.

The ion desorption yield varies with the material, the ion energy and the ion species. Ions being heavy, the desorption yield is close to 1. A beam conditioning can be observed but at high dose above 10^{15} ions/cm^2. Ultimately, ion bombardment may lead to the sputtering of the material and implantation of the ions [79].

The energy of the bombarding ions is a function of their mass, the beam intensity, the beam transverse size, and the presence or not of magnetic fields [52, 80, 81]. Typical ion energy in LHC is in the range of 0.2 – 0.5 keV [10].

Figure II.8.15 shows the molecular desorption yield as a function of ion energy for unbaked and baked stainless steel bombarded by N_2^+. For unbaked material the yield is a few units and reduced by one order of magnitude after bakeout [10, 82].

Beam cleaning being negligible, the ISR solution to overcome the vacuum instability limitation was to increase the number of pumps, reduce the outgassing using 300°C bakeout, and perform an ex-situ Ar/O_2 glow discharge cleaning with in-situ bakeout. Doing so, the critical current increased and the machine could reach 57 A with a pressure of 2 10^{-12} Torr [82, 83].

At cryogenic temperature, in addition to chemically bound molecules, ions can stimulate the desorption of weakly bound, physisorbed, molecules. The yields are therefore very large and about linear with surface coverage, e.g. 2 000 H_2/ion or 2 CO/ion at one monolayer for 5 keV H_2^+ ions [84, 85]. It can be shown that the critical current is modified due to the cryosorbing surface to Eq. II.8.66 (see Ref. [52]),

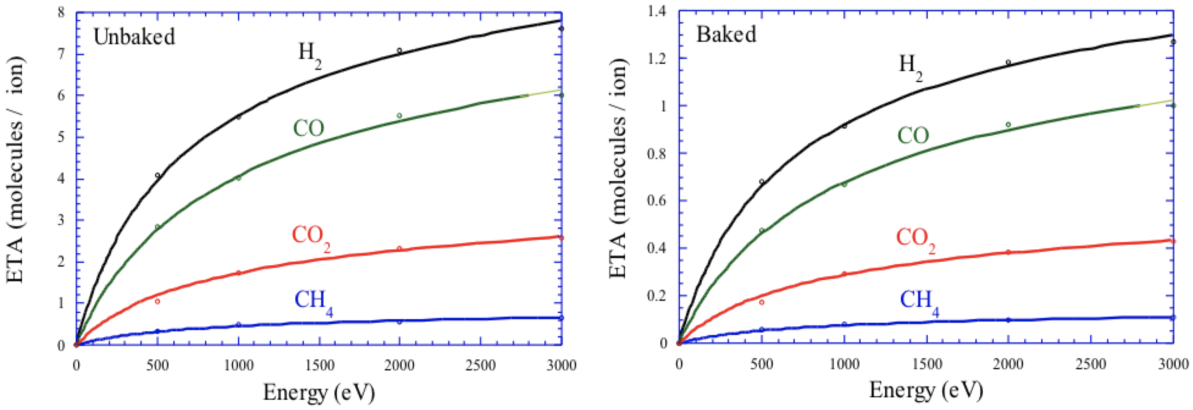

Fig. II.8.15: Molecular desorption yield as a function of ion energy for unbaked (left) and baked (right) stainless steel bombarded by N_2^+ [10].

$$I_{\text{critical}} = \frac{\sigma\, S_{\text{eff}}}{(\eta_{\text{ion}} + \eta\prime_{\text{ion}})\; 10^3\, \frac{\sigma_{\text{ion}}}{e}} \quad , \tag{II.8.66}$$

with $\eta\prime_{\text{ion}}$ the ion desorption yield of physisorbed molecules at 1 monolayer and σ the sticking probability.

Nowadays, accelerators are designed to cope with the vacuum instability, e.g. SNS [86] and LHC [87]. However, the phenomenon still exists and is suspected to reappear under specific circumstances at the time of beam commissioning or unexpected machine parameter modifications, e.g. J-Parc [88].

For ion machines, such as RHIC and LHC, there might be ion losses from the beam. Owing to the high ion energy and the grazing angle, these losses may lead to large pressure increases: 10^{-8} to 10^{-5} mbar [89]. The large yield originates from a surface effect due to thermal activation provoked by the ion bombardment [90]. Desorption yields are extremely large, in the range 20 to 20 000 molecules/ions, as measured by Pb53+ with 4.2 MeV/u and 14 mrad incidence [91]. The desorption yield is determined by the energy given to the electrons (electron stopping force) that subsequently provokes the molecular desorption [92]. Collimators shall be placed around the ring at specific positions to intercept the ion losses and localise the gas load [93].

II.8.6.4 Electron cloud in vacuum systems

II.8.6.4.1 Introduction

First observations of electron clouds in vacuum systems due to beam-induced multipacting are dating from the end of the 70s [94], but it is only recently that the phenomenon became an important limiting factor for the operation of accelerators and storage rings. Nowadays, each machine that is expecting to circulate intense positive bunches shall take into consideration the electron cloud phenomena from its design stage. Although in principle harmful also for negatively charge machines, the beam-induced multipacting is a less limiting factor.

Table II.8.23 shows the machine parameters of some accelerators sensitive to electron clouds.

There is a wide range of machines, with positively charged beams, affected all around the world. Sensitivity to beam-induced multipacting is mostly driven by the bunch population, bunch spacing and the vacuum chamber materials. All types of materials commonly used for vacuum chamber fabrication are therefore concerned. In all these machines, the beam-induced multipacting creates and electron cloud that may render the accelerator unstable above electron densities in the range $0.4 - 10 \times 10^{12}$ e^-/m^3.

Table II.8.23: Parameters of some accelerators sensitive to electron clouds.

	PEPII	**KEKB**	**DAFNE**	**LHC**	**HL-LHC**	**Sup. KEKB**	**ILC DR**	**FCC-hh**
Particle	e^+	e^+	e^+	p	p	e^+	e^+	p
Energy [GeV]	3.1	3.5	0.51	7 000	7 000	4	5	50 000
Lumin. [Hz/cm^2]	3 10^{33}	2 10^{34}	5 10^{32}	1 10^{34}	5 10^{34}	8 10^{35}	na	5 10^{34}
Circumf. [km]	2.2	3	0.1	26.7	26.7	3	3,3	97.8
Nb of bunches	1 658	1 284	120	2 808	2 748	2 500	1 312	10 426
Bunch population	6 10^{10}	9 10^{10}	2 10^{10}	1.2 10^{11}	2.2 10^{11}	9 10^{10}	2 10^{10}	
Bunch spacing [ns]	4.2	7	2.7	25	25	4	554	25
Bunch length [ns]	0.05	0.02	0.1	0.25	0.25	0.02	0.02	0.25
Instab. thresh. [e^-/m^3]	1 10^{12}	4 10^{11}	1 10^{13}	5 10^{11}	1 10^{12}	3 10^{11}	4 10^{10}	4 10^{10}
Material	Al	Cu	Al	Cu/SS	Cu/SS	Cu/Al	Cu	Cu

Electron clouds provoke pressure increases, bunch instabilities along the bunch train, beam size increase and heat load on cryogenic machines. For instance, a pressure increase up to 10^{-8} Torr was observed in the low energy ring of PEP-II above a beam current of 500 mA [95]. A beam size increase from 30 µm to 150 µm was measured at SuperKEK-B while increasing the bunch current from 0.05 mA to 0.35 mA [96]. Bunch instabilities along the train were quantified in the LHC during a "scrubbing" run in Dec. 2012 with 15% loss of the bunch population after the first 300 (100) bunches and 6 (45) minutes following injection in the ring. Finally, heat loads were measured in the LHC cryogenic system above 0.4 10^{11} p/bunch resulting in 15–20 kW at 5–20 K at nominal parameters [97]. Electron cloud is definitively a limiting factor that shall be considered for the vacuum designer [52]!

Like Eq. II.8.59, the pressure increase due to the electron bombardment of the vacuum chamber wall is given by Eq. II.8.67,

$$P = \frac{\eta_{\text{electron}}\,\dot{\Gamma}_{\text{electron}}}{GS} \quad , \tag{II.8.67}$$

with η_{electron} the number of molecules desorbed per incident electron and $\dot{\Gamma}_{\text{electron}}$ the electron flux to the wall.

Figure II.8.16 depicts a schematic build-up of the electron cloud in the LHC. In the bending magnets, the proton bunch produces synchrotron radiation that impinges at grazing angle on the vacuum chamber wall. Electrons are then emitted under the photoelectric effect. These electrons are accelerated to $\sim$ 200 eV towards the opposite wall due to the electric field generated by the highly charged bunch. While impinging on the wall, the photoelectrons may reflect or interact with the material to produce secondary electrons with 1-10 eV. In both cases, these electrons are available for interaction with the next bunch's field 25 ns later for further acceleration towards the wall (0.2–2 keV). The successive passages of bunches spaced by 25 ns lead to an electron cloud build up. Only the absorbed electrons without further electron re-emission are lost and do not participate to the electron cloud build up.

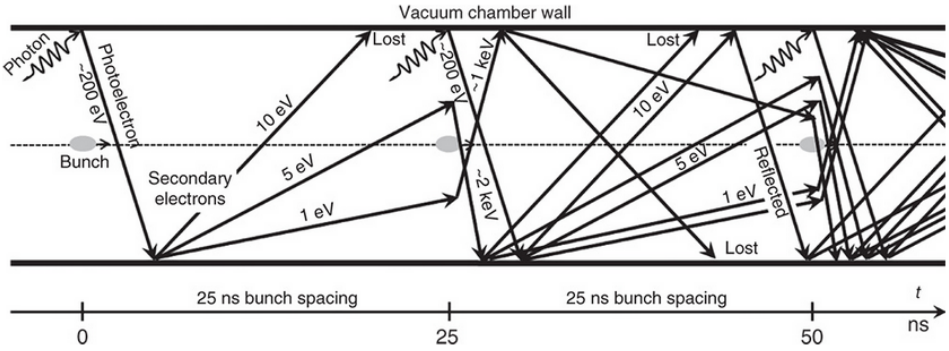

Fig. II.8.16: Schematic electron cloud build-up in the LHC [52].

The electron cloud production is dominated by the multiplication of electrons. It originates from the secondary electron emission and the successive bunch passages before electrons are lost, "beam-induced multipacting". However, for large synchrotron radiation loads, electron clouds can be also dominated by photoelectron production.

The beam-induced multipacting is usually characterised by a threshold: above a given bunch intensity, the multipacting occurs. For LHC, the threshold is at $\sim 5 \times 10^{10}$ proton/bunch for an as received surface but increases further to higher values as "beam conditioning" takes place. To sustain the cryogenic heat load on the LHC beam screens, beam conditioning is required to keep the electrical charge at a reasonable level. The extraction of 8 kW of synchrotron radiation on the 5–20 K beam screen costs 1.4 MW at the electric plug. Adding 1 W/m on the beam screen due to beam-induced electron cloud, leads to 7 MW in total at the electric plug. For the next generation of cryogenic machines, the argument plays in favour on minimising the beam-induced heat loads and extracting them at a higher temperature.

The electron cloud is highly sensitive to magnetic fields. Indeed, the low-energy electrons are confined along the strong magnetic field lines. Consequently, the threshold of multipacting changes with the magnet types. Quadrupoles are the magnets most sensitive to beam-induced multipacting. It has a lower threshold than dipoles. Field-free areas have the highest multipacting threshold. Electrons trapped by the magnetic field lines of a solenoid, do not interact with the bunches, and remain close the vacuum chamber wall and are ultimately absorbed. Hence, multipacting is avoided. Solenoids are therefore routinely used as a mitigation technique against multipacting [98, 99].

The electron cloud build up is a fast phenomenon: a few bunches are required to reach a quasi-steady state regime. The energy distribution of the cloud is dominated by low-energy electrons emitted by the surface (0-50 eV). The quantity of kicked electrons represents only 1% of the low-energy electrons.

The electron cloud is strongly dependent on the bunch intensity, magnetic fields, and filling schemes. All these parameters are linked to the machine properties and performance, they cannot be easily modified.

The main (material) parameter that drives the multipacting effect is the secondary electron yield (SEY). It represents the quantity of emitted electrons from a surface per incident electron. The yield is a function of the energy of the incident electron. It has a maximum, $\delta_{\max}$, at about 200-300 eV. For the LHC dipole, the electron cloud appears when $\delta_{\max} > 1.3$. The threshold for quadrupoles is at 1.1.

Electron cloud can be mitigated by: 1) reducing the photoelectron yield (grazing incidence has larger yield than perpendicular incidence); 2) reducing the secondary electron yield (scrubbing, NEG or amorphous carbon films, geometry); 3) reducing the number of electrons in the system (solenoidal magnetic field, clearing electrodes, material reflectivity) or 4) adapting the beam structure or the vacuum chamber dimensions to reduce the electron multiplication. All these different techniques are implemented for the optimal operation of accelerators sensitive to electron clouds.

II.8.6.4.2 Photon interaction

Photons emitted by synchrotron radiation are intercepted by the vacuum chamber wall. Photons can be reflected either specularly in the forward direction or diffusely in the vacuum chamber cross section plane. High-energy photons can be also transmitted through the material. For instance, the LEP aluminium vacuum chamber was shielded with lead to adsorb as many as possible photons to cope with radiation ageing and to minimise radiation to the personnel. Finally, photons can interact with the material. The penetration depth of photons is about 5 nm in metals. Depending on the photon energy, there are three type of interactions, from low to high energy: 1) photoelectrons can be emitted from the material (the photoelectric effect), 2) photons can elastically scatter on the weakly bound electrons, lose energy and be re-emitted at a different angle while the electron is ejected from the atom (the Compton effect), and 3) the high energy photons in the vicinity of the nucleus can be transformed into a pair of electron and positron (e^+e^- pair production).

Figure II.8.17 shows the photon interaction cross section in Cu as a function of the energy based on data from [100]. Up to 100 keV, the photoelectric effect dominates. In the range 100 keV – 10 MeV, the Compton effect dominates. Above 100 MeV, e^+e^- pair production dominates. The cross section is given in barn (1 barn = 10^{-24} cm^2 = 10^{-28} m^2).

Table II.8.24 gives the dominating regime, photoelectrons or Compton, of different accelerators as determined by their critical energy. As shown, only high-energy lepton rings can be Compton dominated. Therefore, for most of the machines, it is the photoelectric effect that matters.

Table II.8.24: Dominating photon interaction regime of accelerators as determined by their respective critical energy.

Accelerator	**Photoelectrons dominated**	**Compton dominated**
LHC	44.1 eV	
Sync. rad. machine	5-10 keV	
Super KEKB HER	7.3 keV	
FCCee Z pole	19.6 keV	
FCCee WW pole	105.5 keV	0.11 MeV
FCCee ZH pole		0.36 MeV
LEP2		0.75 MeV
FCCee tt pole		1.10 MeV

For the photoelectric effect, the energy of the emitted photoelectrons from the material varies from 0 to ($h\nu - W_\mathrm{F}$) eV, with $h\nu$ the photon energy and W_F the work function of the material. The photoelectron energy distribution curve is dominated by the low-energy part. Most of the photoelectrons

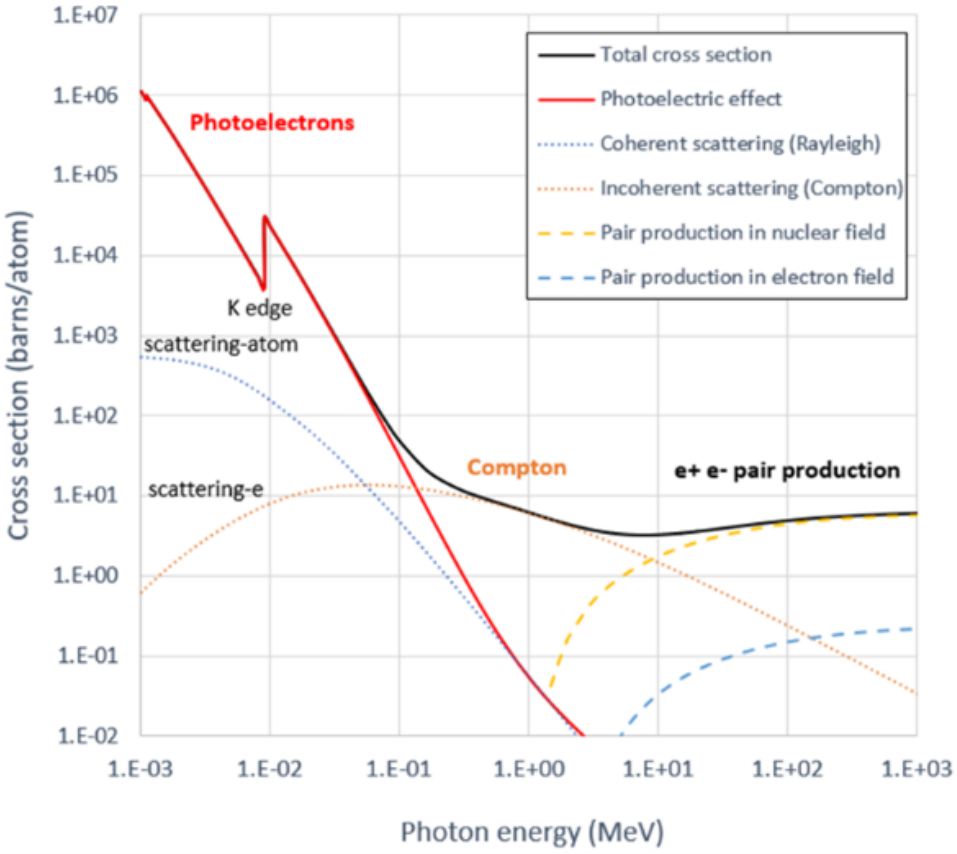

Fig. II.8.17: Photon interaction cross sections in Cu.

are secondary electrons produced in the material with energy < 20 eV. Only a few 0.1% - 1% have higher energies.

Figure II.8.18 shows the photoelectrons distribution produced by 35 and 100 eV photons interacting with gold. The photoelectron kinetic energy distribution is dominated by the low-energy part originating from secondary electrons. The work function edge is visible at 30 eV (the gold work function equals 5.3 eV). The 4f core level electrons (Au 4f7/2 - Au 4f5/2) with a splitting energy of 3.67 eV is also visible. Summing up all photoelectron energy spectra (so-called Energy Distribution Curves, EDC) over the photon energies of the synchrotron radiation spectrum gives the true EDC for accelerators. It can be shown that it is similar to Fig.II.8.18, see Ref. [101].

The synchrotron radiation impinges on the vacuum chamber wall at grazing incidence. The photoelectron reflectivity varies from low value at perpendicular incidence (1%) to a high value at grazing angle (80% on Cu with zero Å roughness for unpolarised photons) [102]. High forward reflectivity is therefore expected in accelerators. However, high-energy photons may be adsorbed. For instance, photons impinging on Cu have an absorption L-edge at $\sim$ 920 eV and are fully absorbed above 3 keV and Al has an absorption L-edge at $\sim$ 65 eV and full absorption above the K-edge at 1.5 keV [102]. Because the photon reflectivity varies with the angle, the photon energy, the nature of the surface, etc., it is therefore desirable to measure the reflectivity properties of the vacuum chamber materials.

Table II.8.25 gives the forward reflectivity (in %) at $\sim$ 10 mrad of some usual materials for differ-

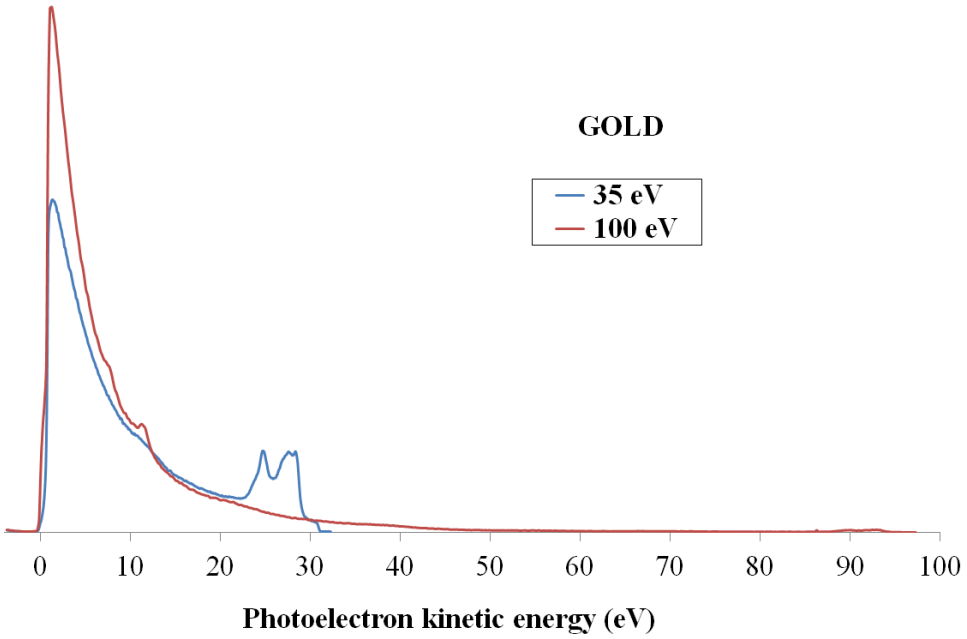

Fig. II.8.18: Photoelectron energy spectra from 35 and 100 eV photons interacting with gold [101].

ent critical energies and surface treatments. The forward reflectivity decreases when the critical energy increases. When smooth, Cu has indeed a large forward reflectivity, which can decrease to 5% for the electroplating case or to 1.8% for the sawtooth case as expected (sawtooth are machined on the Cu material to intercept the photon at quasi perpendicular incidence). NEG films have a forward reflectivity of about 15-20% irrespective of their surface treatment.

Table II.8.25: Forward reflectivity (in %) at $\sim$ 10 mrad of some usual materials for different critical energies [103].

Material	**Treatment**	**45 eV**	**194 eV**	**3-4 keV**
Al	unbaked	-	-	20
Cu roll bounded	unbaked	81	77	33
Cu roll bound. air baked	unbaked	22	18	
Cu electroplated	unbaked	5	7	
Cu sawtooth	unbaked	2	-	
Cu sawtooth	150°C	1	1	
TiZr film	unbaked	20	17	
TiZr film	120°C	20	17	
TiZr film	250°C	20	17	
TiZr film	350°C	21	17	
TiZr film	CO saturated	21	-	

The surface roughness is also an important parameter. Refined reflectivity measurements have shown that Cu with 10 nm roughness (the Cu surface of the LHC beam screen has 15 nm roughness) has a forward reflectivity of 80% at 4 mrad incidence over the photon energy range 35 to 1 850 eV [104]. Such high reflectivity implies that ray tracing programs (e.g. Synrad+ [105]) shall be used to track the

photon trajectories and understand their interactions with the vacuum system. Such high reflectivity also opens the possibility to extract the synchrotron radiation heat load in specific locations held at a temperature close to 300 K bringing important energetic and budget savings for the design and operation of the next generation of superconducting machines [106].

The photoelectron yield, PY*, is defined by the number of emitted photoelectrons per *absorbed* photons. It can be measured at the same time as the forward reflectivity using an experimental system as depicted in Fig. II.8.10. Like the molecular desorption yield, the photoelectron yield decreases under "beam conditioning" but to a moderate extent: only a factor two.

Table II.8.26 gives photoelectron yield per absorbed photon (e/ph) at $\sim$ 10 mrad of some usual materials for different critical energies and surface treatments. PY* increases with increasing critical energy.

Table II.8.26: Photoelectron yield per absorbed photon (e/ph) at $\sim$ 10 mrad of some usual materials for different critical energies [103].

Material	Treatment	45 eV	194 eV	4 keV
Al	unbaked	0.11	0.32	-
Cu-smooth	unbaked	0.11	0.32	0.43
Cu electroplated	unbaked	0.08	0.08	-
Cu sawtooth	unbaked	0.03	0.04	-
TiZr film	unbaked	0.06	0.08	-
TiZr film	350°C	0.02	0.03	-

II.8.6.4.3 Electron interaction

The penetration depth of electrons into a solid surface is 1–10 nm. Primary electrons entering the solid generate secondary electrons which diffuse and can be eventually emitted from the material. The escape depth of the electrons is less than 10 nm and function of the material and the primary electron energy. The emitted electrons are called secondary electrons.

Figure II.8.19 shows the electron EDCs of Cu for 11 and 312 eV primary electron energy. The EDC shows a component at reflected primary electron energy and a larger component at lower energy ($<$ 20 eV). For primary energy below 30 eV, the EDC is dominated by the reflected electrons. For higher energies, secondary electrons dominate [107].

When summing up all the contributions for each primary electron energy, one obtains a so-called secondary electron yield (SEY) curve. Here the secondary electron yield, δ, is defined by Eq. II.8.68,

$$\delta = \frac{\text{number of emitted electrons}}{\text{number of incident electrons}} \quad . \tag{II.8.68}$$

As shown by Fig. II.8.20 for some unbaked technical material, this curve has a maximum for primary electron energies around 200–300 eV with $\delta_{\max} = 2$ to 3.5. The integral of the right curve of Fig. II.8.19 equals about 2 as shown by the intersection of $\mathrm{E_p} = 312$ eV with the curve of Cu. Al has the highest yield; therefore, Al vacuum chambers are usually treated against multipacting.

The SEY curve can be modelled as a function of the primary energy E_p by Eq. II.8.69 (see

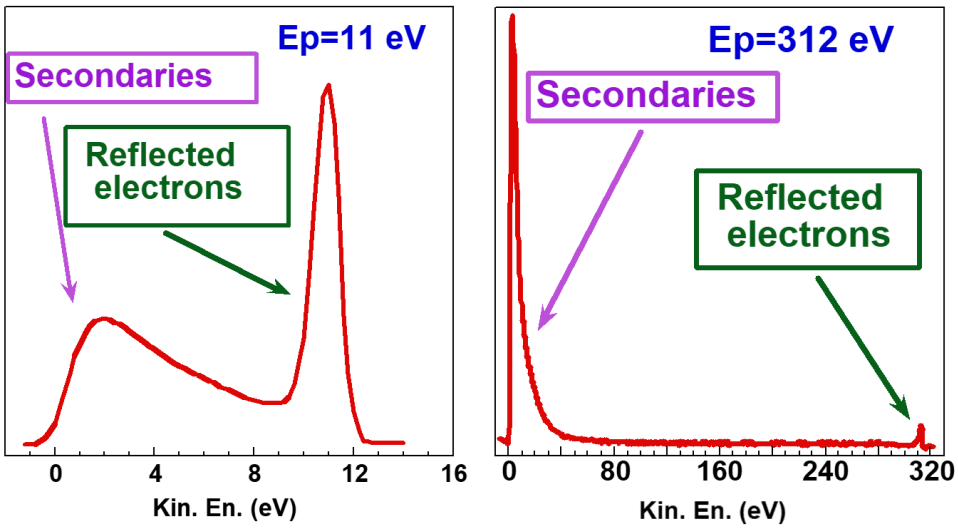

Fig. II.8.19: Electron EDCs of Cu for 11 and 312 eV primary electron energy [107].

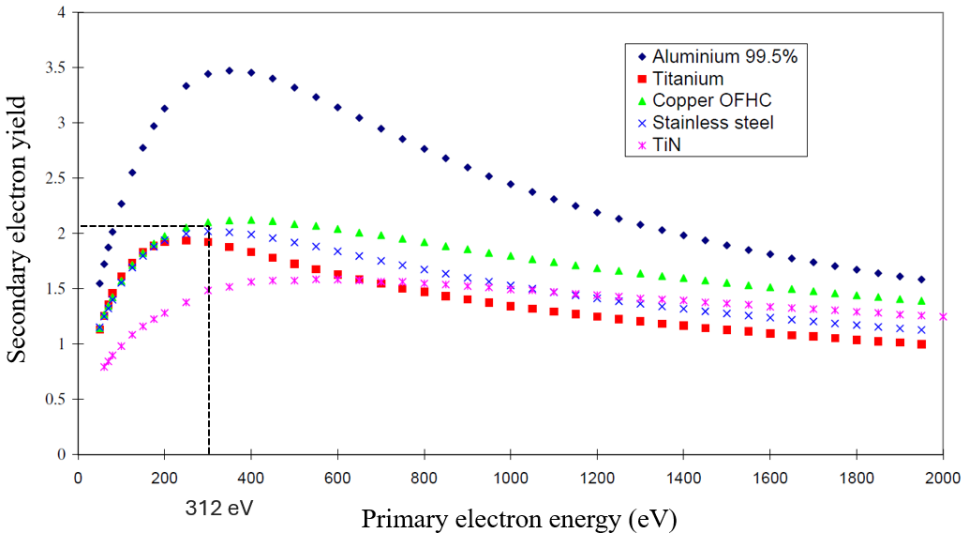

Fig. II.8.20: Secondary electron yield (SEY) curve of some unbaked technical material [108].

Ref. [103]),

$$\delta(E_p) \;=\; R\,\delta_{\text{elastic}}(E_p) \;+\; \delta_{\max}\frac{s\times(E_p/E_{\max})}{s\;-\;1\;+\;(E_p/E_{\max})^s} \quad , \tag{II.8.69}$$

with R the reflectivity at 0 eV, the relative contribution of reflected component, $(E_{\max}, \delta_{\max})$ the coordinates of the curve maximum and a parameter $s \sim 1.4$.

When decreasing the incidence angle, the SEY increases. Introducing the angle, θ, with respect to the surface normal, the parameters $\delta_{\max}$, $E_{\max}$ and s vary like Eq. II.8.70 [109],

$$\begin{aligned} \delta_{\max}(\theta) &= \delta_{\max} e^{0.4\,(1-\cos\theta)} \quad , \\ E_{\max}(\theta) &= E_{\max} \times [1 + 0.7\,(1-\cos\theta)] \quad , \\ s(\theta) &= s \times [1 + 0.18\,(1-\cos\theta)] \quad . \end{aligned} \tag{II.8.70}$$

SEY can be measured using a Faraday cup (or a secondary electron collector) and an electron gun bombarding a sample isolated from ground. Using appropriate bias to repel the electrons and by measuring the drain currents corresponding to the electron beam current and secondary electrons, δ can be computed [52, 110].

As said in the introduction, the SEY is a crucial parameter for the electron multipacting. Several techniques have been developed along the years to lower the SEY to mitigate the electron cloud [52].

In the LHC, TiZrV NEG film, with $\delta_{\max} = 1.1$, is used in the room temperature part of the machine to mitigate electron multipacting [111].

In the cryogenic arcs of the LHC, the SEY reduces thanks to "beam conditioning", i.e. under electron bombardment, towards 1.1-1.3 after an accumulated electron dose of $\sim$ 10 mC/mm^2 [107, 108]. Hence dedicated periods of scrubbing are required for LHC. The SEY reduction is due to a graphitization process owing to the conversion of the carbon bindings from sp^3 to sp^2 [112]. Unfortunately, the physics underlying beam scrubbing is still not fully understood and well mastered. Indeed, during the beam operation and long period of maintenance, the composition of the top layer surface evolves in an uncontrolled way. This led in some circumstances to unexpected high heat load in the LHC arcs limiting the overall machine performance. The observed large SEY originates from the presence of cupric oxide (Cu-II, CuO) and a too low carbon coverage on the high-load beam screens instead of cuprous oxide (Cu-I, Cu_2O) with large enough carbon coverage to allow the graphitization of "standard" beam screens [113].

To alleviate the issue, amorphous carbon will be coated on the beam screens of the High-Luminosity LHC, the LHC upgrade [93]. At cryogenic temperature, the 50 nm thick coating, already successfully used in the CERN SPS on a much thicker version [114], has $\delta_{\max} = 1.1$ [115].

But, at cryogenic temperature, the SEY increases with gas physisorption and its accumulation to large coverages. Thick layers of gas may exhibit $\delta_{\max}$ as large as 1.3, 1.5, 1.9 and 2.2 for CO, CH_4, CO_2 and H_2O respectively. Consequently, a too large accumulation of molecules is forbidden in an accelerator operating at cryogenic temperature.

Beside the production of secondary electrons, the primary electron also stimulates the desorption of neutrals. The molecular electron stimulated desorption (ESD) yield can be measured using the throughput method. A hot filament or an electron gun is used to irradiate a sample that can be isolated from ground. A residual gas analyser allows to measure the gas composition and the partial pressures. The yield is computed from the ratio of the desorbed molecules (using Eq. II.8.25) to the number of incident electrons [11, 12, 52].

Typical ESD yields, η_{electron}, are in the range 10^{-3}–1 molecule/e. The energy threshold for desorption is $\sim$ 10 eV. The yield increases with increasing energy up to 300 eV before levelling-off until 1 keV [116]. The ESD yields of unbaked Cu as a function of energy, E, can be modelled in the 0–300 eV range using Eq. II.8.71 (see Ref. [52]),

$$\eta_{\text{electron}}(E) \;=\; \eta_E \left(\frac{E - E_{\text{th}}}{300 - E_{\text{th}}} \right)^{0.85} \quad , \tag{II.8.71}$$

with the parameters given in Table II.8.27.

Table II.8.27: Fitting parameters.

Molecule	**H_2**	**CH_4**	**H_2O**	**C_2H_6**	**CO**	**CO_2**
η_E [molecule/e]	1.9×10^{0}	2.1×10^{-2}	3.1×10^{-2}	1.1×10^{-1}	5.8×10^{-2}	2.7×10^{-1}
E_{th} [eV]	12.7	7.5	-22.9	11.4	7.2	9.1

A reduction of the ESD yield is observed with the electron dose. The variation of the yield of unbaked Cu with the electron dose, D, when bombarded by 300 eV electrons is given by Eq. II.8.72,

$$\eta_{\text{electron}}(D) \;=\; \eta_0 \left(\frac{D}{D_0} \right)^{-a} \quad , \tag{II.8.72}$$

with the parameters given in Table II.8.28.

Table II.8.28: Fitting parameters.

Molecule	**H_2**	**CH_4**	**H_2O**	**CO**	**CO_2**
η_0[molecule/e]	2×10^{-1}	2.5×10^{-2}	1×10^{-1}	3.5×10^{-2}	5×10^{-2}
D_0 [e/cm^2]	3×10^{14}	1×10^{14}	6×10^{14}	2×10^{14}	4×10^{14}
a	0.47	0.62	0.66	0.49	0.54

By integrating Eq. II.8.72 over the electron dose, one can obtain the quantity, $Q_{\text{electron}}(D)$ (in molecules/cm^2) of desorbed gas after an accumulated dose,

$$Q_{\text{electron}}(D) \;=\; \frac{\eta_0 \, D_0}{1 - a} \left[\left(\frac{D}{D_0} \right)^{1-a} - 1 \right] \quad . \tag{II.8.73}$$

Exercise 16: in the LHC, the electron cloud is set to bombard the unbaked Cu colaminated beam screen during the "scrubbing period". An electron dose of 16 mC/mm^2 is required to fully scrub the beam screen in order to mitigate the electron cloud. How many monolayers of gas have been removed from the surface? Assume the mean electron energy of the electron cloud equals 300 eV and a monolayer 10^{15} molecules/cm^2.

Table II.8.29: Desorbed quantity of gas after an accumulated dose of 16 mC/mm^2 or 10^{19} e/cm^2.

Molecule	**H_2**	**CH_4**	**H_2O**	**CO**	**CO_2**
Q_{electron} [molecule/cm^2]	28×10^{15}	0.5×10^{15}	4.6×10^{15}	3.4×10^{15}	4.6×10^{15}

At cryogenic temperature, it is found that the initial ESD yield is lower than at room temperature, but the conditioning rates are similar, see Fig. II.8.21.

The ESD yield of physisorbed molecules is about linear with the surface coverage. At 4.2 K, values at one monolayer (10^{15} molecules/cm^2) can be large as shown in Table II.8.30 (see also Ref. [116]).

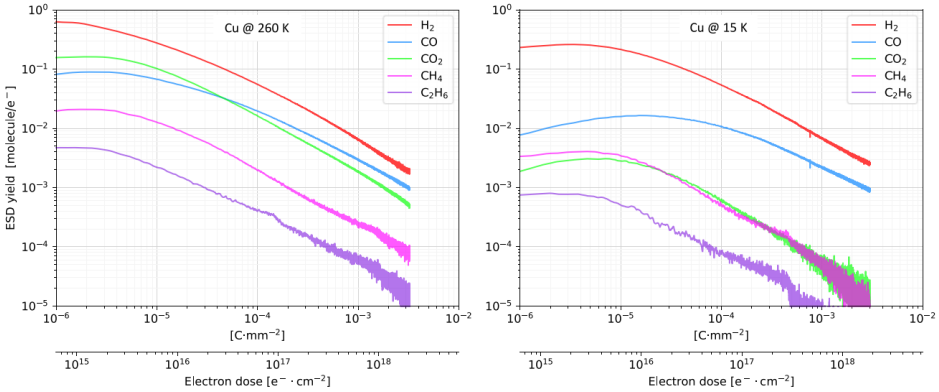

Fig. II.8.21: ESD conditioning curves for LHC grade unbaked Cu held at 260 K and 15 K bombarded by 300 eV electrons [116].

Table II.8.30: Desorption yield of one monolayer of physisorbed gas at 4.2 K bombarded by 300 eV electrons.

Molecule	**H_2**	**CH_4**	**CO**	**CO_2**
η	500	5	10	0.5

The ESD yield of condensed molecules (ice) exhibit a maximum around 300 eV. Under the electron irradiation, ices of H_2O and CO_2 are fragmented into sub-species (H_2, O_2) and (CO, O_2) with the following ESD yields ratio 1:0.4:1.5 for H_2O (which means 1 H_2O/e, 0.4 H_2/e and 1.5 O_2/e) and 1:5:0.3 for CO. A very large fraction (5) of CO_2 is therefore fragmented into CO. The maximum yields are 0.12, 10.5 and 0.38 for H_2O, CO and CO_2 respectively [117].

II.8.7 Design and operation of beam vacuum systems

II.8.7.1 Beam-gas interactions

The cross section, σ, characterises the probability of a particle interaction, for instance when the beam interacts with the atoms of a target. It has the dimension of an area. The unit is 1 barn $= 10^{-28}$ m^2 $= 10^{-24}$ cm^2 (see Refs. [10, 11]).

When a particle beam of intensity, I, crosses a target of thickness dx with a density of atoms n, the change in beam current, dI, is given by Eq. II.8.74,

$$dI = -I\sigma\, n dx \quad . \tag{II.8.74}$$

Noting that $dx = vdt$, with v the speed of the beam particles, one gets Eq. II.8.75,

$$\frac{dI}{dt} = -I\, n\, v\, \sigma \quad . \tag{II.8.75}$$

The evolution of the beam current, Eq. II.8.76, is then given by the integration of the previous equation,

$$I = I_0 \, e^{-\frac{t}{\tau}} \quad , \tag{II.8.76}$$

with I_0 the initial beam current and τ the lifetime given by

$$\tau = \frac{1}{n \, \sigma \, v} \quad . \tag{II.8.77}$$

During the interaction process, the beam current decreases exponentially with a time constant inversely proportional to the gas density and the cross section. A low gas density is required to provide a long beam lifetime. For accelerator physics purpose, it is more convenient to use the gas density than pressure. Hence, the results of computation are usually given in molecules/m^3 rather than mbar.

In a vacuum system, the particles beam interacts differently with the different gas species of density n_i according to their respective cross sections σ_i. For each interaction with a molecule a beam lifetime can be computed,

$$\tau_i = \frac{1}{n_i \, \sigma_i \, v} \quad . \tag{II.8.78}$$

Summing up all the interaction process on the different gas species gives Eq. II.8.79,

$$\sum \frac{dI_i}{dt} = -I \, v \sum n_i \, \sigma_i \quad . \tag{II.8.79}$$

Hence, the beam lifetime is given by Eq. II.8.80,

$$\frac{1}{\tau} = \sum \frac{1}{\tau_i} \quad . \tag{II.8.80}$$

For a vacuum system, this gives Eq. II.8.81,

$$\frac{1}{\tau} = \frac{1}{\tau_{\mathrm{H_2}}} + \frac{1}{\tau_{\mathrm{CH_4}}} + \frac{1}{\tau_{\mathrm{H_2O}}} + \frac{1}{\tau_{\mathrm{CO}}} + \frac{1}{\tau_{\mathrm{CO_2}}} \quad . \tag{II.8.81}$$

As a vacuum system design criterion, the vacuum lifetime must be much larger (i.e. $>>$ 24 h) than other lifetimes, e.g. the particle loss due to the collisions at the interaction points, the particle loss due to the beam collimation, the particle loss due to beam instability, etc.

Beam gas interactions can be divided into two categories: inelastic and elastic interactions. High-energy proton beams may have nuclear scattering and multiple Coulomb scattering. High-energy electron beams may have elastic and inelastic scattering on the nuclear and on the electrons surrounding the nucleus of the residual gas.

In high-energy proton storage rings, the proton beam can interact with the nuclei of the atom [118]. In this case, the scattered proton changes its direction or loses so much energy that it is lost from the beam. Such process is characterised by the nuclear scattering cross section that increases with the beam energy.

Table II.8.31 gives the atomic mass, A, the nuclear cross sections and relative to H_2 cross sections

at 7 TeV for some molecules. The heavier the molecule, the larger the cross section. For instance, a given gas density of CO_2 will reduce the beam lifetime by a factor ~ 14 as compared to the same gas density of hydrogen. As a vacuum system design criterion, the gas density of heavy molecules shall be minimised.

Table II.8.31: Atomic mass with nuclear scattering cross sections and relative cross sections at 7 TeV.

Molecule	**H_2**	**He**	**CH_4**	**H_2O**	**CO**	**N_2**	**O_2**	**CO_2**	**Kr**	**Xe**
A	2	2	16	18	28	28	32	44	84	131
σ [mb]	95	126	566	565	854	820	924	1317	2177	3231
$\sigma_{\mathrm{rel},i}$	1	1.33	5.96	854	8.99	8.63	9.73	13.86	22.92	34.01

For vacuum system design, it is convenient to express the gas density in H_2-equivalent as if there were only one gas species,

$$n_{\mathrm{H_2\,eq}} = \sum n_i \, \sigma_{\mathrm{rel},i} \quad . \tag{II.8.82}$$

Exercise 17: in the LHC, the vacuum lifetime is set at 100 h. What are the corresponding gas density and pressure (at room temperature, $T = 300$ K) for H_2 and CO assuming a single gas composition?

Exercise 18: assume a gas mixture of H_2 and CO, with 2 10^{14} H_2 m^{-3} and 5 10^{13} CO m^{-3}, i.e. a total pressure of 10^{-8} mbar, what would be the vacuum lifetime?

From the previous exercises, one sees that the knowledge of the gas density for each molecular species matters and not only the level of the (total) pressure.

At a proton beam energy lower than 3 TeV, multiple Coulomb scattering may dominate. A single Coulomb scattering event is due to the elastic scattering via electro-magnetic forces of an incoming particle on a nucleus. Multiple Coulomb scattering is due to a series of small-angle scattering events which lead to the gradual blow up of the beam emittance, ε and thus the transverse beam dimension σ_x.

The multiple scattering characteristic time, τ_m, is directly proportional to the beam momentum p,

$$\tau_m[\mathrm{hour}] = 1.13 \times 10^{22} \frac{\varepsilon}{G\langle\beta\rangle} \frac{p^2}{n} \quad \alpha \quad \frac{p^2}{\gamma} \quad \alpha \quad p \quad , \tag{II.8.83}$$

with G the gas factor, n the gas density, p the particle momentum (GeV/c), $\langle\beta\rangle$ the average beta function (m) and $\varepsilon = \varepsilon_0/\gamma$ the beam emittance (m rad). Table II.8.32 gives the gas factor, G.

Table II.8.32: Atomic mass A and gas factor G for multiple Coulomb scattering.

Molecule	**H_2**	**He**	**CH_4**	**H_2O**	**CO**	**N_2**	**O_2**	**Ar**	**CO_2**
A	2	2	16	18	28	28	32	40	44
G	21.10	39.45	370.86	593.10	900.66	884.60	1 144.00	2 709.26	1 472.66

In electron storage rings, the beam lifetime depends on the four scattering cross sections (nuclear elastic and inelastic scattering and elastic and inelastic electron scattering from the electrons surrounding the nucleus of the residual gas such that $\sigma = \sigma_1 + \sigma_2 + \sigma_3 + \sigma_4$.

The nuclear elastic scattering is given by Eq. II.8.84,

$$\sigma_1 \;=\; 1.305\,10^{-35}\,\frac{Z^2}{E^2}\left[\left(\frac{\langle\beta_H\rangle}{a}\right)^2 + \left(\frac{\langle\beta_V\rangle}{b}\right)^2\right] \quad . \tag{II.8.84}$$

The nuclear inelastic scattering is given by Eq. II.8.85,

$$\sigma_2 \;=\; 3.09\,10^{-31}\,Z^2\ln\!\left(\frac{183}{Z^{1/3}}\right)\left[\ln\!\left(\frac{1}{\chi_{\rm RF}}\right) - 5/8\right] \quad . \tag{II.8.85}$$

The elastic scattering from electrons surrounding the nucleus of the residual gas is given by Eq. II.8.86,

$$\sigma_3 \;=\; 2.55\,10^{-32}\,\frac{Z}{\chi_{\rm RF}\,E} \quad . \tag{II.8.86}$$

The inelastic elastic scattering from electrons surrounding the nucleus of the residual gas is given by Eq. II.8.87,

$$\sigma_4 \;=\; 3.09\,10^{-31}\,Z\left[\ln\!\left(\frac{4.89\,10^3\,E}{\chi_{\rm RF}}\right) - 1.4\right]\left[\ln\!\left(\frac{1}{\chi_{\rm RF}}\right) - \frac{5}{8}\right] \quad . \tag{II.8.87}$$

Here, σ_i is the cross section in m^2, Z the atomic number (i.e. 6 for C), E the beam energy (GeV), a the semi-horizontal chamber dimension (m), b the semi-vertical chamber dimension (m), $\langle\beta\rangle$, the average beta in H and V plane (m), $\varepsilon_{\rm RF} = \chi_{\rm RF}E$, the maximum allowable energy spread in the RF ($\chi_{RF} \ll 1$).

II.8.7.2 Pressure profiles

Although many codes are available to compute the pressure in accelerator vacuum systems, it is useful to understand and derive the fundamental equations of pressure profiles [119].

We analyse first the case of a **lumped pumping system**. Let's consider a vacuum chamber of uniform cross-section, with specific surface A [cm^2/m] (surface per meter of vacuum chamber), specific outgassing rate q [mbar.l/s/cm^2] and equal pumps (of pumping speed S [l/s] each) evenly spaced at a distance L in [m]. Q is the gas throughput in [mbar.l/s]. The specific conductance is c in [l.m/s]. The total outgassing rate is $AqL = Q_{\rm tot}$ [mbar.l/s].

By virtue of Eq.II.8.10 and by definition of the total outgassing rate, one can write the following equations for an elemental chamber,

$$\begin{cases} Q(x) &= -\,c\,\frac{dP(x)}{dx} \quad , \\ \frac{dQ(x)}{dx} &= A\,q \quad . \end{cases} \tag{II.8.88}$$

Differentiating the first one and substituting in the second one, we obtain Eq. II.8.89,

$$c\,\frac{d^2\,P(x)}{dx^2} \;=\; -\,A\,q \quad . \tag{II.8.89}$$

The boundary conditions are given by Eq. II.8.90,

$$\begin{cases} \left.\frac{dP(x)}{dx}\right|_{x=L/2} = 0 \quad , \\ \left.P(x)\right|_{x=0} = 2\frac{A\,q\,L/2}{S} \quad . \end{cases} \tag{II.8.90}$$

The pressure is maximum at the middle ($x = L/2$) between the pumps and the pressure at the pump is the total outgassing of twice the half distance between pumps ($2 \times L/2$) over the pumping speed (S). The solution is a second-order polynomial, the pressure profile is parabolic with a minimum at the pumps and a maximum between the pumps,

$$P(x) = \frac{Aq}{2c}\left(Lx - x^2\right) + \frac{AqL}{S} \quad . \tag{II.8.91}$$

The maximum pressure is given by

$$P_{\max} = P(L/2) = A\,q\,L\left(\frac{1}{S} + \frac{L}{8c}\right) \quad . \tag{II.8.92}$$

Therefore, the lowest achievable pressure given by an infinitely large pumping speed is

$$P_{\max,\infty} = A\,q\,\frac{L^2}{8c} \quad . \tag{II.8.93}$$

The circulating particle beam interacts with the average pressure, given by Eq. II.8.94,

$$P_{\text{av}} = \frac{1}{L}\int_0^L P(x)\,dx = A\,q\,L\left(\frac{1}{S} + \frac{L}{12\,c}\right) \quad . \tag{II.8.94}$$

Noting that the total outgassing rate, Q, equals AqL, and remembering that $Q = P_{\text{av}} S_{\text{eff}}$, one can identify the effective pumping speed from Eq. II.8.95,

$$S_{\text{eff}} = \left(\frac{1}{S} + \frac{L}{12\,c}\right)^{-1} \quad , \tag{II.8.95}$$

or the specific pumping speed, $S_{\text{spec}} = S_{\text{eff}}/L$ in l/s/m.

The lowest achievable average pressure in a lumped pump system obtained when the pumping speed S of the pump is infinite,

$$P_{av,\infty} = A\,q\,\frac{L^2}{12\,c} \quad . \tag{II.8.96}$$

In such a pumping system, the average pressure seen by the beam is limited by the distance between the pumps and the specific conductance. A low average pressure requires a small distance between pumps and a large specific conductance.

Exercise 19: assume a beam pipe of 5 cm diameter, e.g. the LHC cold bore, with specific conductance 15 l/s.m. Assuming a specific outgassing rate of 7×10^{-13} mbar.l/s/cm^2 (outgassing rate of baked stain-

less steel), what size of pumps and which distance is required to reach an average pressure of 10^{-8} mbar around the ring?

The plot of the effective pumping speed of the LHC cold bore as a function of the distance between the pumps shows that the system is conductance limited when the pumps distance is larger than $\sim$ 10 m, see Fig. II.8.22. Assuming the use of pumps with infinite pumping speed, the maximum distance between the pumps shall be less than 40 m ($\sqrt{12cP_{\max}/Aq}$). This is not applicable in a large circumference ring; indeed, this would mean the use of 675 pumps per proton ring! Fortunately, the LHC is based on a distributed pumping system!

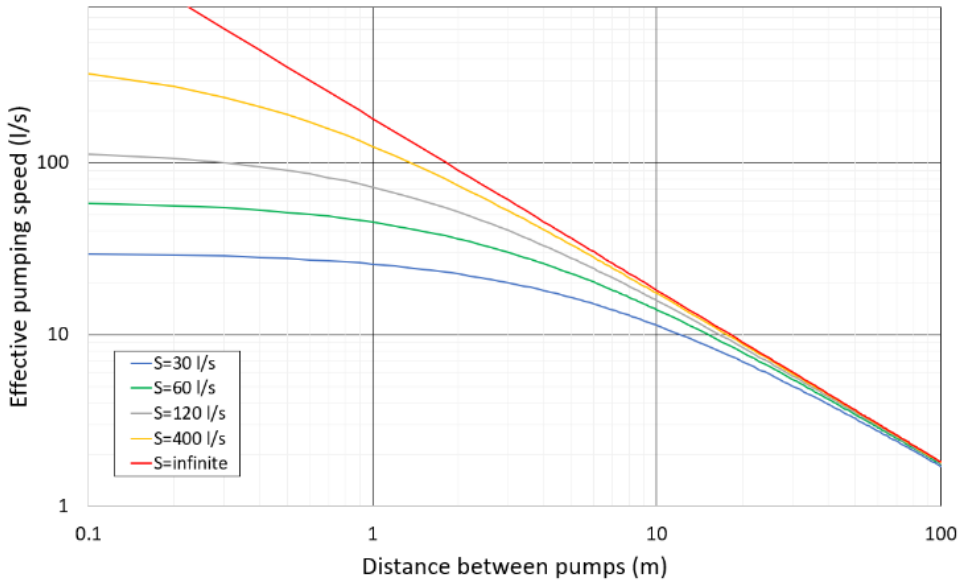

Fig. II.8.22: Effective pumping speed of a lumped pumping system for different pump sizes as a function of the distance between pumps. The specific conductance is 15 l/s·m.

In a **distributed pumping system**, each portion of the beam pipe provides pumping. For this purpose, NEG can be used at room temperature and cryopumping at cryogenic temperature. The LEP vacuum system, the room temperature, and the cryogenic temperature part of the LHC vacuum system are distributed pumping systems.

The gas balance equation in such an elemental vacuum chamber can be written as Eq. II.8.97,

$$V\frac{dP}{dt} = a + (b-s)\,P + c\frac{d^2P}{dx^2} \quad , \tag{II.8.97}$$

with a the linear outgassing rate in mbar.l/s/m, s the linear pumping speed in l/s/m, b the ion induced desorption in l/s/m, c the specific conductance of the vacuum chamber in l/s.m and V the vacuum chamber volume per unit of length in l/m. The variation of pressure in the volume with time is due to:

- the first term for molecular desorption (thermal, PSD, ESD),
- the second term for ion-induced molecular desorption and the (NEG or cryogenic) surface pumping, and
- the third term for the gas flow in a conductance-limited system.

In quasi-static conditions and for long tubes ($c = 0$), the pressure is independent of the longitudinal position (see Eq. II.8.98). P_{inf} is the pressure of an infinitely long tube, i.e. a conductance-limited tube. The more a tube is conductance-limited, the less the pressure at the extremity of a short tube modifies the pressure in the tube,

$$P_{\text{inf}} = \frac{a}{s-b} \quad . \tag{II.8.98}$$

For short tubes that are not conductance limited, $c \neq 0$. The solution for a distributed lumped pumping system (distance between pumps L, pumping speed S) is

$$P(x) = A\, e^{-\lambda x} + B\, e^{\lambda x} + \frac{a}{\lambda^2\, c} \quad , \tag{II.8.99}$$

with $\lambda = \frac{s-b}{c}$. The constants A and B can be derived from the boundary conditions that express the conservation of flow at a pump,

$$\begin{cases} c\,\frac{dP(x)}{dx}\Big|_{x=L/2} &= -\,P(L/2)\,S \quad , \\ c\,\frac{dP(x)}{dx}\Big|_{x=-L/2} &= +\,P(-L/2)\,S \quad . \end{cases} \tag{II.8.100}$$

So, the pressure profile in a non conductance limited distributed and lumped pumping system is

$$P(x) = P_{\text{inf}} \left(1 - \frac{\cosh(\lambda x)}{\cosh(\lambda L)\left(1 + \frac{c}{S}\lambda \tanh(\lambda L)\right)} \right) \quad . \tag{II.8.101}$$

It can be shown that for a specific conductance below $121\,\text{l/s}\cdot\text{m}$, the second term vanishes for $x > 0.5$ m. Half a metre away from the pump, the pressure of a "short" tube is dominated by the pressure of a long tube (see Eq. II.8.98).

Different software can be used to compute the gas density profiles in vacuum systems more complex than a distributed pumping system. At CERN, VASCO is used to compute the vacuum stability and the 1D gas density profile [120] and Molflow+ is a particle Monte-Carlo simulator to compute the 3D gas density profile of vacuum systems [105].

II.8.7.3 An example: the LHC

The LHC vacuum system comprises a cryogenic vacuum system in the arcs and a room temperature vacuum system in the long straight sections and experimental areas. The vacuum system was designed to provide vacuum stability and to cope with synchrotron radiation and electron cloud [122].

The vacuum system design sets a lifetime limit due to nuclear scattering at 100 h equivalent to an hydrogen gas density of 10^{15} H_2/m^3. As shown above, this corresponds to an average pressure in the arc of $\sim 10^{-8}$ mbar hydrogen equivalent. As computed using Eq. II.8.102,

$$H = \frac{IE}{c\tau} = 0.93\,\frac{E[\text{TeV}]\,I[\text{A}]}{\tau[\text{h}]} \quad , \tag{II.8.102}$$

Table II.8.33: ATLAS, CMS and Long Straight Section 1 & 5 vacuum system design values [121].

	H_{2_eq} / m^3	mbar
<LSS$_{1\ or\ 5}$>	5 10^{12}	2 10^{-10}
<ATLAS>	1 10^{11}	4 10^{-12}
<CMS>	5 10^{12}	2 10^{-10}

the corresponding heat load, H, on the cold mass due to nuclear scattering from both beams is 80 mW/m. It represents an upper limit for the 1.9 K cryogenic system for which the nuclear scattering on the residual gas represents a non-negligible heat load. In the experimental areas, the vacuum system was optimised to minimise the beam-gas background to the experiments. Table II.8.33 gives the design values for the two high luminosity experiments [121].

In the LHC arc, a beam screen is inserted to intercept the heat load induced by the circulating beam and protect the cold bore held at 1.9 K, see Fig. II.8.23. The beam screen operates in the range 5–20 K. Two ID 3.7 mm cooling tubes are laser welded on the top and bottom face of the beam screen to provide 1.1 W/m distributed heat load extraction at the maximum. The laser welding is not fully penetrating to avoid helium leaks in the beam vacuum. The racetrack shape beam screen is made of a Cu-colaminated on stainless steel strip that is perforated before forming and welding. The 75 µm thick Cu allows circulation of the beam image currents while the 1 mm thick a-magnetic stainless steel provides stiffness to the structure during a quench (resisting against eddy-current forces of several tons) and preserve the quality of the magnetic field. Pumping slots with a surface area of 4.4% provide a distributed pumping speed to control the gas density. The shape and size of the randomly positioned slots is optimised to minimise the beam-induced heat load onto the cold bore to below 1 mW/m and their impact on the longitudinal and transverse beam impedance (maximum slot width < 1.5 mm). Sawteeth of 40 µm high with 500 µm pitch, are produced on the horizontal plane to intercept the synchrotron radiation light at perpendicular incidence to minimise the number of photoelectrons and forward reflectivity. Pumping slot shields are clipped on the cooling tube to intercept the electrons of the electron cloud circulating along the magnetic field lines to protect the 1.9 K cold bore from direct bombardment. CuBe sliding ring are placed every half metre to allow an ease insertion of the 16 m long beam screen into the cold bore while minimising the heat transfer to the cold bore below 4.3 mW/m. The beam screen aperture is optimised for beam optics: 44 mm radial ID and 34.3 mm between flats ID.

The perforations in the LHC beam screen are essential to control the gas density as originally foreseen [123, 124]. The Superconducting Super Collider was a $20 + 20$ TeV proton-proton collider project with 87 km circumference collider located in Texas, which was cancelled by the US congress in 1993. Experimental studies using synchrotron radiation performed for the SSC studies demonstrated that for a non-perforated beam screen, the hydrogen pressure could reach 10^{-7} mbar after a couple of hours of photon irradiation. A second experiment conducted this time with a perforated beam screen allowed to keep the pressure well below 10^{-9} mbar [125]. These results were later confirmed for the LHC type beam screen [126, 127].

The gas density and the surface coverage evolution in time in a cryogenic accelerator can be described by Eqs. II.8.103,

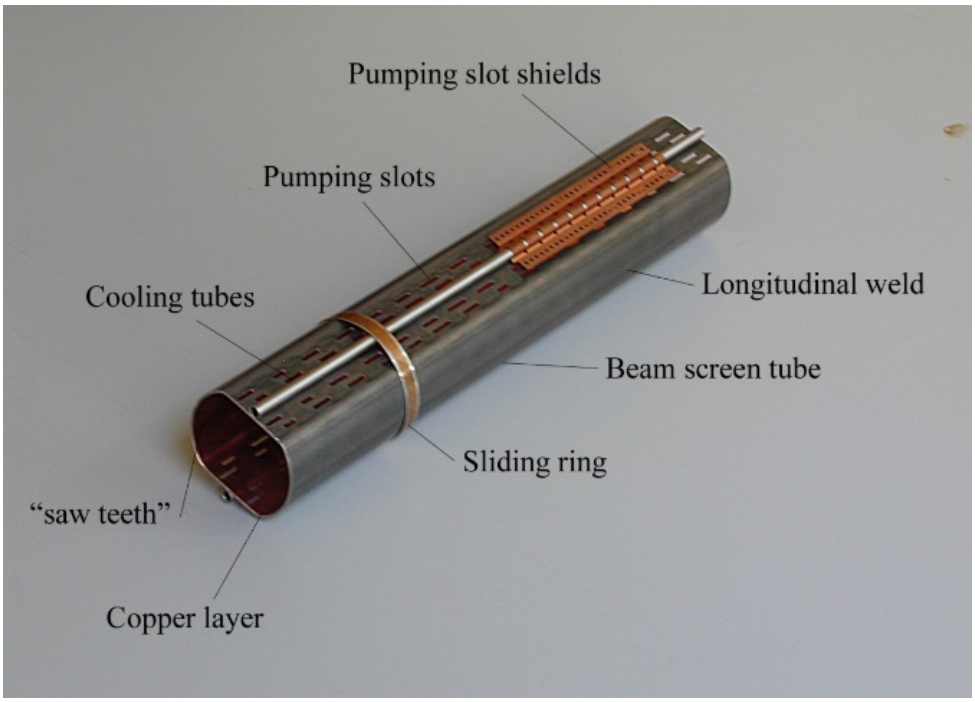

Fig. II.8.23: The LHC beam screen.

$$\begin{cases} V\,\frac{\partial n}{\partial t} & = \eta\,\dot{\Gamma} + \eta\prime\,\dot{\Gamma} + \frac{A\,\theta}{\tau} - \sigma\,S\,n - C\,n + A_c\,D\frac{\partial^2 n}{\partial z^2} \quad , \\ A\,\frac{\partial \theta}{\partial t} & = \sigma\,S\,n - \eta\prime\,\dot{\Gamma} - \frac{A\,\theta}{\tau} \quad , \end{cases} \tag{II.8.103}$$

with V the volume per unit length [m^3/m], A the surface per unit length [m^2/m], σ the sticking probability, and $\dot{\Gamma}$ the particle flux [particle/m/s].

The first equation describes the gas density, η in [molecules/m^3], increases due to: 1) the first term that accounts for photon (or electron) stimulated molecular desorption, with η the (primary) desorption yield of chemisorbed molecules [molecules/particle], 2) the second term that accounts for photon (or electron) stimulated molecular desorption of physisorbed molecules, with η' the recycling (secondary) desorption yield of physisorbed molecules [molecules/particle], 3) the third term that accounts for the vapour pressure, with τ the sojourn time of physisorbed molecule [s], and 4) the sixth term that accounts for the axial diffusion (that is negligible in conductance-limited vacuum systems), with A_cD the specific conductance per unit axial length [m^4/s], $A_c = \pi r^2$ the tube section of radius r and the Knudsen diffusion coefficient $D = (2/3)rv$, with v the mean molecular velocity. Hence, $A_cD = \pi d^3 v/12$.

This first equation describes also the gas density decreases due to 1) the fourth term that accounts for cryopumping on the cold surface, with S the ideal pumping speed per unit length [m^3/s/m], 2) the fifth term that accounts for pumping through the beam screen holes, with C the beam screen holes pumping speed per unit length [m^3/s/m].

The second equation describes the surface coverage, θ in [molecules/cm^2], increases due to the first term that represents the cryopumping on the cold surface and the surface coverage decreases due to the second and third term that represent the physisorbed molecules leaving the cold surface under particle

bombardment and the vapour pressure.

Note that the two time dependent equations are coupled. In particular, the recycling desorption yield, the vapour pressure and the sticking probability are functions of the surface coverage. Therefore, exact solutions cannot be found. We will neglect here the axial diffusion term ($A_c D = 0$) and consider that the system evolves in quasi-static conditions, therefore $V dn/dt = 0$.

We consider first a cryosorbing tube without pumping holes ($C = 0$). Since $V dn/dt = 0$, the gas density is given by Eq. II.8.104,

$$n = \frac{\eta \dot{\Gamma}}{\sigma S} + \frac{\eta\prime(\theta)\dot{\Gamma}}{\sigma S} + \frac{1}{\sigma S}\frac{A\,\theta}{\tau} \quad . \tag{II.8.104}$$

The gas density is the sum of the gas density increases due to primary desorption, recycling desorption and vapour pressure. We note that the second and third terms are increasing functions with the gas density. We obtain the surface coverage equation by inserting Eq. II.8.104 in the second equation of Eq. II.8.103. The surface coverage variation with the particle dose is the given by Eq. II.8.105,

$$\theta = \frac{1}{A}\int_0^{\Gamma} \eta \, d\Gamma \quad . \tag{II.8.105}$$

All the (primarily) desorbed molecules are cryopumped on the cold surface and consequently the surface coverage increases when the particle dose increases.

For illustration, Fig. II.8.24 shows the gas density and surface coverage evolutions in a long cryosorbing tube irradiated by synchrotron radiation. For comparison, the 100 h lifetime limit at 10^{15} H_2/m^3 is shown. The parameters used for the computation, and applicable to the LHC case, are = 10^{17} ph.m^{-1}.s^{-1}, η = 10^{-4} H_2/ph, η'_0 = 1 H_2/ph (see Section II.8.6.2). We assume that the recycling desorption yield of hydrogen scales linearly with the surface coverage like $\eta\prime(\theta) = \eta'_0\theta/\theta_m$ where θ_m is the monolayer surface coverage. The sticking probability is assumed to vary linearly with relative surface coverage starting at 0.2 and reaching 1 at a monolayer (see Section II.8.5.1).

At the beginning, the gas density is dominated by the primary desorption. During the photon irradiation, the desorbed gas, being captured in the closed geometry, is pumped on the cryosorbing surface. As a result, the recycling desorption increases and become dominant from 100 s until 30 h. During this period, the lifetime limit is already overpassed. Later, the vapour pressure increases with increasing surface coverage. When it approaches one monolayer, the vapour pressure dominates and then levels-off at the saturated vapour pressure (10^{18} H_2/m^3). Obviously, this type of cryosorbing tube is not acceptable for the LHC design!

We consider now a cryosorbing tube with pumping holes ($C \neq 0$), i.e. the LHC beam screen. In quasi-static conditions ($V dn/dt = 0$), the gas density in the system and the surface coverage increase like in the previous case. But here, the surface coverage ceases to increase (i.e. $A\,d\theta = 0$) when the flux of recycled molecules (the vapour pressure being negligible), $\eta'\dot{\Gamma}$, is exactly balanced by the flux of molecules pumped on the cold surface, $\sigma S n$. At this instant, the gas density reaches an equilibrium where the flux of the primary desorbed molecules from the cold surface is equal to the flux of molecules pumped through the holes. This equilibrium gas density, n_{eq}, is given by Eq. II.8.106,

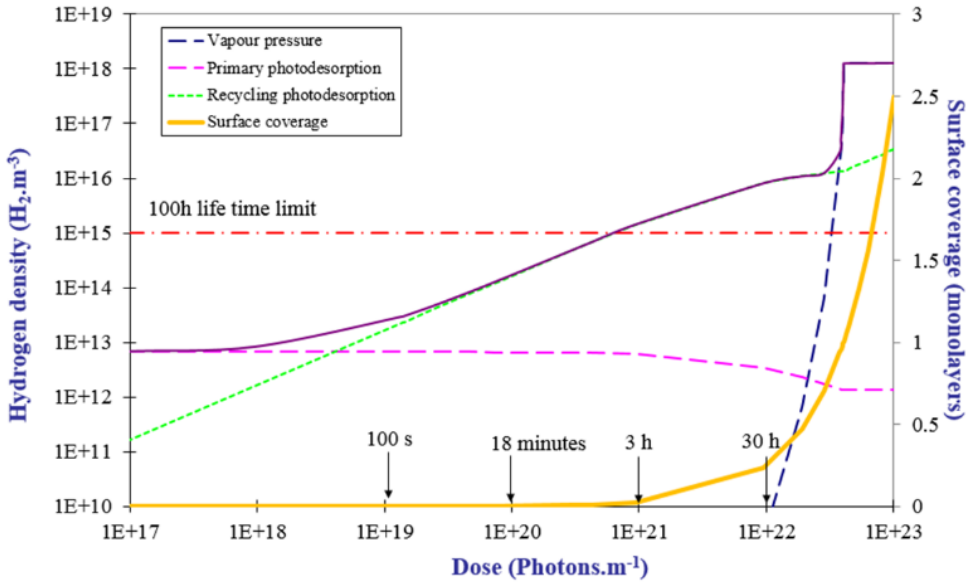

Fig. II.8.24: Gas density and surface coverage evolution in a long cryosorbing tube as a function of the photon irradiation dose.

$$n_{\mathrm{eq}} = \frac{\eta \dot{\Gamma}}{C} \quad . \tag{II.8.106}$$

The level of the equilibrium gas density is simply defined by the gas load of the primary desorption to the pumping speed of the beam screen holes. The percentage of holes in the beam screen defines the equilibrium gas density level.

Assuming a linear dependency of the recycling desorption yield with the surface coverage, the equilibrium surface coverage, θ_{eq}, is given by Eq. II.8.107,

$$\theta_{\mathrm{eq}} = \left(\frac{\sigma S}{C} \frac{\eta}{\eta_0'} \right) \theta_m \quad . \tag{II.8.107}$$

The larger the sticking probability and the primary desorption yield, the larger the equilibrium surface coverage. Conversely, the larger the beam screen pumping speed and the recycling desorption yield, the lower the equilibrium coverage.

From the data in Table II.8.20, we conclude that under synchrotron radiation all gases, except hydrogen, may accumulate on the beam screen cold surface to large equilibrium surface coverage. But, from the data in Table II.8.30, we conclude that under electron bombardment, a tiny quantity of molecules may accumulate on the beam screen surface.

Figure II.8.25 shows the gas density and surface coverage evolution in a long perforated cryosorbing tube as a function of the photon irradiation dose. At first, the pressure increases with the increasing surface coverage originating from the cryosorption of primary desorbed molecules. When the flux of recycled gas is exactly balanced by the flux of pumped gas onto the inner surface of the beam screen, the surface coverage ceases to increase. An equilibrium is then reached, and everything is happening as

if all the primary desorbed gas is pumped by the beam screen perforation. After 100 s of photon irradiation, the equilibrium gas density is reached at 6 10^{13} H_2/cm^2 with an equilibrium surface coverage of 8×10^{-4} monolayers (2.5×10^{12} H_2/cm^2).

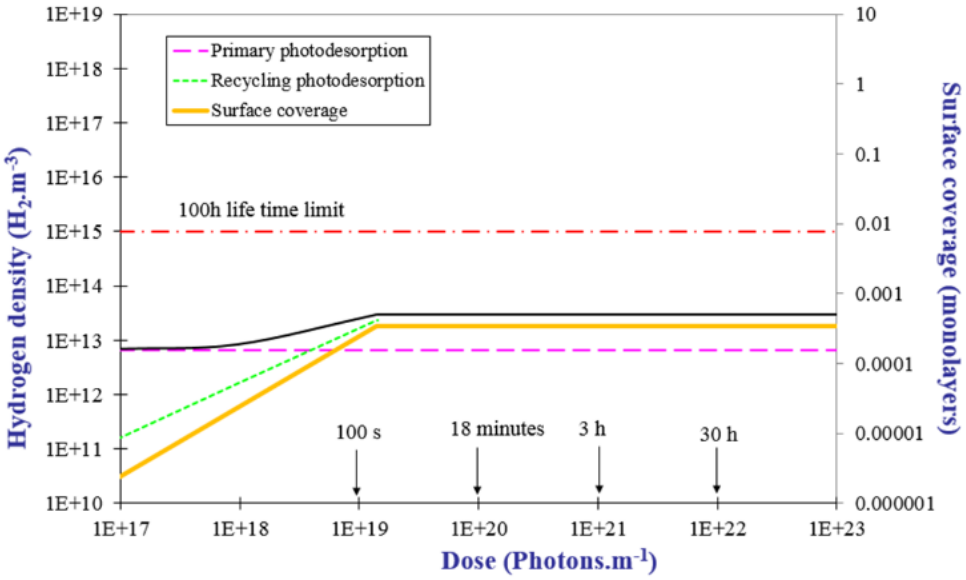

Fig. II.8.25: Gas density and surface coverage evolution in a long perforated cryosorbing tube as a function of the photon irradiation dose.

The LHC cryogenic beam vacuum is made of 8 arcs of 2.8 km each. The proton beams circulate in two independent beam pipes housed in a 1.9 K magnet cold mass inserted in a cryostat. The perforated beam screen is inserted into the 50 mm ID magnet cold bore. The beam screen is cooled between 5 to 20 K by supercritical gaseous helium. The cooling loop intercepts the beam-induced heat load along two half-cells of 53.5 m each, hence, the beam screen temperature profile along an LHC arc is a repetition of the 5-20-5 K pattern every 107 m.

During the LHC beam operation, synchrotron radiation is produced in the bends by the 2808 bunches at a flux of 10^{17} ph/m/s. The light impinges the sawtooth structure at quasi-perpendicular incidence, stimulating the desorption of neutrals and the emission of photoelectrons. The 25 ns spaced bunches with 1.1 10^{11} protons each, provoke an electron cloud build up. In turn, the electrons bombarding the beam screen surface stimulate the desorption of neutrals, emit secondary electrons and deposit part of their energy to the cryogenic system. As shown in Fig. II.8.26, some of the desorbed molecules are physisorbed on the side of the beam screen but a majority is pumped via the beam screen holes and condense on the cold bore tube.

The first observation of synchrotron radiation in the LHC was in August 2010 while the LHC was operating at 3.5 TeV. At that time, a dynamic pressure increase of 2 10^{-10} mbar was noticed when the beam energy was larger than 2 TeV, that corresponds to a critical energy of $\sim$ 1 eV, the energy of chemically bounded molecules. With the years, the dynamic pressure in the LHC arc decreased below the vacuum lifetime limit due to beam conditioning, see Fig. II.8.27.

The LHC room temperature vacuum system is bake-able with most of the machine components

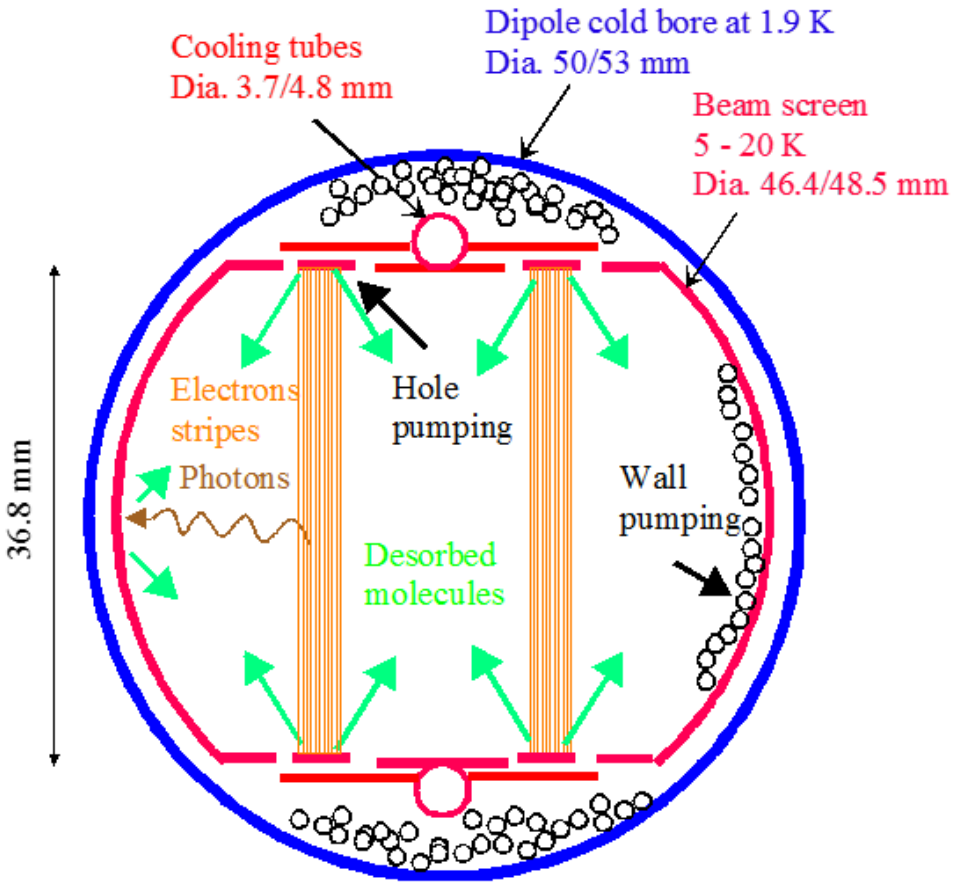

Fig. II.8.26: Schematic cross section of the LHC beam screen and cold bore.

coated with a 1 µm thick TiZrV film. Only a few devices such as collimators, movable masks and injection/extraction kickers are not NEG coated but bake-able. The entire LHC experimental beam pipe is NEG coated. After NEG activation, the static pressure along the 6 km of room temperature beam pipes is $< 10^{-11}$ mbar [42]. The machine is divided in 185 vacuum sectors of lengths ranging from 1 to 150 m.

During the commissioning of a vacuum sector, the uncoated metallic parts are baked to 300°C during 24 h while the NEG coated chambers remain at 100°C to minimise water adsorption. In a second phase, the temperature of the uncoated metallic parts is ramped down to 120°C and the vacuum gauges instruments degassed. Then, the temperature of the NEG is increased to start its vacuum activation.

During the NEG activation the temperature is increased to 200°C and maintained for 24 h; a period during which the native oxide layer is dissolved in the bulk while the TiZrV surface becomes clean. During the temperature ramp, the pressure rises to 10^{-6} mbar, then the activation starts at 180°C and the pressure decrease to 10^{-9} mbar during the plateau. Back at room temperature, very large pumping speeds of $\sim$ 750 l/s/m for H_2 and $\sim$ 12 500 l/s/m for CO are achieved per metre of ID80 mm vacuum chamber [41]. The acceptance criteria of a vacuum sector rely on the temperature monitoring during the NEG activation and diagnostics at the end: gas analysis to demonstrate the cleanliness, pumping speed measurement and leak detection (result shall be below 10^{-9} mbar.l/s).

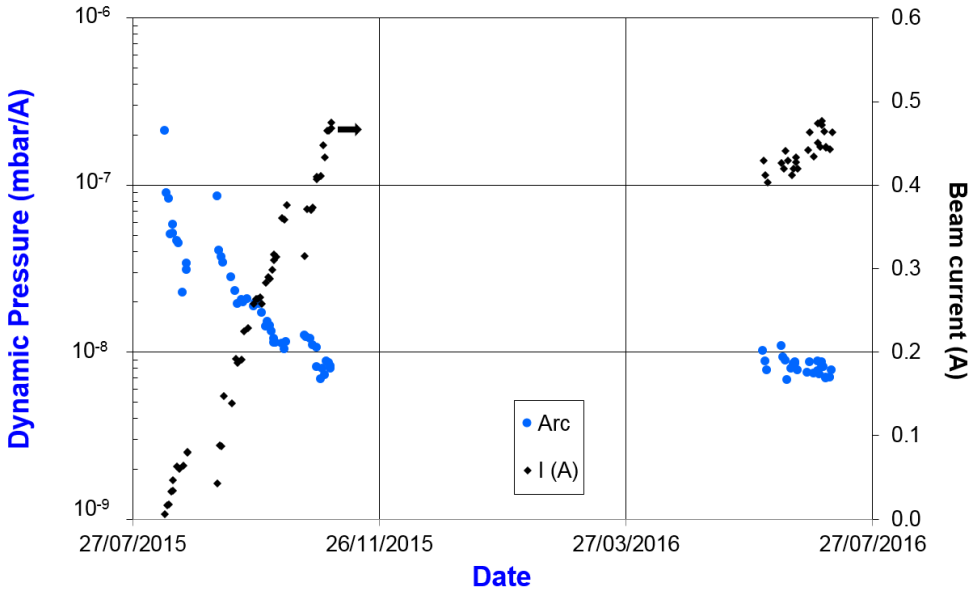

Fig. II.8.27: Dynamic pressure in the LHC arcs [67].

The first observation of the electron cloud in LHC was in the long straight sections by the end of September 2010 [98]. Pressure rises to 10^{-8} mbar were noticed in an unbaked part located at the extremity of the final focusing magnet, a position at 45 m from the interaction point. Although the bunch spacing was 50 ns during that period, in this region, the two beams are counter circulating in the same beam pipe with bunches encounters at multiple of 7.5 m (25 ns), i.e. the position at 45 m away is at the distance of the 6^{th} bunch encounters. The electron cloud phenomenon was demonstrated by powering a 20-Gauss solenoid wrapped around the vacuum chamber, see Fig. II.8.28. While powering the solenoid, the pressure decreased to 5×10^{-10} mbar, demonstrating a strong reduction of the electron stimulated molecular desorption due to the cancellation of the electron multipacting.

Once these very short and specific areas were conditioned under electron bombardment, the average pressure in the long straight sections was in the 10^{-10} mbar range while the beams were circulating. Thanks to the TiZrV NEG coating assisted by an appropriated lumped pumping system, the pressure in the LHC experiments remained also low (5 10^{-10} mbar) despite the two-beam collisions at nominal luminosity (10^{34} Hz/cm^2) and 13 TeV in the centre of mass [67].

II.8.8 Solutions to the exercises

Answer 1: the molar mass of He, air and Ar are 4, 29 and 40 g/mol respectively (air is a mixture of mostly nitrogen with heavier elements such as oxygen with traces of argon and other molecules hence a molar mass of 29 g/mol). For simplicity, room temperature in vacuum technology is usually set to 300 K (i.e. 26.9°C) instead of 293.2 K (20.1°C). Using Eq. II.8.2, the average velocity at room temperature equals 1 300 m/s for He, 470 m/s for air and 400 m/s for Ar. Light molecules travel faster than heavier molecules. Used as a tracer gas for leak detection, helium can be immediately detected in laboratory vacuum systems, however, there might be a time delay even when using helium for leak detection in long

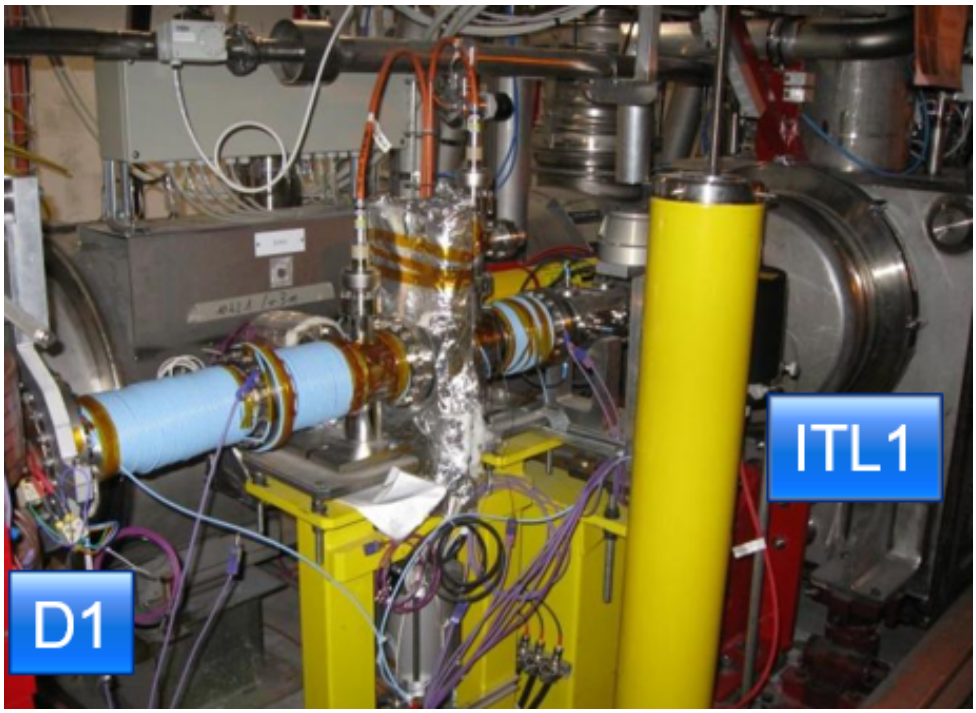

Fig. II.8.28: The 20-Gauss solenoid wrapped around the vacuum chamber upstream to the final focussing magnet ITL1.

pipes such as accelerators beam pipes or cryostats.

Answer 2: the corresponding gas densities to the pressures are 2.5×10^{25}, 2.5×10^{16} and 2.5×10^{11} molecules/m^3 (see Eq. II.8.6). The average molecular speed, derived from Eq. II.8.2, equals 1 776 m/s for H_2 at room temperature. Hence the impingement rate, computed using Eq. II.8.3, equals 1×10^{28}, 1×10^{19} and 1×10^{14} molecules/s/m^2. Since a monolayer equals $\sim 10^{19}$ molecules/m^2, the monolayer formation time are 1 ns, 1 s and 1 day at 1 atm, 10^{-6} mbar and 10^{-11} mbar respectively. The lower the pressure, the larger the monolayer formation time hence the more a vacuum surface can remain free of contamination. Very low pressure is essential to minimise surface contamination.

Answer 3:

$$\begin{aligned} \text{orifice}: \quad & C_{\mathrm{H_2}} = C_{\mathrm{hole,air,RT}}\sqrt{\tfrac{29}{2}} = 3,427[\mathrm{l/s}] \quad \text{and} \quad C_{\mathrm{CO_2}} = C_{\mathrm{hole,air,RT}}\sqrt{\tfrac{29}{44}} = 731[\mathrm{l/s}] \quad , \\ \text{tube}: \quad & C_{\mathrm{H_2}} = C_{\mathrm{tube,air,RT}}\sqrt{\tfrac{29}{2}} = 46[\mathrm{l/s}] \quad \text{and} \quad C_{\mathrm{CO_2}} = C_{\mathrm{tube,air,RT}}\sqrt{\tfrac{29}{44}}, = 10[\mathrm{l/s}] \quad . \end{aligned}$$

Answer 4: the conductance of the vacuum pipe for air is $C = 12$ l/s (see Eq. II.8.15). By applying Eq. II.8.20, the effective pumping speed equals, $S_{\mathrm{eff}} = (12 \times 60)/(12 + 60) = 10$ l/s. Since the effective pumping speed is very close to the tube conductance, the system is conductance limited hence the pressure at the upstream part of the tube is determined by the conductance of the pipe.

Answer 5: hydrogen is the most dominant gas in a baked vacuum system. So, the true pressure is $P = S_{\mathrm{rel,H_2}} \times P_{\mathrm{read}} = 4.4\,10^{-10}$ mbar.

Answer 6: both molecules, nitrogen, N_2, and carbon monoxide, CO have the same principal mass at

28 amu. But a closer look at Table II.8.5 shows that a sub species of N_2 is N (14 amu) with I_{14} = 0.14 I_{28}. Since there are no current at mass 14, the peak at mass 28 represents the ionisation current of CO^+, i.e. carbon monoxide.

Answer 7: masses 2, 28, 40 and 44 correspond to the main peaks of H_2, CO, Ar and CO_2 (see Table II.8.5). Peak 15 is used to trace CH_3^+ originating from CH_4 ionisation in the QMS grid. N_2 and C_2H_6 gas species are ruled out by the absence of signal at mass 14 and 27.

Answer 8: the beam pipe volume equals 78 l. When 1 mbar·l is desorbed from the surface the pressure equals $1/78 \simeq 10^{-2}$ mbar.

Answer 9: the specific outgassing rate after one day is $3 \times 10^{-9}/24 = 1.3 \times 10^{-10}$ mbar.l/s/cm^2. After one week it drops to $3 \times 10^{-9}/(24 \times 7) = 1.8 \times 10^{-11}$ mbar.l/s/cm^2 and to $3 \times 10^{-9}/(24 \times 30) = 4.2 \times 10^{-12}$ mbar.l/s/cm^2 after one month. The beam tube surface, A, equals 31 573 cm^2. Hence the total outgassing rate $Q = qA$ equals $3.9 \times 10^{-6}, 5.6 \times 10^{-7}$ and 1.3×10^{-7} mbar.l/s after one day, one week and one month respectively. And using Eq. II.8.18, one concludes that the pressure equals $1.3 \times 10^{-7}, 1.9 \times 10^{-8}$ and 4.4×10^{-9} mbar after one day, one week and one month respectively.

Answer 10: the specific outgassing rate after bakeout at 300°C is 5×10^{-13} mbar·l /s/cm^2. The beam tube surface, A, equals 31 573 cm^2. Hence the total outgassing rate $Q = qA$, equals 1.6×10^{-8} mbar·l/s after bakeout. So, using Eq. II.8.18 and Table II.8.1, one concludes that the pressure equals 5×10^{-10} Torr (or 7×10^{-10} mbar). A bakeout is mandatory to reach UHV. A bakeout cycle allows to reach the UHV regime in less than a week.

Answer 11: the total outgassing rate of the unbaked vacuum chamber after 1 h of pumping, $Q = qA$ with q given by Eq. II.8.29 and A the surface area, equals 10^{-4} mbar.l/s. The total outgassing after 1 h of pumping for the Viton® seals equals 12.5 x 10^{-5} = 1.3 10^{-5} mbar·l/s. After1 week of pumping (168 h), for a metallic surface with $a = 1$, the total outgassing rate of the metallic part of the unbaked chamber is given by Q_{metal} = 10^{-4} / 168 = 6 10^{-7} mbar·l/s. Whereas for Viton® a = ½, so the total outgassing of the two seals is given by $Q_{\text{Viton}} = 1.310^{-5}/\sqrt{168} = 110^{-6}$ mbar.l/s. The pressure in the unbaked vacuum system is dominated by the Viton® seals. This type of material is obviously forbidden in the UHV-XHV range where ONLY metallic gaskets are used.

Answer 12: using Eq. II.8.1, Eq. II.8.39 can be modified to Eq. II.8.12 as demonstrated below:

$$S = \frac{1}{4} A v = \frac{1}{4} A \sqrt{\frac{8kT}{\pi m}} = A \sqrt{\frac{kT}{2\pi m}} = C_{\text{hole}} \quad .$$

Answer 13: the ideal pumping speed is defined by the maximum pumping speed, i.e. $\sigma = 1$. The gas enters the cryopump at 300 K since the pump is connected to a vacuum system operating at room temperature. The ideal pumping speed is then $3.63 \times 10 \times \sqrt{300/2} = 445$ l/s for H_2 and $3.63 \times 10 \times \sqrt{300/28} = 119$ l/s for CO.

Following multiple collisions with the 10 K chamber, the gas is accommodated with the wall temperature. The chamber surface, A, equals $5 \times \pi \times 100 = 1\,570$ cm^2. Hence the ideal pumping speed equals 4 300 l/s/m for H_2 and 1 500 l/s/m for CO. Each metre of the LHC cold bore (of 5 cm diameter) has a pumping speed of several thousands of l/s!

Answer 14:

P_{300} = 10^{15} x 1.38 10^{-23} x $\sqrt{300 \times 15}$ / 100 = 1 10^{-8} mbar.

P_{300} = 2.5 10^{12} x 1.38 10^{-23} x $\sqrt{300 \times 15}$ / 100 = 2 10^{-11} mbar.

Answer 15:

1. The critical energy for electrons is given by Eq. II.8.47 but we don't know the bending radius. Using Eq. II.8.49, one can compute the bending radius, $\rho = 3/10 \times 0.5/3 = 20$ m. So the critical energy equals $2\,218 \times 3^3/20 = 2\,994.3$ eV.
2. The specific photon flux is given by Eq. II.8.55, $\dot{\Gamma} = 1.28810^{17} \times 3/20 \times 400 = 7.710^{18}$ ph/m/s.
3. The specific power is given by Eq. II.8.52, $P_0 = 88.57 \times 3^4/(2\pi 20^2) = 1\,141.8$ W/m.
4. Using the relativistic formula $E = \gamma m_0 c^2$ and remembering that for an electron, $m_0 c^2 = 511$ keV/c^2, one gets for a 3 GeV beam $\gamma = 3/(511 \times 10^{-6}) = 5\,870.8$. Therefore, the opening angle equals $1/\gamma = 0.0001703$ rad or 0.1703 mrad.
5. The specific gas load, Q, due to photon stimulated molecular desorption can be derived by identification of Eq. II.8.58, $Q = \eta\dot{\Gamma} = 2 \times 10^{-5} \times 7.7 \times 10^{18} = 1.546 \times 10^{14}$ molecules/s/m. Since 2.4×10^{19} molecules correspond to 1 mbar.l according to Eq. II.8.25, then $Q = 1.546 \times 10^{14}/2.4 \times 10^{19} = 6.4 \times 10^{-6}$ mbar.l/s/m.
6. From Eq. II.8.16, one gets $S_{\text{spec}} = Q/P = 6.4 \times 10^{-6}/2 \times 10^{-9} = 3\,201.7$ l/s/m. This is a huge specific pumping speed comparable to the pumping speed of NEG coatings (see Section II.8.4.4.)
7. The conductance scales like $\sqrt{T/M}$. The specific conductance, c, for air is given by Eq. II.8.15 for a length of 100 cm. $c = 12.1 \times 3^3/100 \times 3.3 \times \sqrt{29/2} = 12.4$ l m/s For a lumped pumping system, with infinite pumping speed at the pump, the lowest achievable pressure is given by Eq. II.8.95. Hence, the distance, L, between the pumps shall be, $L = \sqrt{2 \times 10^{-9}/(6.4 \times 10^{-6} \times 12 \times 12.4)} = 0.21$ m. Each pump of infinite pumping speed shall be placed every 21 cm along the accelerator. This is obviously not realistic. One must use a distributed pumping system based on NEG technology
8. The ideal specific pumping speed is given by Eq. II.8.39 for a tube of 1 m long. The specific surface of tube equals $3\pi \times 100 = 942$ cm^2/m. So, the ideal specific pumping speed for hydrogen equals $3.63 \times 942 \times \sqrt{300/2} = 41\,879.7$ l/s/m.
9. The required hydrogen sticking probability to fulfil the specification is given by the ratio of the specific pumping speed to the ideal specific pumping speed, so $\sigma_{H_2} = 32\,01.7/41\,879.7 = 0.08$. This represents a large sticking probability for hydrogen with TiZrV. Even in this case, the specifications are very challenging but reachable [128], and specially developed (rough) coatings are required [41, 129, 130]!

Answer 16: recalling that the elementary charge of the electron equals 1.602×10^{-19} C, the dose of 16 mC/mm^2 corresponds to 10^{19} e/cm^2. Using Table II.8.27 and Eq. II.8.73, one can compute the desorbed quantity for each gas species as given in Table II.8.29. A total of about 40 monolayers of gas has been desorbed during the process.

Answer 17: Equation II.8.77 and Table II.8.29 allow to compute the gas density. The corresponding H_2 gas density is

$$n_{\mathrm{H_2}} = \frac{1}{\tau\,\sigma_{\mathrm{H_2}}\,c} = \frac{1}{3.6\times10^{5}\times95\times10^{-31}\times3\times10^{8}} = 10^{15}\,\mathrm{H_2\cdot m^{-3}} \quad .$$

Using Eq. II.8.6 and Table II.8.1, this gives a pressure equal to 4×10^{-8} mbar at room temperature. Assuming CO as a single species, using Table II.8.29, this gives the following gas density

$$n_{\mathrm{CO}} = \frac{n_{\mathrm{H_2}}}{\sigma_{\mathrm{rel},i}} = \frac{10^{15}}{8.99} \cong 10^{14}\,\mathrm{CO\cdot m^{-3}} \quad .$$

Using Eq. II.8.6 and Table II.8.1, this gives a pressure equal to 4 10^{-9} mbar.

Answer 18: using Table II.8.31 and Eq. II.8.82, one can compute the equivalent H_2 density

$$n_{\mathrm{H_{2\,eq}}} = n_{\mathrm{H_2}} + n_{\mathrm{CO}}\,\sigma_{\mathrm{rel,CO}} = 2\times10^{14} + 8.99\times5\times10^{13} = 6.4\times10^{14} \quad ,$$

from which the vacuum lifetime in hours can be computed using Eq. II.8.77 and Table II.8.29,

$$\tau = \frac{1}{3\,600}\quad\frac{1}{(n_{\mathrm{H_{2\,eq}}}\sigma_{\mathrm{H_2}}\,c)} = \frac{1}{3\,600}\quad\frac{1}{6.4\times10^{14}\times95\times10^{-31}\times3\times10^{8}} = 150\ \mathrm{h} \quad .$$

Answer 19: the cold bore specific surface equals A = 1 570 cm^2/m, the linear outgassing rate per metre of beam pipe is then $Aq = 1\times10^{-9}$ mbar.l/s/m. To maintain an average pressure below $P_{\mathrm{max}} = 10^{-8}$ mbar around the ring, one must have $L/S_{\mathrm{eff}} < P_{\mathrm{max}}/Aq = 10$ (or $S_{\mathrm{eff}}/L > 0.1$).

References

[1] P.A. Redhead, The ultimate vacuum, *Vacuum* **53** (1999) 137–149, doi:10.1016/S0042-207X(98)00349-2.

[2] C. Smorra *et al.* BASE—The Baryon Antibaryon Symmetry Experiment, *Eur. Phys. J. ST* **224** (2015) 3055–3108, doi:10.1140/epjst/e2015-02607-4.

[3] P.A. Redhead, J.P. Hobson and E.V. Kornelsen, *The physical basis of ultra-high vacuum* (Chapman and Hall, London, 1968).

[4] S. Dushman and J.M Lafferty (editor), *Scientific foundations of vacuum technique*, 2nd ed. (J. Wiley & sons, New York, 1962).

[5] J.M. Lafferty (editor), *Foundations of vacuum science and technology*, (J. Wiley & sons, New York, 1998).

[6] K. Jousten (editor), *Handbook of vacuum technology* (Wiley-VCH, Weinheim, 2016), doi:10.1002/9783527688265.

[7] J. Delafosse and G. Mongodin, Les calculs de la technique du vide, *Vide* **16** (1961) pp. 92.

[8] N. Rouvière and G. Rommel, *Bases en technique du vide* (Société française du vide, Paris, 2017).

[9] K .Welch, *Capture pumping technology* 2nd ed. (Elsevier, Amsterdam, 2001), doi:10.1016/B978-0-444-50882-9.X5020-8.

[10] CERN Accelerator School, Vacuum technology, Snekersten, Denmark, 28 May–3 Jun. 1999, edited by S. Turner, CERN 99-05 (CERN, Geneva, 1999), doi:10.5170/CERN-1999-005.

[11] CERN Accelerator School, Vacuum in accelerators, Platja d'Aro, Spain 16–24 May 2006, edited by D. Brandt, CERN 2007-03 (CERN, Geneva, 2007), doi:10.5170/CERN-2007-003.

[12] CERN Accelerator School, Vacuum for particle accelerators, Glumslöv, Sweden, 6–16 Jun. 2017, edited by H. Schmickler *et al.* CERN-ACC-2020-0009 (CERN, Geneva, 2020), doi:10.17181/CAS2017Glumslov.

[13] K. Jousten. *J. Vac. Sci. Technol. A* **26** (2008) 352–359, doi:10.1116/1.2897314.

[14] P.A. Redhead, *Can. J. Phys.* **37** (1959) 1260–1271, doi:10.1139/p59-144.

[15] J.P. Hobson and P.A. Redhead, *Can. J. Phys.* **36** (1958) 271–288, doi:10.1139/p58-031.

[16] D. Alpert, *Le Vide* **17** (1962) pp. 19.

[17] C. Benvenuti, M. Hauer. Improved Helmer gauge for measuring pressures down to 10^{-12} Pascal, Proceedings of 8th Int. Vac. Congress, Cannes, France, 1980. CERN-ISR-VA/80-16.

[18] S. Watanabe, M. Aono, S. Kato, Reduction of outgassing rate from residual gas analyzers for extreme high vacuum measurements, *J. Vac. Sci. Technol. A* **14** (1996) 3261–3266, doi:10.1116/1.580223.

[19] A. Stoeltzel and B. Jenninger, Comparison of ionisation vacuum gauges close to their low pressure limit, *Vacuum* **207** (2023) 111573, doi:10.1016/j.vacuum.2022.111573.

[20] J.A. Basford *et al.*, Recommended practice for the calibration of mass spectrometers for partial pressure analysis, *J. Vac. Sci. Technol. A* **11** (1993) A22-A40, doi:10.1116/1.4755937.

[21] P.A. Redhead, Thermal desorption of gases, *Vacuum* **12** (1962) 203–211, doi:10.1016/0042-207X(62)90978-8.

[22] A.G. Mathewson *et al.*, Thermal desorption of CO from stainless steel, Proc. 7th Int. Vacuum Congress and 3rd Int. Conference on Solid Surfaces of the Int. Union for Vacuum Science, Technique and Applications, Vienna, Austria, 12–16 Sep. 1977, edited by R. Dobrozemsky *et al.* (Wien TU, Vienna, 1977) pp. 1027, preprint CERN-ISR-VA/76-27, doi:10.17181/CERN-ISR-VA-76-27.

[23] J-P. Bacher, C. Benvenuti, P. Chiggiato, M-P. Reinert, S. Sgobba, A-M. Brass. Thermal desorption studies of selected austenitic stainless steels. *J. Vac. Sci. Technol. A* **21** (2003) 167–174, doi:10.1116/1.1527953.

[24] P. Redhead. Recommended practices for measuring and reporting outgassing data, *J. Vac. Sci. Technol. A* **20** 2002 1667–1675, doi:10.1116/1.1496783.

[25] P.A. Redhead, Modeling the pump-down of a reversibly adsorbed phase. I. Monolayer and submonolayer initial coverage, *J. Vac. Sci. Technol. A* **13** (1995) 467–475, doi:10.1116/1.579381.

[26] M. Li and H.F. Dylla. Model for outgassing of water from metal surfaces, *J. Vac. Sci. Technol. A* **11** (1993) 1702–1707, doi:10.1116/1.578482.

[27] A.G. Mathewson and O. Gröbner, Thermal outgassing and beam induced desorption, in *Handbook of accelerator physics and engineering*, Eds. A.W. Chao and M. Tigner, (World Scientific, Singapore, 1999), pp. 253–257, doi:10.1142/9789810248147_0003.

[28] A.G. Mathewson *et al.*, Comparison of chemical cleaning methods of aluminium alloy vacuum chambers for electron storage rings, *J. Vac. Sci. Technol. A* **7** (1989) 77–82, doi:10.1116/1.575736.

[29] C. Herbeaux, P. Marin, V. Baglin, O. Gröbner. Photon stimulated desorption of an unbaked stainless steel chamber by 3.75 keV critical energy photons *J. Vac. Sci. Technol. A* **17** 635–643 (1999), doi:10.1116/1.581630.

[30] P. Tison, Dégazage des aciers inoxydables austénitiques sous ultravide. Rôle de l'hydrogène, *Vide* **48** no. 264 (1992) pp. 377–410.

[31] R.J. Elsey, Outgassing of vacuum materials – I, *Vacuum* **25** (1975) 299–306, doi:10.1016/0042-207X(75)90730-7.

[32] R. Calder and G. Lewin, Reduction of stainless-steel outgassing in ultra-high vacuum, *Br. J. Appl. Phys.* **18** (1967) 1459, doi:10.1088/0508-3443/18/10/313.

[33] J. Kamiya *et al.*, Outgassing measurement of an LHC collimator and estimation for the NEG performances, *Vacuum* **85** (2011) 1178–1181, doi:10.1016/j.vacuum.2011.03.004.

[34] L. Westerberg *et al.*, Hydrogen content and outgassing of air-baked and vacuum-fired stainless steel, *Vacuum* **48** (1997) 771–773, doi:10.1016/S0042-207X(97)00042-0.

[35] B.C. Moore, Recombination limited outgassing of stainless steel, *J. Vac. Sci. Technol. A* **13** (1995) 545–548, doi:10.1116/1.579782.

[36] B. Versolatto and N. Hilleret. CERN LHC Vacuum Group, 2002. Unpublished.

[37] P. Marin *et al.*, Outgassing performance of an industrial prototype tube for the Virgo antenna, *Vacuum* **49** (1998) 309–314, doi:10.1016/S0042-207X(98)00001-3.

[38] K. Saito *et al.*, TiN thin film on stainless steel for extremely high vacuum material, *J. Vac. Sci. Technol. A* **13** (1995) 556, doi:10.1116/1.579785.

[39] P. He *et al.*, Outgassing and surface properties of TiN coated SNS ring vacuum chambers, Proc. of Particle Accelerator Conf. 2003, PAC'03, Portland, Oregon, USA, May 2003, pp. 788–790, doi:10.1109/PAC.2003.1289478.

[40] C. Benvenuti *et al.*, Vacuum properties of TiZrV non-evaporable getter films, *Vacuum* **60** (2001) 57–65, doi:10.1016/S0042-207X(00)00246-3.

[41] P. Costa Pinto, P. Chiggiato, Ti–Zr–V non-evaporable getter films: From development to large scale production for the Large Hadron Collider, *Thin Solid Films* **515** (2006) 382–388, doi:10.1016/j.tsf.2005.12.218.

[42] G. Bregliozzi *et al.*, Achievement and evaluation of the beam vacuum performance of the LHC long straight sections, Proc. of Particle European Accelerator Conference 2008, EPAC'08, Genoa, Italy, May 2008, pp. 3685–3687, https://cds.cern.ch/record/1124067/.

[43] Y. Saito *et al.*, Material and surface processing in J-PARC vacuum system, *Vacuum* **86** (2012) 817–821, doi:10.1016/j.vacuum.2011.01.017.

[44] K. Battes, C. Day and V. Hauer, Systematic study of the outgassing behavior of different ceramic materials, *J. Vac. Sci. Technol. B* **39** (2021) 034202, doi:10.1116/6.0000954.

[45] B. Salvant *et al.*, Update on beam induced RF heating in the LHC, Proc. 4th Int. Particle Accelerator Conference, Shanghai, China, 12–17 May 2013, edited by Z. Dai *et al.* (JACoW, Geneva, 2013) pp. 1646–1648, https://accelconf.web.cern.ch/IPAC2013/papers/tupme032.pdf.

[46] S. Jenzer *et al.*, Is it possible to use additive manufacturing for accelerator UHV beam pipes?, Proc. 10th Int. Particle Accelerator Conference, Melbourne, Australia, 19–24 May 2019, edited by M. Boland *et al.* (JACoW, Geneva, 2019), doi:10.18429/JACoW-IPAC2019-WEXXPLS3.

[47] S. Sammartano *et al.*, Outgassing rates of PEEK, Kapton® and Vespel® foils, CERN-ACC-Note-2020-0039 (CERN, Geneva, 2020), doi:10.17181/CERN-ACC-NOTE-2020-0039.

[48] K. Battes, C. Day and V. Hauer, Outgassing behavior of different high-temperature resistant polymers, *J. Vac. Sci. Technol. A* **36** (2018) 021602, doi:10.1116/1.5001243.

[49] A.G. Mathewson. The surface cleanliness of 316 LN stainless steel studied by SIMS and AES, *Vacuum* **24** (1974) 505, doi:10.1016/0042-207X(74)90017-7.

[50] C. Scheuerlein and M. Taborelli, The assessment of metal surface cleanliness by XPS, *Appl. Surf. Sci.* **252** (2006) 4279, doi:10.1016/j.apsusc.2005.07.007.

[51] G. Cattenoz *et al.*, Vacuum acceptance tests for the UHV room temperature vacuum system of the LHC during LS1, Proceeding of IPAC'14, Dresden, Germany.

[52] O.B. Malyshev, Vacuum requirements, in *Vacuum in particle accelerators* (Wiley-VCH, Weinheim, 2020), pp. 1–23, doi:10.1002/9783527809134.ch1.

[53] J.N. Chubb, L. Gowland and I.E. Pollard, Condensation pumping of hydrogen and deuterium on liquid helium cooled surfaces, J. Phys. D **1** (1968) 361–370, doi:10.1088/0022-3727/1/3/313.

[54] J.N. Chubb and I.E. Pollard, Experimental studies of hydrogen condensation on to liquid helium cooled surfaces, *Vacuum* **15** (1965) 491–496, doi:10.1016/0042-207X(65)90344-1.

[55] R. Haefer, Cryogenic vacuum techniques, *J. Phys. E: Sci. Instrum.* **14** (1981) 273–288, doi:10.1088/0022-3735/14/3/002.

[56] A.A. Krasnov, Molecular pumping properties of the LHC arc beam pipe and effective secondary electron emission from Cu surface with artificial roughness, *Vacuum* **73** (2004) 195–199, doi:10.1016/j.vacuum.2003.12.051.

[57] C. Benvenuti, R.S. Calder and G. Passardi, Influence of thermal radiation on the vapour pressure of condensed hydrogen (and isotopes) between 2 and 4.5 K, *J. Vac. Sci. Technol.* **13** (1976) 1172, doi:10.1116/1.569063.

[58] C. Benvenuti, Characteristics, advantages, and possible applications of condensation cryopumping, *J. Vac. Sci. Technol.* **11** (1974) 591, doi:10.1116/1.1318074.

[59] F. Chill, S. Wilfert and L. Bozyk, Cryopumping of hydrogen on stainless steel in the temperature range between 7 and 18 K, *J. Vac. Sci. Technol. A* **37** (2019) 031601, doi:10.1116/1.5086164.

[60] E. Wallén, Adsorption isotherms of H_2 and mixtures of H_2, CH_4, CO, and CO_2 on copper plated stainless steel at 4.2 K, *J. Vac. Sci. Technol. A* **14** (1996) 2916–2929, doi:10.1116/1.580245.

[61] E. Wallén. Adsorption isotherms of He and H_2 at liquid He temperatures, *J. Vac. Sci. Technol. A* **15** (1997) 265–274, doi:10.1116/1.580523.

[62] L. Amiaud *et al.*, Interaction of D_2 with H_2O amorphous ice studied by temperature-programmed desorption experiments, *J. Chem. Phys.* **124** (2006) 094702, doi:10.1063/1.2168446.

[63] A. Hofmann, *The physics of synchrotron radiation* (Cambridge Univ. Press, Cambridge, 2004), doi:10.1017/CBO9780511534973.

[64] CERN Accelerator School, General accelerator physics, Gif-sur-Yvette, France, 3–14 Sep. 1984, edited by P.J. Bryant and S. Turner, CERN 85-19 (CERN, Geneva, 1985), 2 vols., doi:10.5170/CERN-1985-019-V-1, doi:10.5170/CERN-1985-019-V-2.

[65] CERN Accelerator School, Synchrotron radiation and free electron lasers, Grenoble, France, 22–27 Apr. 1996, edited by S. Turner, CERN 98-04 (CERN, Geneva, 1998), doi:10.5170/CERN-1998-004.

[66] O. Gröbner, The design and performance of the LEP vacuum system at CERN, *Vacuum* **43** (1992) 27–30, doi:10.1016/0042-207X(92)90178-Y.

[67] V. Baglin. The LHC vacuum system: Commissioning up to nominal luminosity, *Vacuum* **138** (2017) 112–119, doi:10.1016/j.vacuum.2016.12.046.

[68] Y. Suetsugu *et al.*, SuperKEKB main ring vacuum system status until the end of Phase-2 commissioning, *J. Vac. Sci. Technol. A* **37** (2019) 021602, doi:10.1116/1.5083928.

[69] J. Gómez-Goñi, O. Gröbner and A.G. Mathewson, Comparison of photodesorption yields using synchrotron radiation of low critical energies for stainless steel, copper, and electrodeposited copper surfaces, *J. Vac. Sci. Technol. A* **12** (1994) 1714–1718, doi:10.1116/1.579042.

[70] V. Baglin, I.R. Collins and O. Gröbner, Photon electron yield and photon reflectivity from candidate LHC vacuum chamber materials with implications to the vacuum chamber design, Proc. 6th European Particle Accelerator Conference, Stockholm, Sweden, 22–26 Jun. 1998, edited by S. Myers *et al.* (JACoW, Geneva, 1998), pp. 2169–2171, http://accelconf.web.cern.ch/e98/PAPERS/TUP18H.PDF.

[71] J. Gómez-Goñi, Photon stimulated desorption from copper and aluminum chambers, *J. Vac. Sci. Technol. A* **25** (2007) 1251–1255, doi:10.1116/1.2712187.

[72] A.G. Mathewson *et al.*, Comparison of synchrotron radiation induced gas desorption from Al, stainless steel and Cu chambers, *AIP Conf. Proc.* **236** (1991) 313–324, doi:10.1063/1.41124.

[73] I.R. Collins *et al.*, A photodesorption study of a TiZr coated stainless steel vacuum chamber, Proc. 8th European Particle Accelerator Conference, Paris, France, 3–7 Jun. 2002, edited by T. Garvey *et al.* (JACoW, Geneva, 2002), https://accelconf.web.cern.ch/e02/papers/wepdo013.pdf.

[74] V. Baglin *et al.*, Molecular desorption by synchrotron radiation and sticking coefficient at cryogenic temperatures for H_2, CH_4, CO and CO_2, *Vacuum* **67** (2002) 421–428, doi:10.1016/S0042-207X(02)00226-9.

[75] V.V. Anashin, A study of the photodesorption process for cryosorbed layers of H_2, CH_4, CO or CO_2 at various temperatures between 3 and 68 K, *Vacuum* **53** (1999) 269–272, doi:10.1016/S0042-207X(98)00365-0.

[76] E. Fischer, Two kilometers at 10^{-10} Torr. The CERN Intersecting Storage Rings for protons, *J. Vac. Sci. Technol.* **9** (1972) 1203–1208, doi:10.1116/1.1317013.

[77] R.S. Calder. Ion induced gas desorption problems in the ISR, *Vacuum* **24** (1974) 437–443, doi:10.1016/0042-207X(74)90001-3.

[78] F.F. Rieke and W. Prepejchal, Ionization cross sections of gaseous atoms and molecules for high-energy electrons and positrons, *Phys. Rev. A* **5** (1972) 1507–1519, doi:10.1103/PhysRevA.6.1507.

[79] G. Hulla, Low energy ion induced desorption on technical surfaces at room temperature, PhD Thesis, Vienna University, March 2009, CERN-THESIS-2009-026, http://hdl.handle.net/20.500.12708/13560.

[80] O.B. Malyshev, The energy of ions bombarding the vacuum chamber walls. Round beams, *Nucl. Instrum. Meth. A* **993** (2021) 165068, doi:10.1016/j.nima.2021.165068.

[81] O.B. Malyshev, The energy of ions bombarding the vacuum chamber walls. Elliptic beams, *Nucl. Instrum. Meth. A* **1027** (2022) 166301, doi:10.1016/j.nima.2021.166301.

[82] A.G. Mathewson, Ion induced desorption coefficients for titanium alloy, pure aluminium and stainless steel, CERN-ISR-VA-76-5 (CERN, Geneva, 1976), 10.17181/CERN-ISR-VA-76-5.

[83] M. Jacob and K. Johnsen, A review of the accelerator and particle physics at the CERN Intersecting Storage Rings, CERN-84-13 (CERN, Geneva, 1984), doi:10.5170/CERN-1984-013.

[84] J. Barnard, Y. Bojko and N. Hilleret, Desorption of H_2 and CO_2 from Cu by 5 keV Ar^+ and H_2^+ ion bombardment, *Vacuum* **47** (1996) 347–350, doi:10.1016/0042-207X(95)00249-9.

[85] N. Hilleret and R. Calder. Ion desorption of condensed gases, Proc. 7th Int. Vacuum Congress and 3rd Int. Conference on Solid Surfaces of the Int. Union for Vacuum Science, Technique and Applications, Vienna, Austria, 12–16 Sep. 1977, edited by R. Dobrozemsky *et al.* (Wien TU, Vienna, 1977), pp. 227–230, preprint CERN-ISR-VA-77-33, doi:10.17181/CERN-ISR-VA-77-33.

[86] H. C. Hseuh, C. J. Liaw, M. Mapes. Design of the SNS accumulator vacuum systems, Proceeding of PAC'99, New York, USA, p. 1345.

[87] O. B. Malyshev, A. Rossi. Ion desorption vacuum stability in the LHC – The multigas model. Proceeding of EPAC'00, Vienna, Austria, p. 948.

[88] J. Kamiya *et al.*, Recent status and improvements of the RCS vacuum system, *JPS Conf. Proc.* **33** (2021) 011023, doi:10.7566/JPSCP.33.011023.

[89] W. Fischer, M. Bai, J. M. Brennan et al. Vacuum pressure rises with intense ion beams in RHIC. Proceeding of EPAC'02, Paris, France, p. 1485.

[90] M. Bender *et al.*, An inelastic thermal spike model to calculate ion induced desorption yields, *Nucl. Instrum. Meth. B* **267** (2009) 885–890, doi:10.1016/j.nimb.2009.02.039.

[91] E. Mahner *et al.*, Molecular desorption of stainless steel vacuum chambers irradiated with 4.2 MeV/u lead ions, *Phys. Rev. ST Accel. Beams* **6** (2003) 013201, doi:10.1103/PhysRevSTAB.6.013201.

[92] A.W. Molvik *et al.*, Heavy-ion-induced electronic desorption of gas from metals, *Phys. Rev. Lett.* **98** (2007) 064801, doi:10.1103/PhysRevLett.98.064801.

[93] O. Brüning and L. Rossi (editors), *The High Luminosity Large Hadron Collider: New machine for illuminating the mysteries of the universe*, 2nd ed. (World Scientific, Singapore 2024), doi:10.1142/13487.

[94] O. Gröbner, Bunch induced multipactoring, Proc. Int. Conference on High Energy Accelerators, Protvino, USSR, 11–17 Jul. 1977 (Protvino Inst. High Energy Phys., Serpukhov, 1977), pp. pp. 277–282, preprint CERN-ISR-VA 77-38, doi:10.17181/CERN-ISR-VA-77-38.

[95] J. Seeman et al. Status report of PEP-II performance, Proceedings of EPAC'00, Vienna, Austria, p. 38.

[96] Y. Suetsugu, K. Shibata, T. Ishibashi et al. SuperKEKB main ring vacuum system status until the end of Phase-2 commissioning, J. Vac.Sci.Technol. A37 021602 (2019), doi:10.1116/1.5083928.

[97] G. Iadarola. Overview on heat loads in the LHC, Proceedings of ECLOUD'18, La Biodola, Italy, p.51. CERN 2020-007.

[98] G. Bregliozzi, V. Baglin, P. Chiggiato et al. Observations of electron cloud effects with the LHC vacuum system, Proceedings of IPAC'11, San Sebastian, Spain, p. 1560.

[99] Y. Suetsugu *et al.*, Achievements and problems in the first commissioning of superKEKB vacuum system, *J. Vac. Sci. Technol. A* **35** (2017) 03E103, doi:10.1116/1.4977764.

[100] M.J. Berger *et al.*, XCOM: Photon Cross Section Database (version 1.5). [Online] National Institute of Standards and Technology, Gaithersburg, MD, last visited 27 November 2023, http://physics.nist.gov/xcom.

[101] R. Cimino, I. R. Collins, and V. Baglin, VUV photoemission studies of candidate Large Hadron Collider vacuum chamber materials, Phys. Rev. ST Accel. Beams 2, 063201 (1999). doi:10.1103/PhysRevSTAB.2.063201.

[102] B.L. Henke, E.M. Gullikson, and J.C. Davis. X-ray interactions: photoabsorption, scattering, transmission, and reflection at E=50-30000 eV, Z=1-92, Atomic Data and Nuclear Data Tables Vol. 54 (no.2), 181-342 (July 1993), https://henke.lbl.gov/optical_constants/.

[103] V. Baglin, Handbook of accelerator physics and engineering. (World Scientific, 2023), p. 336. P. 337. doi:10.1142/13229.

[104] E. La Francesca, M. Angelucci, A. Leidl et al. Reflectivity and photoelectron yield from copper in accelerators, Phys. Rev. Accel. Beams 23, 083101 (2020). doi:10.1103/PhysRevAccelBeams.23.083101.

[105] R. Kersevan, M. Ady, Recent developments of Monte-Carlo codes Molflow+ and Synrad+, proceedings of IPAC'19, Melbourne, Australia, https://molflow.web.cern.ch/content/synrad-downloads.

[106] R. Cimino, V. Baglin and F. Schäfers, Potential remedies for the high synchrotron-radiation-induced heat load for future highest-energy-proton circular colliders, *Phys. Rev. Lett.* **115** (2015) 264804, doi:10.1103/PhysRevLett.115.264804.

[107] R. Cimino and I.R. Collins, Vacuum chamber surface electronic properties influencing electron cloud phenomena, *Appl. Surf. Sci.* **235** (2004) 231–235, doi:10.1016/j.apsusc.2004.05.270.

[108] V. Baglin *et al.*, The secondary electron yield of technical materials and its variation with surface treatments, Proc. 7th European Particle Accelerator Conference, Vienna, Austria, 26–30 Jun. 2000, edited by W.A. Mitaroff *et al.* (JACoW, Geneva, 2000), pp. 217–221, https://cds.cern.ch/record/466534.

[109] R.E. Kirby and F.K. King, Secondary electron emission yields from PEP-II accelerator materials, *Nucl. Instrum. Meth. A* **469** (2001) 1–12, doi:10.1016/S0168-9002(01)00704-5.

[110] R. Cimino and T. Demma, Electron cloud in accelerators, *Int. J. Mod. Phys. A* **29** (2014) 1430023, doi:10.1142/S0217751X14300233.

[111] B. Henrist *et al.*, The secondary electron yield of TiZr and TiZrV non-evaporable getter thin film coatings, *Appl. Surf. Sci.* **172** (2001) 95–102, doi:10.1016/S0169-4332(00)00838-2.

[112] R. Cimino *et al.*, Nature of the decrease of the secondary-electron yield by electron bombardment and its energy dependence, *Phys. Rev. Lett.* **109** (2012) 064801, doi:10.1103/PhysRevLett.109.064801.

[113] V. Petit *et al.*, Beam-induced surface modifications as a critical source of heat loads in the Large Hadron Collider, *Commun. Phys.* **4** (2021) 192, doi:10.1038/s42005-021-00698-x.

[114] W. Vollenberg *et al.*, Amorphous carbon coating in SPS, Proc. 12th Int. Particle Accelerator Conference (IPAC 2021), Online, 24–28 May 2021, edited by L. Lin *et al.* (JACoW, Geneva, 2021), pp. 3475–3478, doi:10.18429/JACoW-IPAC2021-WEPAB338.

[115] M. Haubner, V. Baglin and B. Henrist, Electron conditioning of technical surfaces at cryogenic and room temperature in the 0–1 keV energy range, *Vacuum* **207** (2023) 111656, doi:10.1016/j.vacuum.2022.111656.

[116] H. Tratnik, N. Hilleret and H. Störi, The desorption of condensed noble gases and gas mixtures from cryogenic surfaces, *Vacuum* **81** (2007) 731, doi:10.1016/j.vacuum.2005.11.064.

[117] R. Dupuy *et al.*, Electron-stimulated desorption from molecular ices in the 0.15–2 keV regime, *J. Appl. Phys.* **128** (2020) 175304, doi:10.1063/5.0021832.

[118] A. G. Mathewson. Calculation of characteristic beam decay times in LHC, CERN-LHC-VAC/AGM, Vacuum Technical Note 96-02, February 1996.

[119] A.G. Mathewson. Vacuum system design, CAS - CERN Accelerator School : 5th General Accelerator Physics Course, Jyväskylä, Finland, September 1992. CERN-94-01-V2.

[120] A. Rossi. VASCO (VAcuum Stability COde): multi-gas code to calculate gas density profile in a UHV system, CERN LHC Project Note 341, 2004.

[121] A. Rossi. Residual Gas Density Estimations in the LHC Insertion Regions IR1 and IR5 and the Experimental Regions of ATLAS and CMS for Different Beam Operations, CERN LHC Project Report 783, 2004.

[122] O. Gröbner, Overview of the LHC vacuum system, *Vacuum* **60** (2001) 25, doi:10.1016/S0042-207X(00)00240-2.

[123] The Large Hadron Collider in the LEP Tunnel, Ed. by G. Brianti and K. Hübner, CERN 87-05, May 1987.

[124] Design study of the Large Hadron Collider, The LHC Study Group, CERN 91-03, May 1991.

[125] V.V. Anashin, O. B. Malyshev, V. N. Osipov et al. Investigation of synchrotron radiation-induced photodesorption in cryosorbing quasiclosed geometry, J. Vac. Sci. Technol. A 12, 2917–2921 (1994), doi.org/10.1116/1.578965.

[126] R. Calder *et al.*, Synchrotron radiation induced gas desorption from a prototype Large Hadron Collider beam screen at cryogenic temperatures, *J. Vac. Sci. Technol. A* **14** (1996) 2618–2623, doi:10.1116/1.579989.

[127] V. Baglin *et al.*, First results from COLDEX applicable to the LHC cryogenic vacuum system, Proceeding of EPAC'00, Vienna, Austria, p.2283.

[128] M. Grabski, E. Al-Dmour and S.M. Scolari, Vacuum system performance of the 3 GeV electron storage ring at MAX IV Laboratory, Proc. 13th Int. Particle Accelerator Conference, Bangkok, Thailand, 12–17 Jun. 2022, edited by F. Zimmermann *et al.* (JACoW, Geneva, 2022), pp. 2836–2838, doi:10.18429/JACoW-IPAC2022-THPOTK034.

[129] S. Calatroni *et al.*, NEG thin film coating development for the MAX IV vacuum system, Proc. 4th Int. Particle Accelerator Conference, Shanghai, China, 12–17 May 2013, edited by Z. Dai *et al.* (JACoW, Geneva, 2013) pp. 3385–3387, https://accelconf.web.cern.ch/IPAC2013/papers/thpfi044.pdf.

[130] P. Costa Pinto *et al.*, Development and production of non-evaporable getter coatings for the vacuum chambers of the 3 GeV storage ring of MAX IV, Proc. 6th Int. Particle Accelerator Conference, Richmond, VA, USA, 3–8 May 2015, edited by S. Henderson *et al.* (JACoW, Geneva, 2015), pp. 3145–3147, doi:10.18429/JACoW-IPAC2015-WEPHA019.